Novel Deflection Sensing and Actuation Methods for Needle Steering in Soft Tissue

by

Thomas D. Lehmann

A thesis submitted in partial fulfillment of the requirements for the degree of

Doctor of Philosophy

in

Biomedical Engineering

Department of Electrical and Computer Engineering

University of Alberta

Abstract

Needle insertion is a minimally invasive intervention for procedures involving drug delivery, biopsy, and radiation therapy. In the prominent radiation therapy procedure prostate brachytherapy, rice grain sized radioactive seeds are introduced into soft tissue via needles in and around the prostate to treat cancerous cells. To ensure an effective distribution of radiation, the seeds need to be distributed according to a pre-calculated plan, which is difficult to achieve as needles deflect from the ideal, straight trajectory. The needle deflection can be manually corrected by the surgeon based on training and intuition through intermittent axial rotation or lateral force application. In order to support the surgeon in guiding the needle towards a straight trajectory, robotic assistance can be used. In order to steer a flexible needle towards a defined target, ultrasound-image-based needle localization is commonly used for needle tip position feedback. Acquiring and processing of ultrasound images, however, significantly limits the control sampling rate. As an alternative, this work proposes a real-time estimator for needle deflection during insertion based on shear force and bending moment measured at the needle base by a force/torque sensor that does not require implicit knowledge of tissue properties and could replace image-based deflection measurement. The estimator is based on an adaptive quasi-static mechanics-based model for needle-tissue interactions. The model's estimation performance is evaluated and experimentally compared by carrying out insertion experiments into homogeneous phantom and non-homogeneous biological tissues. The estimator maintains an adequate estimation accuracy up to a high insertion depth, as confirmed by insertion experiments into phantom and biological tissue samples. The proposed deflection estimator is subsequently applied to needle steering. The needle tip trajectory obtained during insertion from the estimator is used to parameterize a kinematic bicycle model. The bicycle model is then used to predict the needle tip trajectory and the ideal depth at which to rotate the needle to reach a desired target. Experimental results show that the method accurately predicts the needle tip trajectory and the ideal rotation depth.

In the second part of this thesis, a novel needle actuation method is proposed based on a technique used manually by surgeons to steer the needle. A point force is applied laterally onto the needle near its entry point into tissue during insertion in order to manipulate the needle deflection. As a first step to examine how lateral needle actuation can enhance and complement steering, an experimental needle insertion study is carried out. The results show that lateral actuation further reduces needle deflection at the final insertion depth in a way that is not possible with only one intermittent axial needle rotation. In order to facilitate model-based automatic control, an energy-based needle deflection model that can account for lateral actuation and intermittent axial needle rotation is subsequently developed. Experimental model validation shows a small error of approximately 0.5-2 mm between measured and estimated needle tip deflection. Moreover, a simulation study using the developed deflection model further highlights the potential for and limitations of needle deflection reduction. Consequently, a model-based steering approach is devised that steers the needle in real-time based on a pre-planned trajectory optimized for needle placement as desired in prostate brachytherapy. It is experimentally shown that the needle deflection can be significantly reduced with only lateral needle actuation as steering input such that the needle tip trajectory during insertion remains close to the pre-planned trajectory.

The above proposed energy-based deflection model requires the tissue Young's modulus as parameter input. Therefore, in the final chapter of this thesis, an intraoperative method for the identification of tissue Youngs modulus using lateral needle actuation is proposed. The needle-tissue system's response to lateral force is observed and the tissue Youngs modulus is then identified based on the energy stored in the needle-tissue system. Experimental studies are presented to confirm the relatively good accuracy of the identified tissue Youngs modulus when compared to an independent measurement.

Preface

In the following, all contents of this thesis published in peer-reviewed conferences and journals are listed. Parts of Chapter 3 were presented at the *2015 IEEE International Conference on Robotics and Automation* [1] (Section 3.2) and published in *IEEE/ASME Transactions on Mechatronics* [2] (Section 3.3). The contents of Chapter 4 were presented at the *2016 IEEE/ASME International Conference on Advanced Intelligent Mechatronics* [3], contents of Chapter 5 are published in *IEEE Robotics and Automation Letters* [4], contents of Chapter 6 are published in *IFAC Mechatronics*[5], and contents of Chapter 8 are published in *IEEE Transactions on Instrumentation and Measurement* [6]. In all of the above listed publications, Thomas Lehmann is the first author. The literature review provided in Section 1.2 is the author's own work.

The experimental needle insertion setups introduced in Chapter 2 are the author's own work except for the Hand-held Needle Steering Assistant, which was developed by Carlos Rossa. All described devices and algorithms that are the work of others are acknowledged where appropriate. Mr. Abdoreza Farhangi contributed to the design of the lateral needle actuation system introduced in Chapter 2.

To my parents Barbara and Hans-Dieter Lehmann.

Acknowledgements

I would like to express my sincerest gratitude to my supervisor Dr. Mahdi Tavakoli for believing in my abilities and giving me the opportunity to conduct this research under his guidance, for the ever-present support, encouragement and advice, and for being an outstanding mentor and role model in many regards. Thank you also to my co-supervisor, Dr. Ron Sloboda for the expert advice, suggestions, and very thorough and thoughtful feedback on my work and writing. I would also like to thank Dr. Carlos Rossa for the great supervision and guidance, for always going above and beyond to provide excellent and thorough feedback on my work and manuscripts, which helped to significantly improve my writing. Thank you to Dr. Nawaid Usmani for always being available when expert opinions on the surgical procedure of prostate brachytherapy were needed, for providing access to the operating room in order to observe a prostate brachytherapy procedure and for providing valuable feedback on my work. Many thanks also to my peers Jay Carriere, Bita Fallahi, Mohsen Khadem and Michael Waine for the many fruitful discussions, advice and help on countless occasions. I would also like to thank all current and past members of the Telerobotic and Biorobotic Systems Group that I had the pleasure and privilege to work with for the excellent work atmosphere and the many social gatherings on and off campus that helped make my stay absolutely enjoyable and unique. Thank you also to Brayden DeBoon, Abdoreza Farhangi, Shayan Meschian and Qingxin Yuan for their assistance and help with experiments, and experimental setup assembly and development. Furthermore, thank you also to the third member of my supervisory committee, Dr. Qing Zhao, and all professors who served as examiners on my candidacy and final thesis examination. The research presented in this thesis was supported by the Canada Foundation for Innovation (CFI), the Alberta Innovation and Advanced Education Ministry, the Natural Sciences and Engineering Research Council (NSERC) of Canada, the Canadian Institutes of Health Research (CIHR), the Alberta Innovates - Health Solutions (AIHS) and by a University of Alberta startup grant.

Contents

List of Tables

List of Figures

Chapter 1

Introduction

1.1 Needle Insertion

Percutaneous (from Latin ”through the skin”) needle insertion has in the last decades been used increasingly in medical practice with many advantages due to the minimally invasive nature of the thin tubular devices used for the procedures and thus minimum trauma caused to the patient. Needles allow internal organs and regions of the body to be accessed with very minor trauma. In several medical applications such as drug delivery, biopsy and radiation therapy needles are inserted in order to administer drugs or radioactive agents, or to withdraw tissue samples. Needle insertion has also become a subject of study in the field of robotics in the past decade towards increasing the efficiency and accuracy of the surgical procedures. Typically in medical applications of needle insertion, the needle needs to be steered towards a pre-defined target. From this, potential applications for robotic assistant systems in needle insertion arise such as automated or assisted needle steering, pre-planning and simulation of the needle trajectory, and visual and haptic assistance and decision support.

One of the procedures, in which needles are inserted to deliver radioactive agents for cancer irradiation is the treatment procedure prostate brachytherapy. The following section introduces the procedure in more detail as the research conducted in this thesis is aimed towards prostate brachytherapy.

1.1.1 Prostate Brachytherapy

Prostate cancer is the second most frequently diagnosed cancer in men worldwide, with 1.1 million new cases estimated in 2012. Furthermore, prostate cancer is the fifth leading cause for cancer-related deaths worldwide [7]. For Canada it is projected that in 2017, about 21,300 new cases of prostate cancer will be diagnosed, which constitutes 21% of all cancer diagnoses in men and represents the most commonly diagnosed type of cancer. The projected percentage of all estimated cancer deaths is 10%, which ranks third among men [8].

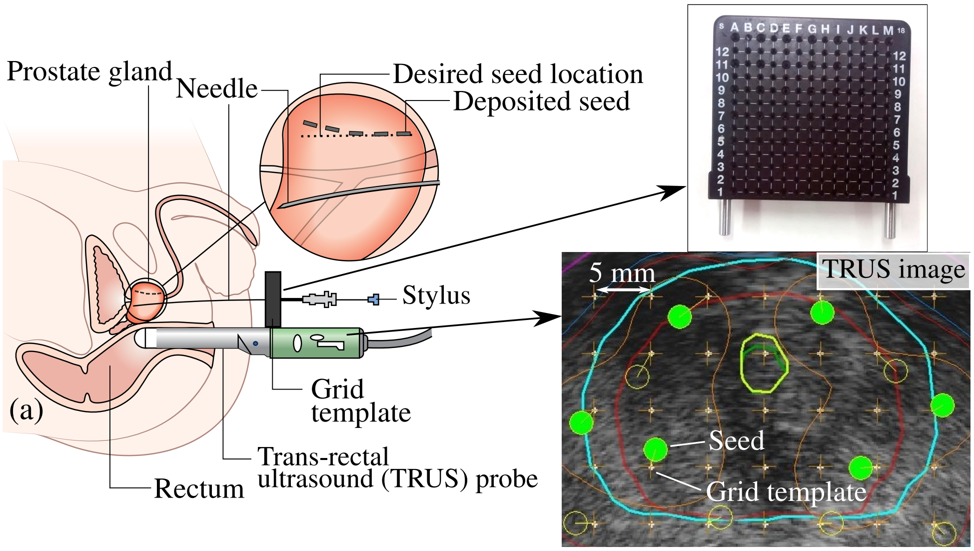

Figure 1.1: A schematic representation of the radiation therapy procedure prostate brachytherapy. Radioactive seeds are implanted within the prostate with a needle guided by a grid template. The location of seed deposition is observed with a trans-rectal ultrasound (TRUS) probe (source: Cancer Research UK / Wikimedia Commons).

A popular treatment option for early-stage prostate cancer is prostate brachytherapy (from Greek “short distance” therapy) where rice-grain sized seeds are implanted into the prostate using needles. A schematic representation of the procedure shown in Figure 1.1 illustrates needle insertion under ultrasound guidance that is commonly referred to as the “Seattle” technique [9]. Multiple low-dose-rate (LDR) seeds typically containing the radioisotope ^{125}I are implanted in and around the prostate gland. To do this, a total of approximately 16-20 hollow needles carrying rows of seeds are inserted successively by hand, guided by a 5 mm grid template (see Figure 1.1). When the final insertion depth is reached, each needle is withdrawn while at the same time the seeds are pushed out using a stylet. This way, ideally multiple rows of seeds are implanted in parallel at distances defined by the grid template. The distribution of the seeds is pre-planned in order to achieve a desired distribution of radiation across the cancer-affected prostate volume. During insertion and seed deposition, the location of needle and deposited seeds is monitored by a trans-rectal ultrasound (TRUS) probe to facilitate accurate seed placement.

For the radiation emitted by the seeds to be distributed efficiently throughout the prostate, it is important for the seeds to be deposited at their pre-planned locations. The target locations are registered with the template holes and, therefore, it is desirable that the needle remain on a straight trajectory during insertion. The seeds then apply a defined dosage of radiation to the cancerous tissue from close proximity, thus directly affecting the cancer while reducing radiation exposure to surrounding healthy tissue and organs. Brachytherapy is an established alternative to other cancer treatment procedures such as external beam radiation therapy as it is more patient friendly, less time consuming (e.g. only 1-2 sessions) and carries high success rates in terms of tumour reduction.

As mentioned, a critical assumption during pre-planning is that the needle remains on a straight trajectory during insertion. In clinical practice, however, this assumption does not hold well as the needle deflects from the desired straight trajectory due to its bevelled tip. Thus, needle deflection can cause the seeds to be misplaced from their desired locations within the prostate, which in turn causes inefficient distribution of radiation and can therefore negatively affect treatment efficacy [10][11].

The tip of brachytherapy needles is bevelled to enable manual steering and to minimize cutting-induced tissue trauma. During insertion, the bevelled tip causes the tissue to be displaced asymmetrically, which forces the needle to deflect in the same direction as the bevel. This feature of the bevelled-tip needle can be used during insertion to steer the needle by simply intermittently rotating the needle axially to adjust the bevel direction and therefore the unadjusted direction of needle deflection as the needle is further inserted. This technique is in fact commonly applied during prostate brachytherapy. During insertion, the surgeon will insert the needle and observe the deflection through TRUS images. If an unacceptable amount of deflection is observed, the surgeon will manually rotate it by 180° about its insertion axis to steer the needle back towards the target. Rotation may be done intermittently throughout insertion rather than continuously to avoid tissue damage and out-of-plane deflection. The needle deflection needs to be controlled by an experienced surgeon such that the needle shape at the final insertion depth reaches the target and is as close to the unbent needle as possible [12]. The absolute seed placement uncertainty is approximately ±5 mm for manual placement by an expert practitioner [11].

A further method for steering the needle is the manual application of lateral force onto the needle shaft between the patient's skin and the grid template. The lateral force causes the shaft to be displaced laterally. When the force is applied at a shallow insertion depth and maintained during further insertion, the needle deflection can be significantly reduced. The lateral force application technique can also be used to enhance needle deflection in order to reach the volume of the prostate behind the pubic arch [12].

These methods of manual needle steering and trajectory control can be automated using robotic assistance in order to aid the surgeon during prostate brachytherapy and more generally during all needle insertion procedures. Extensive research has been conducted in various robotics-related fields towards advancing automated needle steering techniques. The following section introduces basic concepts and components for robotic needle steering and reviews the main body of work that is fundamentally and also tangentially related to this thesis. In each chapter, state of the art research related to the specific chapter contents is introduced in detail.

1.2 Literature Review on Robotics-assisted Needle Insertion

Various aspects of robotic needle steering have been studied by the robotics community for nearly two decades. One major goal of past research concerning robotic needle steering is the improvement and facilitation of the various medical applications associated with needle steering such as biopsy, radiation therapy (e.g., brachytherapy), ablation and drug delivery. The main operational objective of the vast majority of such needle insertion applications is the steering of the needle to a specific location within the body. Robotic needle steering can increase the accuracy of needle placement at various levels of automation and provide additional information or decision support to the medical practitioner. Towards this objective, extensive research has been conducted in modelling needle-tissue interactions, sensing, estimation and prediction of needle deflection, and control algorithms for needle steering using predominantly axial rotation as the control action. In this section, the current state of the art in robotics-assisted needle steering is introduced with primary focus on literature that is directly relevant to this thesis, such as needle-tissue interaction modelling, needle deflection estimation and control, and robotic systems for needle insertion. Figure 1.2 depicts major mutually related concepts and components that are required for robotics-assisted needle insertion and steering, and their interactions as a block diagram. The components of the physical system comprised of the needle and tissue (Figure 1.2, block 3) interact during needle insertion. As the needle is inserted, various coupled interaction forces act between the needle

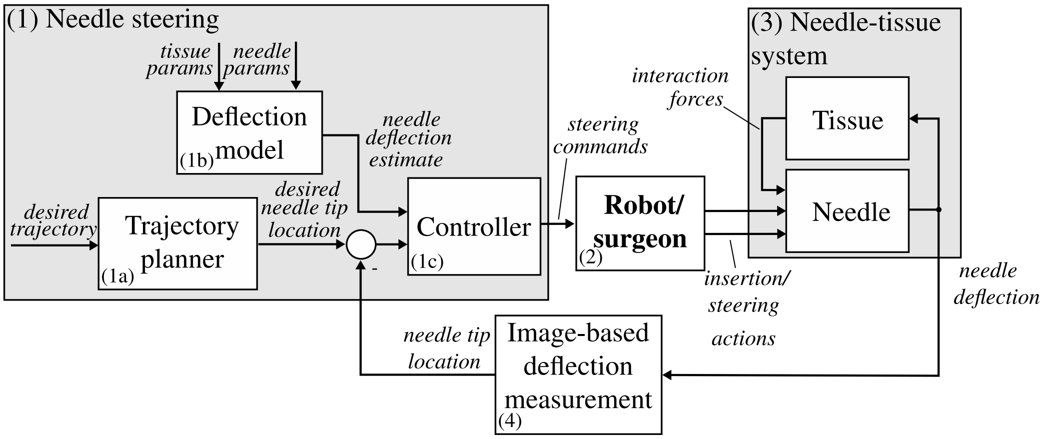

Figure 1.2: General conceptual representation of various components of robotics-assisted needle insertion [27].

and tissue and can be compartmentalized into friction, tissue displacement, tissue compression and bevelled-tip induced cutting [13, 14, 15, 16, 17, 18, 19, 20, 21, 22, 23, 24, 25, 26]. The interaction force mainly responsible for needle deflection is a result of the asymmetric displacement of tissue by the bevelled needle tip. This force is commonly referred to as the *cutting force* and often modelled as a point load at the needle tip. As the needle is introduced, the needle tip cuts and displaces the tissue, which in turn causes a reaction load enacted by the tissue onto the needle's bevel surface [14]. The reduced point load acts normal to the needle axis in the same direction as the bevel. As a result of its deflection, the needle applies lateral pressure onto the tissue along its inserted portion. The elastic properties of the tissue then cause it to enact a reaction load onto the needle. In order to either complement, avoid the need for needle deflection measurement, or estimate/predict deflection, various needle-tissue interaction associated needle deflection models (Figure 1.2, block 1b) based on the mechanics of needle-tissue interactions have been proposed [13, 28, 14, 15, 17, 19, 29, 20, 21, 30, 23, 31, 25, 32, 26, 33, 34, 35].

Fundamental interactions between needle and tissue such as friction and cutting-related tip forces have been investigated [28, 14, 36, 19, 29]. Okamura *et al.* first investigated the types of force interactions occurring between the needle and tissue [14]. The identified physical needle-tissue interactions are separated into stiffness before puncture, and friction and cutting force after puncture. The paper further devises a method to experimentally quantify and distinguish the individual force components.

The first quasi-static mechanics-based needle-tissue interaction model proposed by Kataoka *et al.* considers the tissue deformation caused by tissue displacement as a uniform distribution along the inserted needle portion [13]. A model which establishes a relation between base force and the deflection is then derived. The model, however, significantly underestimates needle deflection. Using force interactions between needle and tissue such as cutting force and tissue support, and force/torque measurements at the needle base, Abolhassani *et al.* establish a relationship with needle deflection [15, 17]. In Lehmann *et al.* [31], assumed needle-tissue interaction loads are parameterized using force and moment measurements at the needle base. Interaction loads along the needle are modelled with multiple distributed loads. Their developed modelling method shows improvements in deflection estimation accuracy compared to the above described quasi-static deflection models.

A detailed study considering macroscopic and microscopic needle-tissue interactions was proposed by Misra *et al.* [20]. They presented an energy-based mechanical model that takes into account needle bending (strain energy), needle-tissue interaction (compression and elasticity) and tip cutting work (tip force and rupture). The model accordingly accounts for the needle tip and shaft interactions as the needle cuts through tissue [29, 20]. Roesthuis *et al.* extended the model proposed by Misra *et al.* by modelling the resistive force due to tissue compression as a distributed load acting along the inserted needle portion and incorporating needle steering through axial rotation into the model [21, 30]. Another model that uses an energy-based approach was proposed by Lee and Kim [34]. Khadem *et al.* developed a comprehensive dynamic model for needle deflection that incorporates insertion velocity to be used as a further control input along with axial needle rotation [32]. Khadem *et al.* also developed a two-body rigid/flexible dynamic model that allows for a wider variety of control commands such as insertion velocity, axial rotation, and needle base force/torque to be used for real-time needle steering control [26]. Rossa *et al.* in their version of an energy-based model consider also a cutting-related tip force and a load along the inserted needle portion modelled by a set of elastic springs [33, 35]. The springs model the tissue's resistance to compression. The spring stiffness is the tissue's Young's modulus. To determine the amount of tissue compression at a given position along the needle, the difference between the needle shaft shape and the needle tip path, also referred to as the tip trajectory, is considered accounting for an arbitrary amount of axial needle rotations. Moreover, the (stationary) grid template commonly used in prostate brachytherapy (see Figure 1.1) is included in the model.

Other proposed deflection models are kinematics-based [37, 38, 29, 23, 39, 40, 26] e.g., based on bicycle kinematics, which are less directly associated with tissue properties but can nevertheless adequately model and predict multi-bend needle tip trajectories. The use of kinematic unicycle and bicycle models was first introduced and adapted for the purpose of modelling multi-bend needle tip trajectories by Park *et al.* and Webster *et al.* [41, 37]. Webster *et al.* devised a method to relate the needle tip trajectory to the unicycle or bicycle model's planar trajectory where the centre of the unicycle wheel or the the centre of the bicycle's rear wheel can be virtually attached to the needle tip. To model a needle rotation about 180°, the sign of the bicycle's front wheel angle is inverted. The bicycle offers more parameters to adjust than the unicycle as the attachment point of the bicycle to the needle tip can be chosen more freely, and the bicycle's wheel distance can be adjusted. The kinematic bicycle model has become the most commonly used method for needle trajectory planning and on-line trajectory adjustment. Other adjustable parameters of a bicycle model are the bicycle's translational velocity and hence the needle insertion velocity, the front wheel's steering angle and the angular velocity of the front wheel's steering angle. Fallahi *et al.* extended the bicycle model by adding virtual rollers to the bicycle wheels that allow the bicycle to slip laterally thus essentially adding the possibility to loosen the non-holonomic constraints as desired [40]. A further application of deflection models and needle-tissue interaction models is the simulation of needle insertion and procedure pre-planning.

Needle deflection can be measured through medical imaging modalities (Figure 1.2, block 4) such as ultrasound (US) [42, 43, 44, 45, 46, 47, 23, 48, 49, 50, 51, 52], magnetic resonance (MR) [53, 54] or computed tomography (CT) [55, 56] imaging. The image modality with the most focus has been US since it is low-cost, does not expose the patient to ionizing radiation and does not impose design and material requirements on mechanical support structures and robotic systems. Commonly, US-image-feedback-based needle steering systems use actuated US probes that track the needle tip during insertion and record axial US image slices of the needle within tissue from which the current needle tip deflection can be obtained and used for feedback control.

To define a trajectory on which the needle or its tip should travel in order to reach a desired target while at the same time avoiding obstacles such as bones or vessels, a trajectory planner (Figure 1.2, block 1a) can be used. To construct the desired trajectory, deflection and needle-tissue interaction models can be utilized. The desired trajectory is then supplied to the control algorithm responsible for needle steering. Various trajectory planning algorithms have been developed. A common approach for needle trajectory planning involves the combination of kinematic models and rapidly exploring random trees (RRT). Such planners are then augmented with on-line re-planning using image feedback in order to correct for inaccuracies in the planned trajectory that are caused by model errors [57, 58, 59, 36, 41, 38, 60, 61, 62, 63, 64, 65, 66, 67, 39].

A controller (Figure 1.2, block 1c) then generates appropriate control actions based on measured and estimated/predicted needle deflection feedback as well as the pre-planned trajectory. The control actions can either be supplied to an automatic robotic system or suggested to the surgeon depending on the desired level of automation. In case of a planar deflection controller, a primary control action is intermittent axial needle rotation. This method of steering reduces tissue trauma by reducing drilling effects [68] but is relatively restrictive in terms of curvature manipulation as the needle tip follows a non-holonomic trajectory similar to that of a unicycle or bicycle with fixed steering radius. A further deflection control method that allows for an arbitrary choice of needle curvature is duty-cycled spinning [69, 70, 48, 66]. The method was first introduced by Engh *et al.* and proposes that the needle be rotated frequently during insertion in a given stop-and-go manner instead of intermittently [69]. By adjusting the duty cycle of spinning, the needle's curvature can be adjusted arbitrarily where shorter stop intervals lead to an increased radius of curvature. A considerable drawback of this method is, however, that constant spinning of the needle during insertion can cause significant tissue trauma due to the aforementioned drilling effect caused by the needle tip [68]. To carry out needle insertion and steering with various levels of automation, a large variety of fully autonomous and assistive robotic systems (Figure 1.2, block 2) have been developed. The implemented needle steering concepts and robotic systems for needle steering can be divided into three automation levels: *Level 3*: fully automated steering [71, 72, 73, 74, 75, 76]. Here, the robot is completely in charge of needle insertion and steering. *Level 2*: semi-automated steering (surgeon-in-the-loop) [77, 78, 35, 79, 80, 81]. Here, tasks are shared among the robotic system and surgeon. For example, the surgeon carries out safety-critical tasks such as insertion and the robot is in charge of steering the needle [35]. *Level 1*: assisted manual steering [82, 56, 53, 83, 84, 85]. In this automation level, while all actions are carried out by the surgeon, his or her awareness can be enhanced through haptic or visual cues, etc. and decision support can be provided.

1.3 Motivation and Objectives

This thesis proposes novel methods for needle deflection sensing, estimation, prediction and actuation in order to enhance the steering and placement of flexible needles during insertion into soft tissue.

1.3.1 Force/torque Based Needle Deflection Estimation

As mentioned, needle deflection inside tissue is predominantly measured using ultrasound (US) imaging. The sampling rate of image-based deflection measurement is, however, limited to approximately 20 Hz due to the limited rate of image generation. Depending on the insertion velocity, this can result in significant disadvantages. Moreover, in order to for instance measure the needle tip deflection during insertion using axial US images, the US probe needs to track the needle tip. This occupation of the US probe can prove disadvantageous during a medical procedure such as prostate brachytherapy where the surgeon would lose the ability to observe other regions of interest. Furthermore, the various needle deflection models reviewed in Section 1.2 require tissue parameters such as the Young's modulus, which is difficult to obtain and in many cases requires additional expensive equipment in a clinical scenario. To solve these issues, in Chapter 3, the first developed sensing method for needle deflection uses the measured shear force and bending moment that result from the deflecting needle. A schematic depiction of the needle deflection sensing and steering method is shown in Figure 1.3. Needle-tissue interaction models are proposed and used to establish a relationship between needle deflection and the measured force and moment. The two measurements are the only necessary inputs to the virtual deflection sensor. Direct knowledge of tissue parameters is not necessary. The advantage of this method is that these measurements can be readily obtained with a standard force/torque sensor attached to the

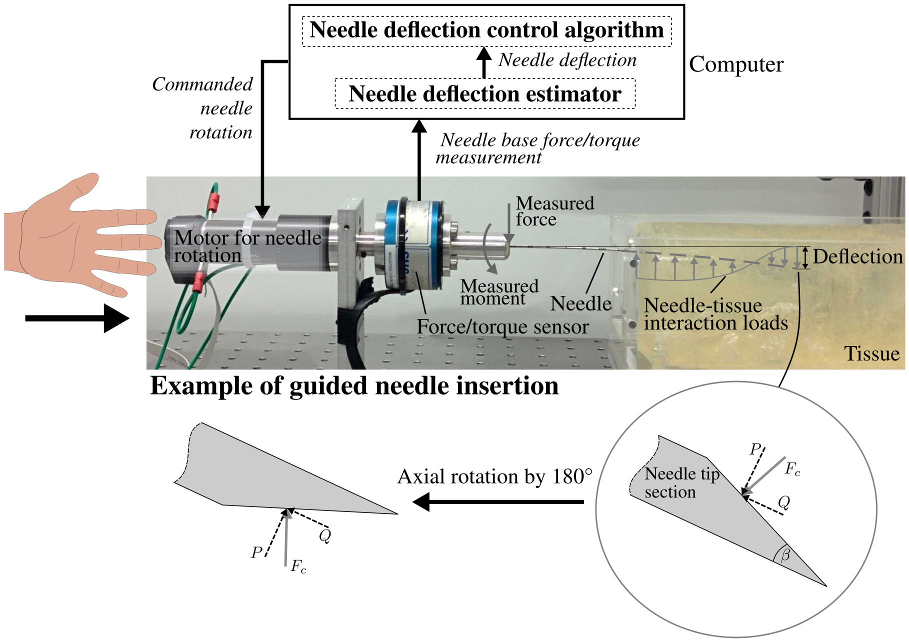

Figure 1.3: Schematic representation of needle deflection sensing and steering.

needle base. The aim to develop a virtual deflection sensor that can estimate needle deflection at a high sampling rate on-line during needle insertion requires a closed-form solution to the deflection modelling problem.

The estimated deflection is then used for needle steering where the estimated needle tip trajectory during insertion is used to parameterize a kinematic model for needle tip deflection. The parameterized kinematic model is then used to predict the insertion depth at which the needle must be rotated by 180° so that a desired target is reached. The parameter estimation and needle steering approach is introduced in Chapter 4.

1.3.2 Lateral Needle Actuation

In the state of the art, the predominantly used method for needle steering is axial needle rotation. This is, however, not the only possible method for needle steering. During prostate brachytherapy, a method for adjusting the needle deflection often used manually by the surgeon is the application of lateral force onto the needle shaft near its entry point into tissue. The force is applied continuously during insertion from a shallow insertion depth onwards to displace the needle shaft laterally. The surgeon uses this technique to reduce the needle deflection by applying the force counter to the direction of needle deflection. A second sce-

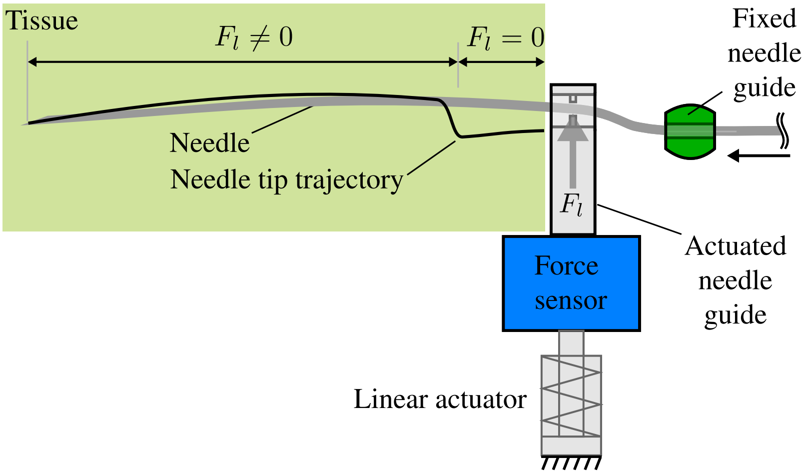

Figure 1.4: A schematic representation of a laterally actuated needle.

nario where lateral force application is used is to reach volumes of the prostate that could not be reached with only bevel-induced needle deflection. An example of such an area is the region of the prostate behind the pubic arch. The pubic arch is a bony obstacle not penetrable by the needle. The surgeon therefore needs to steer the needle behind this obstacle, which in many cases can only be achieved by using lateral force to increase needle deflection beyond the bevel-induced deflection. The second part of this work is concerned with investigating the novel method of automated lateral needle actuation based on the technique manually applied by the surgeon. In order to further the integration of the lateral needle actuation system into prostate brachytherapy and related needle insertion procedures, a system design that replicates the operating room setting is desired. The fundamental design of a lateral needle actuation system is depicted schematically in Figure 1.4. The needle is guided by both a fixed and an actuated needle guide during insertion. While the fixed guide holds the needle in place and prevents it from pivoting, the actuated guide applies a lateral point force onto the needle, which results in lateral displacement of the needle shaft due to the elastic characteristics of tissue. The fixed needle guide represents the guide template currently used in prostate brachytherapy (see Figure 1.1). Throughout the thesis, the application of lateral actuation is considered on a horizontal 2D plane.

A major benefit of automated lateral needle actuation for the purpose of needle steering is the reduction in the amount of tasks that need to be carried out by the surgeon simultaneously. In this work, the overall objective is to investigate lateral needle actuation as an alternative method for robotic needle steering, and to assess the method's potential and limitations. A needle steering control algorithm that uses lateral force and potentially simultaneously axial needle rotation must be able to make control decisions autonomously. This includes informed application of appropriate force magnitudes to steer the needle to a desired target.

An initial experimental study examining the benefits of lateral actuation combined with axial needle rotation with respect to reduction of needle deflection is provided in Chapter 5. To facilitate decision making in real time, a mathematical model of the needle-tissue interaction under lateral force application during insertion is developed in Chapter 6. From the interaction model, a deflection model is derived from which the deflection of a needle that is steered by lateral actuation and axial needle rotation can be estimated and predicted. Moreover, the behaviour of the needle under lateral actuation and the potential benefits of lateral force application with respect to needle steering is investigated through simulations.

In Chapter 7, a control algorithm is then proposed that uses the deflection model introduced in Chapter 6 for needle tip trajectory planning and on-line trajectory adjustment. First, during the trajectory planning phase, the deflection model is used to find a needle tip trajectory that results in an acceptable needle deflection at the final insertion depth. During insertion, this pre-planned trajectory is used as a reference trajectory that the needle tip must follow. An on-line model-based trajectory adjustment algorithm applies lateral force such that the needle tip follows the reference trajectory. The objective of this chapter is to provide an initial control application for the deflection model introduced in Chapter 6, which can be used as a basis for more advanced control algorithms.

The deflection model proposed in Chapter 6 uses the tissue stiffness (Young's modulus) as parameter input. This parameter requirement is common for other needle deflection models found in the literature [20, 21, 30, 32, 26, 35]. While there are various mechanical or image-based methods (e.g., US elastography) readily available to determine the tissue stiffness, these methods often times either require expensive equipment or software. In Chapter 8, a method for intraoperative quantification of tissue stiffness is proposed. The method uses the same actuation system that is used for needle steering. This aims to expand the range of applications for lateral needle actuation while also providing a convenient method for tissue parameter identification that does not significantly interfere with clinical needle insertion. The procedure for tissue stiffness measurement begins with the application of a lateral force of known magnitude onto the needle after it has been inserted to a shallow depth. Subsequently, as the lateral force is held constant, the needle deflection inside and outside of tissue resulting from the force application is measured. Given that the amount of needle deflection and the needle's curvature resulting from the lateral actuation depends on the tissue properties, the tissue stiffness can be deduced.

Throughout the thesis, the various models and control algorithms are validated experimentally. Overall, two major experimental needle insertion setups, one for fully automatic and one for semi-automatic needle insertion have been developed and used for experimental validation. Both systems are introduced in detail in Chapter 2. In particular the semi-automatic insertion setup also serves as an experimental prototype towards incorporating developed robotic assistant systems into clinical needle insertion setups currently used.

Chapter 2

Experimental Robotic Needle Insertion Systems

Two experimental test benches for needle insertion are introduced in this chapter. The primary purpose of the systems is the collection of data for experimental validation of methods introduced in this work such as needle-tissue interaction models, deflection estimation, and needle trajectory prediction and control. The insertion setup introduced in Section 2.1 is designed for fully automatic needle insertion and steering while the one introduced in Section 2.2 is designed to re-create the setup used during prostate brachytherapy procedures and thus also serves as prototype of a surgical assistant system for prostate brachytherapy. Both insertion setups share the same methods for image-based needle deflection measurement introduced in Section 2.3. All setup components are mounted onto an optical breadboard in order to ensure experimental repeatability while providing modularity of the system in case of necessary hardware changes and additions. The design of both below introduced insertion systems is such that the needle always enters tissue perpendicularly. During all needle insertion experiments presented in the following chapters, the needle is pre-inserted by approximately 5-10 mm in order to further guarantee perpendicular entry into tissue and to ensure that an initial needle location can be observed by the ultrasound needle tracking algorithms.

2.1 Automatic Needle Insertion

The experimental test bench shown in Figure 2.1 was designed and built to perform repeatable, fully automated and guided needle insertion into soft tissue. It consists of a 2 degree-of-freedom (DOF) translational-rotational robotic system equipped with a force/torque sensor at the base of the needle and imaging hardware for acquiring camera and US images during needle insertion in soft tissue. The US probe is actuated by a motorized linear stage such that the needle tip can be tracked during insertion.

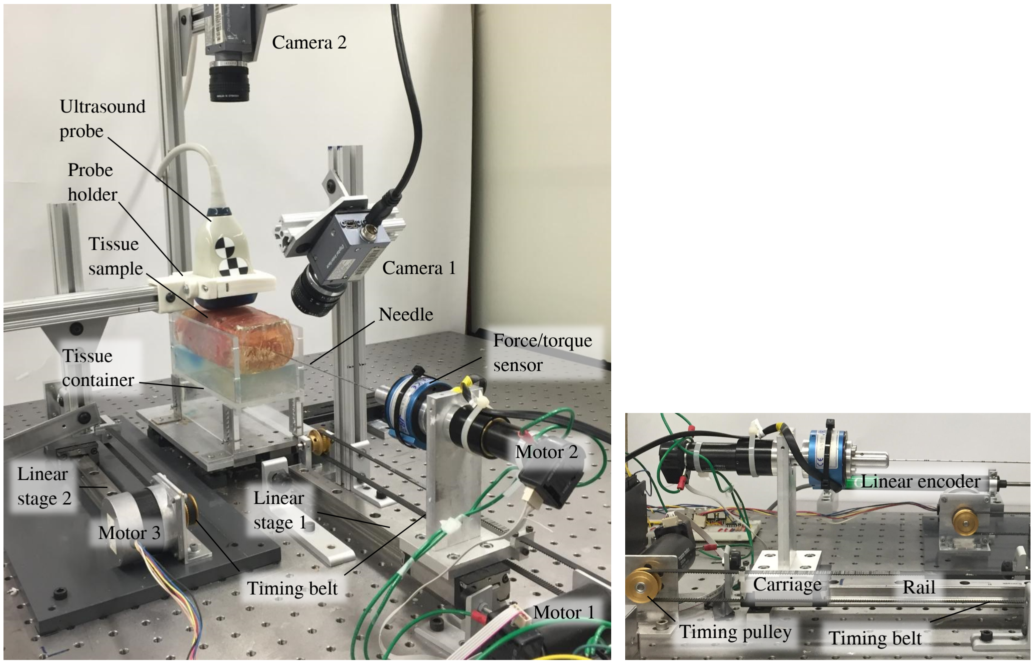

(a) (b)

Figure 2.1: (a) The experimental testbench for performing fully automated needle insertions. A DC motor (Motor 1) provides the linear motion to insert the needle into the tissue. A second motor (Motor 2) attached to the needle base rotates the needle around its axis during insertion. A stepper motor (Motor 3) provides linear motion for the ultrasound probe. The forces at the needle base are measured by a force/torque sensor. Images of the needle inside tissue are recorded by Camera 2. Camera 1 captures close-up images of the needle at its entry point into tissue. (b) A side-view of only the robotic system with force/torque sensor and needle attached to Motor 2.

To measure the tip deflection and shape of the needle within tissue, camera images are recorded and analyzed for insertions into semi-transparent tissue substitutes while ultrasound (US) images are acquired and processed for insertions into non-transparent biological tissue. These measurements can serve as ground truth for experimental validation and real-time control feedback. The imaging hardware and needle tracking software are further detailed in Section 2.3.

The needle, which represents the end-effector of the robot, can be translated along and rotated about its longitudinal axis. The translational motion is guided by a linear stage consisting of a carriage (see Figure 2.1b), which is guided by a rail. The carriage holds the rotational motor (Motor 1, RE40, Maxon Motor AG, Sachseln, Switzerland) with a 14:1 reduction gear (GP 32 A, Maxon Motor AG, Sachseln, Switzerland), the six DOF force/torque sensor (50M31A3-I25, JR3 Inc., Woodland, CA, USA), and the needle. The force/torque sensor's data is filtered by a fourth order Butterworth low-pass filter with a cut-off frequency of roughly 30 Hz. It is actuated by a DC motor (Motor 2, RE40, Maxon Motor AG, Sachseln, Switzerland) via a timing belt. In case the translational stage needs to be driven by hand during manual insertion experiments, the rail-carriage system needs to move freely without the resistance caused by a gear-motor combination. Motor 1 is therefore not equipped with a reduction gear and instead a more powerful motor was chosen, which can directly supply the necessary torque and thus apply sufficient axial force to the needle during insertion.

The mentioned force/torque sensor mounted between the needle and Motor 2 measures shear forces and bending moments occurring at the needle base in two lateral dimensions as the needle bends during insertion into tissue. The sensor also measures axial forces and torques. Its measurements are used to estimate needle deflection during insertion as presented in Chapter 3.

2.2 Semi-automated Needle Insertion

The experimental setup for manual needle insertion including a lateral needle actuation system is depicted in Figure 2.2. It re-creates the setup used during prostate brachytherapy procedures with respect to needle observation methods and hardware such as the grid template. The setup is a prototype of an assistive robotic system for prostate brachytherapy that is designed to extend the current clinical hardware (see Figure 1.1) while at the same time avoiding having to change the basic surgical setup or the procedure. The system is designed to carry out steering actions automatically that would otherwise be carried out manually by the surgeon. The actions to manipulate the needle's trajectory, namely the application of lateral force and axial rotation, can be carried out automatically during insertion. The setup consists of a Hand-held Needle Steering Assistant (HNSA, see Figure 2.3), which was developed by Rossa *et al.* [35] holding a standard 18G brachytherapy needle, a fixed needle guide (needle guide 1) and a second needle guide actuated by linear actuators (needle guide 2) and sensorized through a force/torque sensor mounted at its base. Furthermore, the same actuated ultrasound (US) probe as shown in Figure 2.1a is used for tracking the needle tip inside the phantom tissue sample held by the transparent container.

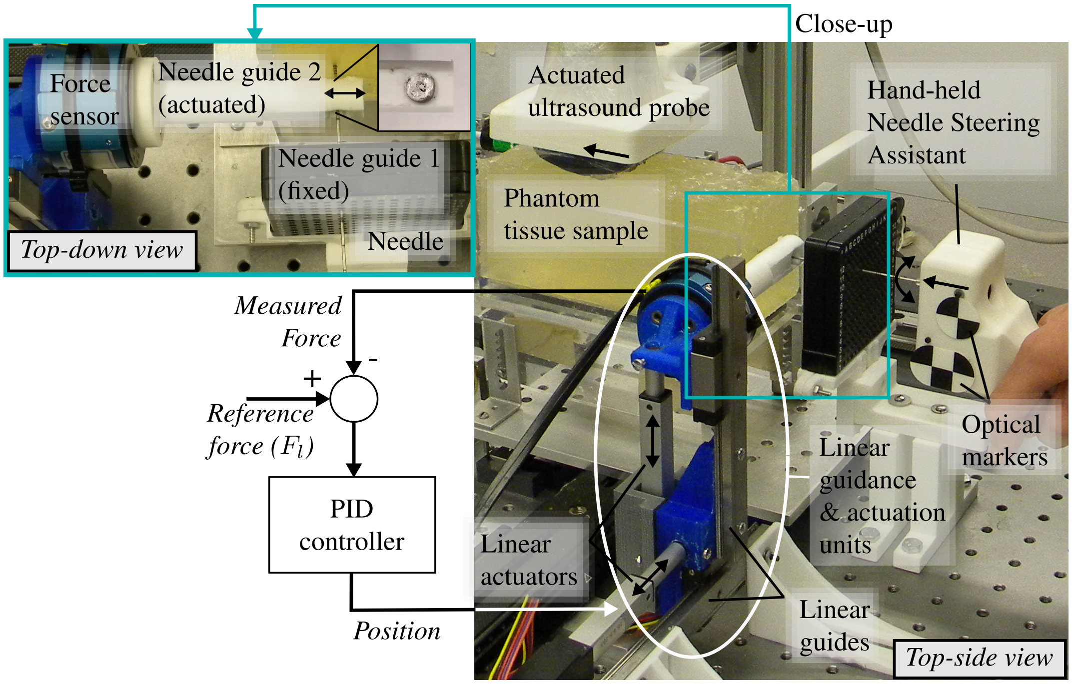

Figure 2.2: The experimental setup used for semi-automated needle insertions. During insertion, lateral force can be applied via linear actuators and the needle can be rotated axially through the Hand-held Needle Steering Assistant [35] at pre-defined insertion depths. The experimental setup re-creates the surgical setup for needle insertion during prostate brachytherapy.

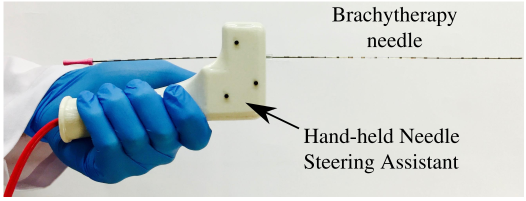

Figure 2.3: The Hand-held Needle Steering Assistant used for manual needle insertion [35].

The HNSA [35] contains a miniature DC motor through which the needle can be rotated axially at a desired insertion depth. Affixed to the side of the HNSA are two optical markers used to continuously track its position during insertion with an optical tracker (MicronTracker, ClaroNav, Toronto, ON, Canada, not included in Figure 2.2). Since the motion tracker is calibrated to the tissue container and the needle is assumed a rigid body in the insertion direction, the current needle insertion depth can be inferred from the measured HNSA location.

Needle guide 2 is a standard variant as used in prostate brachytherapy. It has a thickness of 20 millimetres and the holes are made to fit the 18G brachytherapy needle. As the needle guide 2 is mounted to the breadboard, the needle is restricted from moving laterally and pivoting within the template.

During insertion, the needle is guided by needle guide 1 (fixed) and needle guide 2 (actuated). While guide 1, which resembles the grid template used during brachytherapy, prevents the needle from pivoting, guide 2 is designed to allow the needle to pivot. Needle guide 2 can be displaced laterally to the axial needle direction through two perpendicularly mounted linear guidance and actuation units. Each linear guidance and actuation unit consists of a miniature linear guide (Type SSEBV16-150, MISUMI Group Inc., Tokyo, Japan) and a L16 Miniature Linear Actuator (Actuonix Motion Devices Inc., Victoria, BC, Canada). The units are mounted in serial and confine needle guide 2's motions to a plane normal to the axial needle direction. The forces exerted by the guide onto the needle are measured by a 6 degree-of-freedom (DOF) force/torque (f/t) sensor (50M31A3-I25, JR3 Inc., Woodland, CA, USA). The f/t sensor is used to control the lateral force applied by the actuated guide through a PID force controller. Due to the small hole depth (1.7 mm) of the actuated needle guide the needle can pivot within the guide and friction between guide and needle is negligible.

2.3 Image-based Needle Deflection Measurement

For validation of the needle deflection estimation, the needle shape and tip deflection are measured based on images acquired during insertion into phantom and biological tissue.

2.3.1 Camera-image-based Deflection Measurement

Figure 2.1 depicts a camera mounted near the needle entry point into tissue (Camera 1, SONY XCD-SX90CR, Sony Corporation, Tokyo, Japan) and a second camera (Camera 2, SONY XCD-SX90CR, Sony Corporation, Tokyo, Japan). Camera 2 captures images from a top-down perspective of the inserted needle portion in order to observe the needle shape and tip position during insertion. Camera 1 observes a focused view of the region where the needle enters into tissue for the measurement of sub-millimetre lateral needle motion near

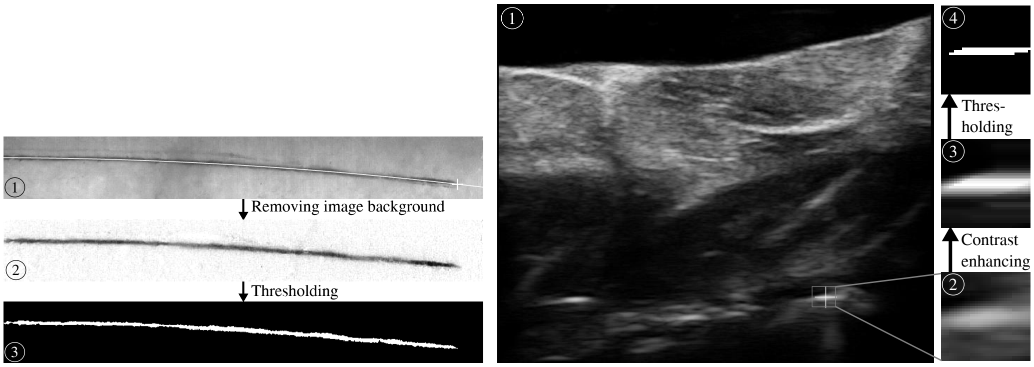

(a) (b)

Figure 2.4: Needle deflection measurement in (a) camera images and (b) axial ultrasound images.

the needle entry point in tissue but is not utilized in this work and therefore the elaboration of image processing algorithms for camera images will only focus on Camera 2.

As the deflection is only observed in the horizontal plane, the needle is steered such that the plane of deflection is parallel to the imaging plane. For the transparent phantom tissue, camera images acquired from Camera 2 are used to measure the needle tip deflection trajectory and the shape of the deflected needle shaft during insertion. The US probe shown in Figure 2.1 is removed for experiments involving Camera 2.

For experiments with non-transparent biological tissue, US images are acquired to measure needle tip deflection and shape. Both the needle shaft's shape and tip trajectory are recorded as they can differ due to tissue compression and deformation.

In case of insertion experiments in transparent phantom tissue, images of the needle are continuously taken throughout insertion by Camera 2. Algorithm 2.1 presents the method for needle shape and tip deflection measurement.

Figure 2.4a shows three images depicting the extraction of the needle contour. In image 1, the fitted needle shape and the measured tip position are shown by a line and a cross, respectively. Image 2 corresponds to `img_diff` and image 3 corresponds to `img_bw` as described in Algorithm 2.1. The camera model used to map the three-dimensional space to the image domain is a pinhole camera model. The millimetre-to-pixel ratio for Camera 2 is 0.192 mm/pixel.

Algorithm 2.1 Needle shape & tip position measurement from camera images

```
function PROCESS_IMAGES(img_set)
    for $i = 1$ to len_img_set do
        Removing image background:
        img_diff ← img_set($i$) - img_set(1)          ▷ Take difference between current & initial image
        thres ← max(img_noise) + $\epsilon$
        img_bw ← im2bw(img_diff, thres)               ▷ Convert to binary image
        Obtaining needle shape:
        pnt_cloud ← img_bw                            ▷ Convert img_bw (needle contour) to point cloud
        p_coef ← polyfit(pnt_cloud,2)                 ▷ Fit polynomial to pnt_cloud
        Detecting needle tip position:
        $x \leftarrow 0$                              ▷ Init image column counter
        win ← ones(len_win, 1)                        ▷ Init window win
        thres_sum ← len_win * 0.05
        while sum(win) > thres_sum do
            $x++$
            $y$ ← polyval(p_coef, $x$)
            win ← [img_bw($y$,$x$) win(1:len_win-1)]  ▷ Move win one horizontal pixel forward
        end while
        array_pos_tip(i,:) ← [ $y$ $x$ ]
    end for
    return array_pos_tip
end function
```

In order to find the needle shape in the images acquired by Camera 2, the needle contour is first extracted from the image background (initial image, `img_set`(1)). The fact that no needle is present in the initial frame is exploited to remove the background from a frame with needle by subtracting the initial frame from the current frame. A threshold is applied to the differential image to obtain a binary image `img_bw` of the needle contour. `img_bw` is then converted into a point cloud and a polynomial is fitted to the points by using a least-squares approach. To find the needle tip, a window (`win`) of a pre-defined length is moved along the polynomial fit in the binary image `img_bw`. The tip is detected when the amount of pixels in `win` with value 1 is smaller than a pre-defined threshold, meaning that the needle's distal end has been reached. The above moving window method is used as it is robust against possibly occurring gaps in the extracted needle contour.

2.3.2 Ultrasound-image-based Deflection Measurement

The US probe (4DL14-5/38 Linear 4D, Ultrasonix, Richmond, BC, Canada) is mounted onto a linear stage via a crossbar structure, which is aligned parallel to the tissue container and actuated by a DC motor (see Figure 2.1, Linear stage 2) via a timing belt. Thus, the probe is restricted to move along the tissue in the direction of needle insertion. The position of the

US probe is controlled such that it follows the needle tip during insertion using the relative position of either the carriage of Linear stage 1 (see Figure 2.1) or the HNSA captured by the optical tracker (see Figure 2.2) as a reference. A diagnostic US system (SonixTOUCH, Ultrasonix, Richmond, BC, Canada) is used to generate US images from the sonography data acquired by the US probe. The US system records axial images of the needle inside tissue in order to track the needle tip position during insertion.

The images generated by the US system, in which the needle cross-section is marked as a bright spot, are processed with a needle tracking algorithm. Image 1 in Figure 2.4b shows an axial US image. In the early work (Chapters 3-4), the algorithm used to track the needle in the ultrasound image was developed by Waine *et al.* [51]. Within the image, a region of interest (ROI) is marked around the bright spot representing the needle cross-section (see Figure 2.4b, image 2). The white cross within the ROI indicates the needle position detected by the algorithm. In Figure 2.4b, images 2, 3 and 4 illustrate the sequence of image processing applied by the algorithm in order to extract the needle cross-section. Before insertion is started, the initial ROI position is supplied by the user. In each subsequent US image, the ROI position is updated around the detected needle position in the previous image. Next, the algorithm uses an Intensity Transform to enhance the image contrast (see Figure 2.4b, image 3). This is followed by the identification and application of a threshold on the ROI to obtain a binary image containing a blob representing the needle cross-section (see Figure 2.4b, image 4). The centre point of the cross-section is finally found by taking the horizontal and vertical median of image 4. The millimetre-to-pixel ratio for US images is 0.064 mm/pixel.

In more recent work, (Chapters 5-8) an algorithm developed by Carriere, which is a modified version of the one introduced by Carriere *et al.* [52], is used to track the needle cross-section for needle deflection measurement. The new algorithm was used as it is able to track the needle more robustly even in the presence of a high amount of image noise.

For some of the experimental studies presented in this thesis, the shape of the needle at the final insertion depth is analyzed and thus needs to be measured. This is done after the needle insertion is stopped when reaching the final insertion depth. The US probe is moved back from the needle tip with a constant velocity to its initial position. As the probe moves back, images of the needle cross-section within tissue are captured by the US system in order to capture the needle shaft's *shape* inside tissue.

Chapter 3

Force/torque-based Deflection Estimation

For on-line needle trajectory control, a needle deflection measurement or estimate is necessary as feedback. In this chapter, an approach for needle deflection estimation is introduced and further improved, which does not rely on imaging modalities or tissue parameters. Section 3.1 provides the background to and related work on the deflection estimation method. In Section 3.2, a force/torque-based deflection estimation method is introduced based on simplified needle-tissue interaction modelling. In Section 3.3, the modelling is refined with the objective to model the needle-tissue interaction in a more adaptive manner such that the estimation error is further minimized.

3.1 Background and Related Work

Figure 3.1 depicts schematically the clamped needle with modelled interaction loads between needle and tissue during insertion. As the needle penetrates tissue, the needle tip cuts tissue and causes tissue displacement, which in turn causes a reaction load enacted by the tissue onto the needle's bevel surface [14]. This load F_c is commonly modelled as a point load acting at the bevel surface's centre. The point load F_c, which will henceforth be referred to as the cutting force, is the initial cause for needle deflection. As a result of deflection, the needle applies lateral pressure onto the tissue along its inserted portion. The elastic properties of the tissue then cause it to enact a reaction load onto the needle. This reaction is modelled in a general form as the distributed load $q_d(z)$ (see Figure 3.1) where z is the horizontal coordinate parallel to the direction of insertion.

Several modelling approaches for force interactions between needle and tissue have been proposed, for deflection estimation. Among those are mechanics-, Finite-Element-Method (FEM)-, kinematics- and statistics-based models. An initial investigation into the types of force interactions occurring between the needle and tissue was conducted by Okamura *et*

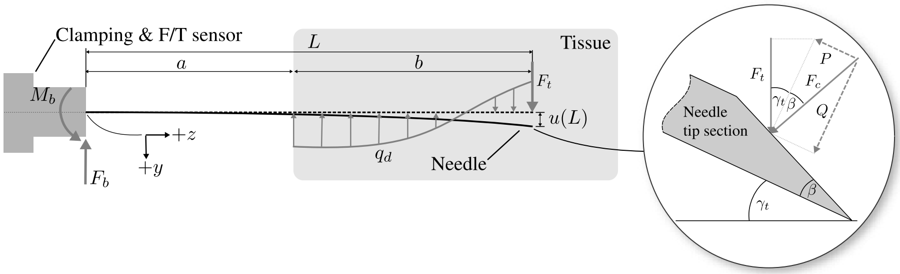

Figure 3.1: The needle and applied tissue reactions modelled as a distributed load q_d and point load F_t. L is the needle length, a and b are the needle portions outside and inside of tissue, respectively. M_b and F_b represent moment and force, respectively, measured at the needle base. The close-up view of the needle tip on the right side shows forces acting at the needle tip during insertion into tissue. Q and P are the transverse and axial components of F_c respectively and F_t is the projection of Q along the vertical coordinate z. γ_t is the tip deflection slope.

al. [14]. The identified physical needle-tissue interactions are stiffness before puncture, and friction and cutting force after puncture.

The first quasi-static mechanics-based needle-tissue interaction model [13] developed for the estimation of needle tip deflection considers the tissue deformation as a uniform distribution along the inserted needle portion. The load is assumed to act in the same direction as the deflection and is caused by tissue displacement of the bevel tip. A model that establishes a relation between needle base force and the deflection is then derived. The model underestimates needle deflection, which was attributed to the model underestimating needle bending outside of tissue. Using force interactions between needle and tissue such as cutting force and tissue support, and force/torque measurements at the needle base, Abolhassani *et al.* [15, 17] established a relationship to needle deflection where a triangularly distributed load q_d, which weakens towards the needle tip, is assumed. Thereby, the tissue is assumed to act as a support while the needle is pushed towards the direction of deflection during insertion. Tissue reaction is assumed to be negligible and hence it is neglected in [17]. Only considering a tip cutting force as done in [17], however, contradicts the finding that the tip cutting force is constant [14], as the needle deflection increases with insertion depth.

In Lehmann *et al.* [31], distributed interaction loads along the needle are incorporated into interaction modelling. Two triangularly distributed loads are considered to act along the needle shaft. The first distributed load is the same as modelled in [17]. The second distributed load is also a triangularly distributed load with opposite direction and distribution intensity profile. The maximum force of distributed load two is at the needle tip and decreases towards the entry point. The second load assumption is based on the fact that the needle stores potential energy in its bent state, which results in a pressure applied onto the tissue in the upward direction, which in turn causes the tissue reaction pointing in the direction of deflection. The assumptions, however, do not take into account the force caused by the needle tip cutting tissue. In Abayazid *et al.* [23], a point load and a uniformly distributed load along the inserted portion of the needle are assumed. The concentrated force acts at the needle tip in the same direction as the deflection. As in the previous work [17], the point load is understood to be the tip cutting force.

Some of the above models and models introduced in Section 1.2 take tissue parameters as inputs, which are typically hard to characterize. Other models provide an accurate deflection estimate but only up to a limited insertion depth. Here, we further advance the estimation of tip deflection and shape of the needle shaft such that a more robust deflection estimate can be obtained.

In Section 3.2, various load assumptions along the needle shaft are introduced and evaluated with regards to the estimation performance. The assumed load distributions are reduced to point loads for model simplification. In Section 3.3, the modelling of needle-tissue interactions is further extended to a more adaptive modelling approach as it is likely that during insertion, the shape of the load distribution changes.

3.2 Deflection Estimation Based on Preliminary Modelling of Needle-tissue Interactions

3.2.1 Needle Deflection Models

This section introduces models for needle-tissue interaction. The underlying methodology, which relates the force/moment equilibrium in the static case to the deflection of a beam is introduced. In the proposed model, there are two steps for estimating the deflection namely 1) writing the force and moment balance equations for the modelled loads along the needle and 2) subjecting the deflection model of the cantilever beam to these loads. The individual steps are described in the following three subsections. Needle deflection at each insertion step can then be calculated.

Two different distributions for the force exerted by the tissue onto the needle are considered in this section, namely uniform and triangular distributions which serve as the basis for three different deflection models. These considerations are further explained in the following subsections.

Model 1: Two Triangularly Distributed Loads

This model was introduced by Lehmann *et al.* [31]. It is based on the assumption that two triangularly distributed loads act along the portion of the needle that is in contact with tissue. The model is shown in Figure 3.2a.

The projection of the needle in tissue along its axis (z) is called L. Also, a and $b = L - a$ are the needle portions that are outside and inside of tissue, respectively. The difference between the physical needle length and its projection along z as it bends (i.e. L) is considered to be negligible. The resultant force and moment induced by the needle-tissue interaction forces at point A are F_R and M_R, respectively, which are measured by a force/torque sensor. The distance between the needle base and the point A is c.

Since the sensor measures moments around its centre and the bending moments of interest for force-sensor-based deflection estimation are the ones occurring at the needle clamping's tip, the measured moments need to be re-calculated to account for the length of the clamping: $M_b = M_R - F_b c$ where $c = 52.75$ mm is the distance between the sensor's centre and the needle clamping's tip. The needle tip deflection is called u_t.

As the needle bends while being inserted into tissue, it compresses the tissue below the needle as shown in Figure 3.2a. The force applied by the compressed tissue is assumed to form a triangularly distributed load $q_{tr,1}$. The assumption is that as the needle bends, it increasingly compresses tissue below the needle. Therefore, it is reasonable to assume that the tissue applies the highest reaction force at the needle entry point and the least reaction force at the needle tip [17]. Consequently, $q_{tr,1}$ is assumed to be at its maximum at the needle entry point and at its minimum at the needle tip. According to beam theory [86], $q_{tr,1}$ can be replaced by a point load $F_{tr,1}$ at the centroid of $q_{tr,1}$ at point B (see Figure 3.2a). The centroid and thus $F_{tr,1}$ is located at 1/3 of the inserted needle length b. Above the needle,

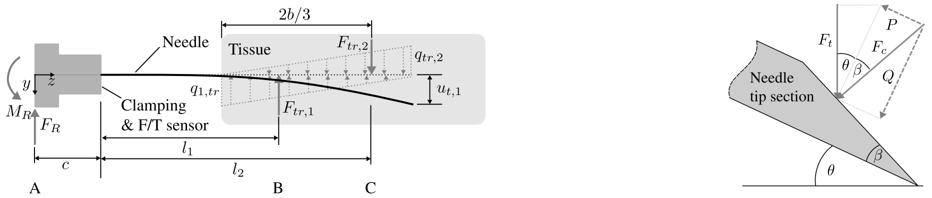

(a) Model 1: Two triangularly distributed loads.

(b) Needle tip forces.

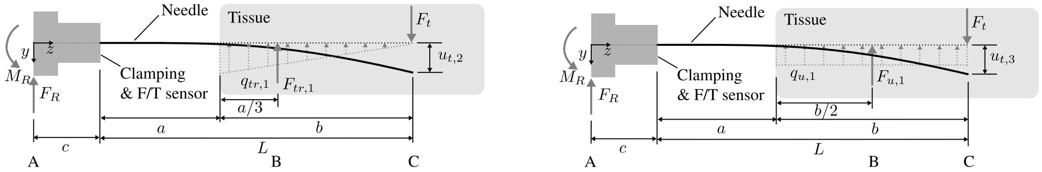

(c) Model 2 with above force (F_t) at the tip.

(d) Model 3 with uniformly distributed load below.

Figure 3.2: Needle-tissue interaction model. (a) The assumed tissue loads acting on the needle are $q_{tr,1}$ and $q_{tr,2}$. $q_{tr,1}$ and $q_{tr,2}$ are triangularly distributed loads that can be replaced by the point loads $F_{tr,1}$ and $F_{tr,2}$, respectively. The measured force and moment at the point A are F_R and M_R. The distance between A and the needle base is c. The projection along z of the total needle length, and of the portions of the needle inside and outside the tissue respectively are L, b and a. The tip deflection is called u_t. (b) Forces acting on the needle tip during insertion. F_c is the force normal to the needle bevel, Q and P are the transverse and axial component of Q respectively and F_t is the projection of Q along y. β is the bevel angle and θ is the deflection slope. (c) A proposed model variant of (a) with $q_{tr,2}$ changed to the point load F_t acting at the needle tip. (d) The load $q_{tr,1}$ in (c) was changed to the uniformly distributed load $q_{u,1}$.

however, the triangular load distribution $q_{tr,2}$ is assumed because the needle stores potential energy in its bent state, which results in a pressure applied onto the tissue in the upward direction, which causes a downwards pointing tissue reaction ($q_{tr,2}$). Here, the point load $F_{tr,2}$ replacing $q_{tr,2}$ is placed at 2/3 of b.

In order to relate the measured force and moment F_R and M_R to the loads $F_{tr,1}$ and $F_{tr,2}$ acting along the needle, the force and moment balance equations need to be established. The balance of moments and forces acting at point A gives

$$0 = -M_R + F_{tr,1}(l_1 + c) - F_{tr,2}(l_2 + c) \tag{3.1}$$

$$0 = -F_R + F_{tr,1} - F_{tr,2} \tag{3.2}$$

with

$$l_1 = a + b\gamma_1 \text{ and } l_2 = a + b\gamma_2 \tag{3.3}$$

where $\gamma_1 = 1/3$, $\gamma_2 = 2/3$ and c is the distance between the needle base and the origin of the force sensor's frame as shown in Figure 3.2. The unknown forces $F_{tr,1}$ and $F_{tr,2}$ can now be found by using (3.1) and (3.2):

$$\begin{bmatrix} F_{tr,1} \\ F_{tr,2} \end{bmatrix} = \begin{bmatrix} 1 & -1 \\ l_1 + c & -(l_2 + c) \end{bmatrix}^{-1} \begin{bmatrix} F_R \\ M_R \end{bmatrix} \tag{3.4}$$

The deflection generated by $F_{tr,1}$ and $F_{tr,2}$ can now be calculated by modelling the needle as a cantilever beam undergoing these loads. The needle deflection is calculated in the static case in each discretized insertion step starting from the unbent needle. The deflection model is a static cantilever beam model based on the Euler-Bernoulli beam theory. For a beam experiencing an overall load of $q(z)$, also known as the forcing term, along its longitudinal axis z with respect to the needle's base, the deflection $u(z)$ in the y direction is governed by

$$\frac{d^2}{dz^2}\left(EI\frac{d^2u(z)}{dz^2}\right) = q(z) \tag{3.5}$$

where E and I are the Young's modulus and area moment of inertia of the needle. As we have two loads acting on the needle (see Figure 3.2), in order to obtain the overall tip deflection, the deflections caused by each force are separately calculated and superimposed. The deflections ($u_{1,tr}(L)$ and $u_{2,tr}(L)$) caused by the forces $F_{tr,1}$ and $F_{tr,2}$ can be computed as:

$$u_{1,tr}(L) = \frac{(3L - l_1)l_1^2}{6EI}F_{tr,1} \tag{3.6}$$

$$u_{2,tr}(L) = \frac{(3L - l_2)l_2^2}{6EI}F_{tr,2} \tag{3.7}$$

where l_1 and l_2 are defined by (3.3). Finally, the resulting tip deflection $u_{t,1}$ at the needle tip is [86]:

$$u_{t,1} = u_{1,tr}(L) + u_{2,tr}(L) \tag{3.8}$$

Model 2: A Triangularly Distributed Load and Cutting-induced Point Load

This model considers the cutting-induced point load at the needle tip F_t. The origin of F_t is shown in Figure 3.2b, which illustrates the forces acting at the needle tip during insertion into tissue. As the needle is inserted, the force F_c is applied by tissue at the needle tip, in a direction perpendicular to the needle bevel surface. The force F_c can be decomposed into its transverse component Q and axial component P which depend on the needle bevel angle β. The transverse force component Q causes the needle to bend as it is inserted into the tissue. The influence of the axial force component P on the deflection is neglected as it predominantly causes very small longitudinal compression of the needle. The relation between F_t and Q is given by $F_t = Q\cos\theta$ where θ is the needle bending angle at its tip, which is considered to be very small.

As the needle penetrates into the tissue and deflects in the direction of F_t, it applies pressure onto the tissue. As in Model 1, a triangularly distributed load is considered below the needle. The force distribution model is shown in Figure 3.2c. In this model, $q_{tr,1}$ is again replaced by a point load and (3.6) can be applied to calculate the tip deflection component $u_{1,tr}(L)$. The deflection $u_2(L)$ caused by F_t is:

$$u_2(L) = \frac{L^3}{3EI}F_t \tag{3.9}$$

The resulting deflection $u_{t,2}$ is the combination of (3.6) and (3.9):

$$u_{t,2} = u_{1,tr}(L) + u_2(L) \tag{3.10}$$

Model 3: A Uniformly Distributed Load and Cutting-induced Point Load

In this model we consider the cutting-force-related load for the portion of the tissue above the needle F_t as presented in Model 2. In contrast to Model 2, in this model the reaction of the compressed tissue below the needle (see Figure 3.2d) is assumed to have a uniform distribution along the portion of the needle that is inside the tissue [20]. This reaction is modelled as a load per length $q_{u,1}$. According to beam theory [86], the uniformly distributed load $q_{u,1}$ can again be replaced by the point load $F_{u,1}$ at the centroid of $q_{u,1}$, which is at point B. For a uniformly distributed load, the point B is placed at 1/2 of b.

The deflection caused by $F_{u,1}$ is

$$u_{1,u}(L) = \frac{(3L - l_1)l_1^2}{6EI}F_{u,1} \tag{3.11}$$

where l_1 is defined by (3.3) with $\gamma_1 = 1/2$. The total tip deflection $u_{t,3}$ is given by (3.9) and (3.11):

$$u_{t,3} = u_{1,u}(L) + u_2(L) \tag{3.12}$$

3.2.2 Experimental Results

Insertion experiments are carried out with the experimental setup presented in Section 2.1. The phantom tissue used for the experiments is made from agar of type *A360-500* (Fisher Scientific International Inc., Hampton, NH, USA). The stiffness of the agar phantom tissue can be adjusted by the ratio of agar to water used. Two different tissue samples are used. The agar per litre of water mixtures for Tissue 1 and Tissue 2 are 45 g and 22.5 g, respectively. This means that Tissue 1 is stiffer than Tissue 2. The insertions are performed at two constant insertion velocities of 20 mm/s and 60 mm/s. The insertion depth for all experiments is set to 135 mm as this is a common insertion depth for prostate brachytherapy procedures. The used needle type is a standard 18-gauge prostate seeding needle of length 200 mm (Eckert & Ziegler BEBIG, Inc. Oxford, CT, USA). The material of the needle is stainless steel, which has a Young's modulus E of 200 GPa. The needle's area moment of inertia I is 7.86×10^{-14} m^4.

Figure 3.3a to Figure 3.3d show the tip deflection estimation results ($\hat{u}_t$) versus the image-based measured tip deflection u_t for all three models. Each plot contains the results of one tissue-velocity combination and shows the mean tip deflection (estimated and measured) for three trials for each tissue-velocity combination. The deflection data is smoothed by a Savitzky-Golay low-pass filter of order 2 [87] where the MATLAB implementation `sgolayfilt` is used. The plots also show the error between the estimated and the measured tip deflection $u_t - \hat{u}_t$ for each of the three compared models. Table 3.1 presents the mean absolute error (MAE = $\frac{1}{k}\sum_{i=1}^{k} |u_{t,i} - \hat{u}_{t,i}|$ where k is the amount of samples considered) and the mean $|\bar{u}_t|$ of the three trials, and the standard error $\sigma/\sqrt{n}$, where σ is the standard deviation and n is the number of runs. These parameters are shown for all tissue-velocity combinations and the points where the needle reaches depths of 60 mm and 120 mm during insertion.

For deflection estimations up to a depth of 60 mm, all models maintain a low estimation error ($|u_t - \hat{u}_t| < 1$ mm) except for minor fluctuations, which can be attributed to the

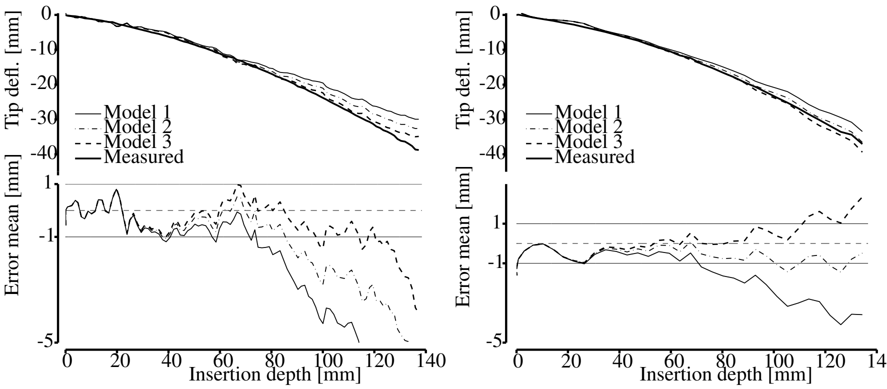

(a) Tissue 1, insertion velocity: 20 mm/s. (b) Tissue 1, insertion velocity: 60 mm/s.

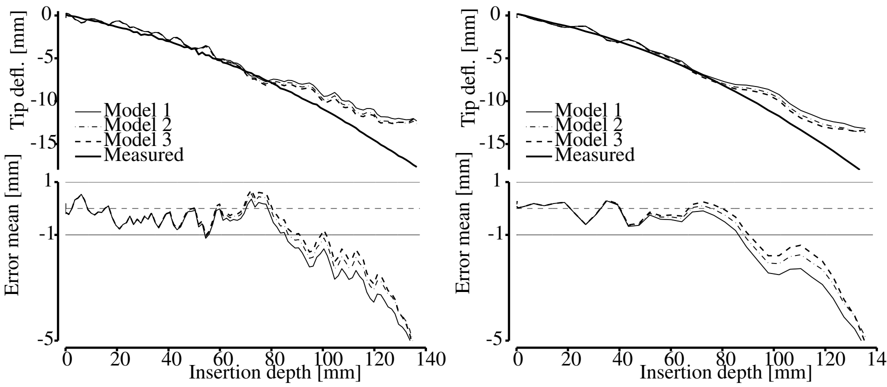

(c) Tissue 2, velocity: 20 mm/s. (d) Tissue 2, velocity: 60 mm/s.

Figure 3.3: The mean curves of three runs with each of two tissue samples and two insertion velocities. The error plot shows the relative error between measured and estimated deflection ($u_t - \hat{u}_t$). The measured deflection u_t is calculated based on camera images.

remaining data noise. When, however, the insertion exceeds a depth of 60 mm, all models begin to under-estimate the tip deflection. The sole exception is for Tissue 1 and velocity 60 mm/s where the estimation shows after a depth of 60 mm the highest precision among all tissue-velocity combinations.

Based on Figure 3.3a to Figure 3.3d, Model 3 performs the best in almost all trials. Especially for Tissue 1, Model 3 shows the best performances with relatively small estimation errors compared to Model 1 and Model 2. The worst performance is shown by Model 1 in all of the trials. This result strongly suggests that the newly developed model (Model 3) represents a significant improvement over the initially proposed model (Model 1) in [31]. As can be observed in Figure 3.3a to Figure 3.3d, at the final insertion depth of 135 mm, the tip deflection in Tissue 1 is roughly that in Tissue 2. This shows that the phantom tissue

Table 3.1: Mean absolute error (MAE), absolute mean ($\lvert \bar{u}_t \rvert$) and standard error ($\sigma/\sqrt{n}$) for all models at two insertion depths. Units are in mm.

		Tissue 1						Tissue 2					
Model #	Insertion depth	20 mms^{-1}			60 mms^{-1}			20 mms^{-1}			60 mms^{-1}		
		MAE	$\lvert \bar{u}_t \rvert$	$\sigma/\sqrt{n}$	MAE	$\lvert \bar{u}_t \rvert$	$\sigma/\sqrt{n}$	MAE	$\lvert \bar{u}_t \rvert$	$\sigma/\sqrt{n}$	MAE	$\lvert \bar{u}_t \rvert$	$\sigma/\sqrt{n}$
1	60 mm	0.56	10.49	0.34	**0.38**	10.81	0.27	0.36	5.17	0.84	0.28	4.88	0.12
2	60 mm	0.46	10.91	0.36	0.47	11.25	0.28	**0.34**	5.27	0.85	0.26	4.98	0.13
3	60 mm	**0.39**	11.23	0.37	0.54	11.59	0.29	**0.34**	5.35	0.86	**0.25**	5.05	0.14
1	120 mm	1.58	26.14	0.56	0.79	28.34	0.59	0.87	11.25	0.38	0.79	12.17	0.74
2	120 mm	0.96	28.46	0.60	**0.39**	30.86	0.67	0.75	11.73	0.40	0.64	12.73	0.83
3	120 mm	**0.49**	30.65	0.65	0.89	33.25	0.76	**0.67**	11.96	0.42	**0.55**	13.04	0.91

stiffness is significantly different for Tissue 1 and Tissue 2. Despite this high variance in tissue properties, Model 3 does not lose precision. This suggests that the model is robust against varying tissue stiffness. Table 3.1 backs up the above observations. The MAE of Model 3 stays well below 1 mm over all four tissue-velocity combinations for the insertion depth of 60 mm. Although the MAE values are very similar for all models across the varying experimental conditions, Model 3 shows the lowest MAE except for the combination Tissue 1 and velocity 60 mm/s. This remains the case at an insertion depth of 120 mm.

In order to show the consistency of the experimental results across the three trials, the standard errors at depths 60 mm and 120 mm are shown in Table 3.1. The low values observed throughout the experiments indicates a high consistency for each tissue-velocity combination.

A limitation of Euler-Bernoulli beam theory and therefore for the deflection estimation approach presented here is that its accuracy is limited to small deflections such as 10% of the overall beam length. Furthermore, the maximum deflection slope should not exceed 5% of the overall needle length. Thus, the fact that the maximum needle deflection observed in this section is greater than the aforementioned small deflection requirement can be a cause of error at higher insertion depths.

3.3 Deflection Estimation Based on Refined Modelling of Needle-tissue Interactions

In the above results (Section 3.2.2), it can be observed that the error between tip deflection estimate and measured deflection increases with higher insertion depth. It is likely that during insertion, the shape of the load distribution changes. As the shapes of the load distributions previously proposed in [13, 31] and Section 3.2 are limited to a uniform or triangular distribution, the model cannot adjust to more complex needle-tissue interaction loads. Hence the need exists to dynamically change the load distribution.

For this purpose, in this section, a novel generalized model is developed, within which distributed loads of arbitrary polynomial shapes can be introduced. The goal is to further enhance the deflection estimation capability over a range of tissue stiffness and non-homogeneities while only considering measurements of force and moment at the needle base as model inputs. To this end, a differential equation based on Euler-Bernoulli beam theory is used to represent the static system of the clamped needle, which is subject to the modelled tissue loads. This equation is then integrated four times in order to obtain a closed form solution for shear force, bending moment, slope and finally deflection at any point along the needle. The following sections introduce the model and present results of estimation performance during needle insertion into gelatin phantom and ex-vivo porcine tissue.

3.3.1 An Adaptive, Quasi-Static Model for Needle-tissue Interactions

This section introduces the formulation for an adaptive model of needle-tissue interactions during needle insertion into tissue. The model is then used in Section 3.3.2 to obtain an estimate of the needle deflection.

Modelling of Interaction Loads

The needle-tissue interactions, which cause the needle to bend, are represented as a distributed load q_d along the inserted needle portion and a point load F_t at the needle tip as depicted in Figure 3.1. Both q_d and F_t are discontinuous in space. q_d only acts where the needle is surrounded by tissue and is therefore modelled to have a discontinuity at the needle entry point into tissue. A widely used method to model loads of this kind involves singularity functions [88], i.e.,

$$q(z) = \frac{q_0}{b^n}\langle z - a\rangle^n; \quad n = 0, 1, 2, ... \tag{3.13}$$

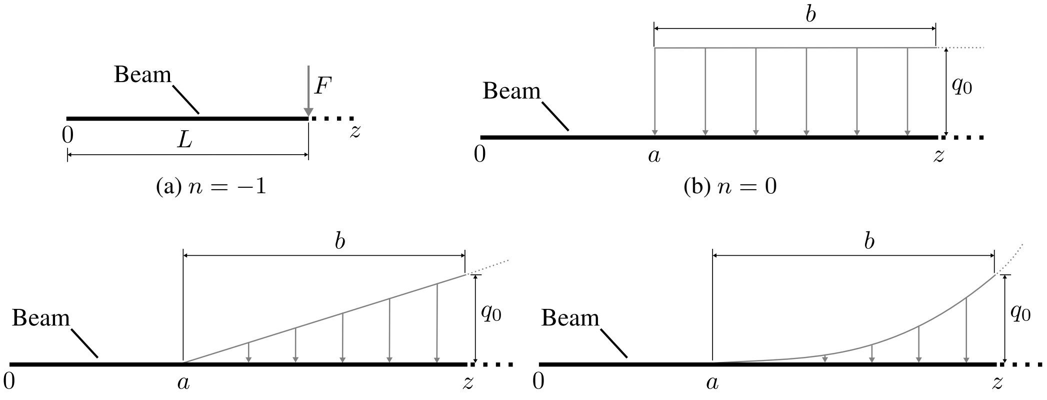

(a) $n = -1$ (b) $n = 0$ (c) $n = 1$ (d) $n = 2$

Figure 3.4: A schematic representation of (a) a point load, (b) a uniform, (c) a triangular and (d) a parabolic load distribution. a is the shift from zero and q_0 is the load magnitude at the variable distance z along the beam.

with

$$\langle z-a\rangle^n = \begin{cases} 0 & \text{when } z \le a \\ (z-a)^n & \text{when } z > a \end{cases} \text{ if } n = 0,1,2,... \qquad \begin{cases} +\infty & \text{when } z = a \\ 0 & \text{when } z \ne a \end{cases} \text{ if } n = -1 \tag{3.14}$$

where a is the shift from zero.

Distributed load q_d Four examples of loads which can be modelled with the above approach are shown in Figure 3.4. The mathematical forms associated with the load examples are $F\langle z-L\rangle^{-1}$ for Figure 3.4a, $\frac{q_0}{b^0}\langle z-a\rangle^0$ for Figure 3.4b, $\frac{q_0}{b^1}\langle z-a\rangle^1$ for Figure 3.4c and $\frac{q_0}{b^2}\langle z-a\rangle^2$ for Figure 3.4d with the loads being shifted about a. The maximum load intensity q_0 acts at a point $z > a$. The parameter b refers to the distance from point $z = a$ at which the value q_0 is defined.

More complex polynomial load shapes of any order m can be formulated as superpositions of (3.13):

$$q(z) = \sum_{i=0}^{m} \frac{q_i}{b^i}\langle z-a\rangle^i \tag{3.15}$$

where q_i is the magnitude of the load expressed by the i^{th} term at z. When (3.15) is used to model the distributed load q_d along the inserted needle portion as illustrated in Figure 3.1, a becomes the portion of the needle outside tissue, and b represents the needle portion inside tissue. The general formulation for q_d in (3.15) is advantageous as any polynomial shape can be modelled. The integrability of (3.15) is later used to derive the analytic solution to the beam deflection formulation, which models needle deflection.

Point load F_t As F_t acts as a point load, it is commonly modelled as a shifted Dirac delta function. The point load F_t related to the cutting force F_c at $z = L$, the needle tip, is modelled as

$$q_t(z) \quad = \quad F_t\langle z-L\rangle^{-1}. \tag{3.16}$$

The Needle-Tissue Interaction Model

The needle is modelled as a cantilever beam, which is subject to the above described loads. Euler-Bernoulli beam theory is used to obtain a governing equation for the needle-tissue system. The resulting equation is a fourth-order ordinary differential equation (ODE). The right hand side of the ODE consists of the applied loads enacted by tissue onto the needle. The analytic formulation for the needle deflection is derived in the following.

The ODE governing the needle-tissue system is

$$\frac{d^2}{dz^2}\left(EI\frac{d^2u}{dz^2}\right) = q_d(z) + q_t(z) = \sum_{i=0}^{m}\frac{q_i}{b^i}\langle z-a\rangle^i + F_t\langle z-L\rangle^{-1} \tag{3.17}$$

where u is the needle deflection along the y-axis (see Figure 3.1), E is the needle's Young's modulus and I is the needle's area moment of inertia. In order to obtain the deflection u, which results from the applied loads $q_d(z)$ and $q_t(z)$, (3.17) is integrated four times with respect to z. The first integration of (3.17) gives the shear force $V(z)$ along the needle:

$$\begin{aligned} -V(z) = \frac{d}{dz}\left(EI\frac{d^2u}{dz^2}\right) &= \int q_d(z) + q_t(z)\; dz \\ &= \sum_{i=0}^{m}\frac{q_i}{b^i(i+1)}\langle z-a\rangle^{i+1} + F_t\langle z-L\rangle^0 + C_1. \end{aligned} \tag{3.18}$$

The boundary condition used to obtain the integration constant C_1 in (3.18) is the shear force at the needle tip ($z = L$) being equal to zero. Therefore, $V(L) = 0$ and

$$-V(z) = \sum_{i=0}^{m} \frac{q_i}{b^i(i+1)} \langle z-a \rangle^{i+1} - \underbrace{b \sum_{i=0}^{m} \frac{q_i}{(i+1)}}_{d_1} - F_t. \tag{3.19}$$

Integration of (3.19) gives the bending moment $M(z)$ along the needle:

$$-M(z) = EI\frac{d^2u}{dz^2} = \sum_{i=0}^{m} \frac{q_i}{b^i \prod_{j=1}^{2}(i+j)} \langle z-a \rangle^{i+2} - d_1 z - F_t z + C_2 \tag{3.20}$$

where d_1 is the second summation term as shown in (3.19). The boundary condition used to obtain the integration constant C_2 in (3.20) is the bending moment at the needle tip ($z = L$). The boundary condition is known to be zero. Therefore $M(L) = 0$ and

$$\begin{aligned} -M(z) = &\sum_{i=0}^{m} \frac{q_i}{b^i \prod_{j=1}^{2}(i+j)} \langle z-a \rangle^{i+2} - d_1(z-L) \\ &\underbrace{- b^2 \sum_{i=0}^{m} \frac{q_i}{\prod_{j=1}^{2}(i+j)}}_{d_2} + F_t(L-z). \end{aligned} \tag{3.21}$$

The sign conventions in the above equations for the shear force $-V(z)$ and bending moment $-M(z)$ are according to Gere *et al.* [88, p. 463f]. Shear force $V(z)$ and bending moment $M(z)$ are negative in case of a positive deflection because the z axis is positive rightward and the y axis is positive downward. The angle θ is positive when clockwise.

Dividing (3.21) by EI and integrating once with respect to z gives the deflection slope $\theta(z)$ along the needle. The needle is clamped at its base, which means that $\frac{du}{dz}\big|_{z=0} = 0$. Hence, the boundary condition for $\theta(z)$ is $\theta(0) = 0$. Therefore,

$$\begin{aligned} \theta(z) &= \frac{du}{dz} \\ &= \frac{1}{EI}\left[\sum_{i=0}^{m} \frac{q_i}{b^i \prod_{j=1}^{3}(i+j)} \langle z-a \rangle^{i+3} - \frac{d_1}{2} z^2 - (d_2 - d_1 L) z + \frac{F_t z}{2}(2L - z)\right] \end{aligned} \tag{3.22}$$

where d_2 is the second term in (3.21).

By integrating (3.22), the beam deflection is obtained. The boundary condition for $u(z)$ is $u(0) = 0$. Therefore,

$$u(z) = \frac{1}{EI}\left[\sum_{i=0}^{m} \frac{q_i}{b^i \prod_{j=1}^{4}(i+j)} \langle z - a \rangle^{i+4} - \frac{d_1}{6} z^3 - \frac{1}{2}\left(d_2 - d_1 L\right) z^2 + \frac{F_t z^2}{6}(3L - z)\right] \tag{3.23}$$

where d_1 and d_2 are defined in (3.19) and (3.21), respectively. The following section uses the model introduced in this section to devise a method for estimating needle deflection in real time.

3.3.2 Real-Time Deflection Estimator

This section introduces a method to estimate the magnitudes of the loads, which are later used in (3.23) to find the needle deflection $u(z)$. In order to obtain $u(z)$ using (3.23), first the load parameters q_i and F_t need to be found. In the model, the parameters m, q_i and F_t define the shape and magnitudes of the loads applied to the needle. m is the polynomial order of the distributed load q_d along the inserted needle portion. Thus, m determines how many iterations of the load components shown in Figure 3.4 must be superimposed.

The question now arises which polynomial order and thus how many measurements are necessary to obtain an accurate needle deflection estimate. In other words, we need to determine how many load components must be superimposed according to (3.23) in order to accurately predict needle deflection. The following section addresses this question and gives an analysis with regards to different considered load shapes.

Identification of Load Shape

We want to estimate the needle deflection with only the two measurements force and torque at the needle base with an analytic approach. Here we show that this can be done with sufficient accuracy.

The procedure is divided into two steps: 1) minimization of a cost function involving the residual between estimated and measured shape of the needle shaft. Four measurements along the deflected needle shaft at the final insertion depth are used in a cost function, which takes the load parameters. In step 2), multiple iterations of this optimization algorithm while

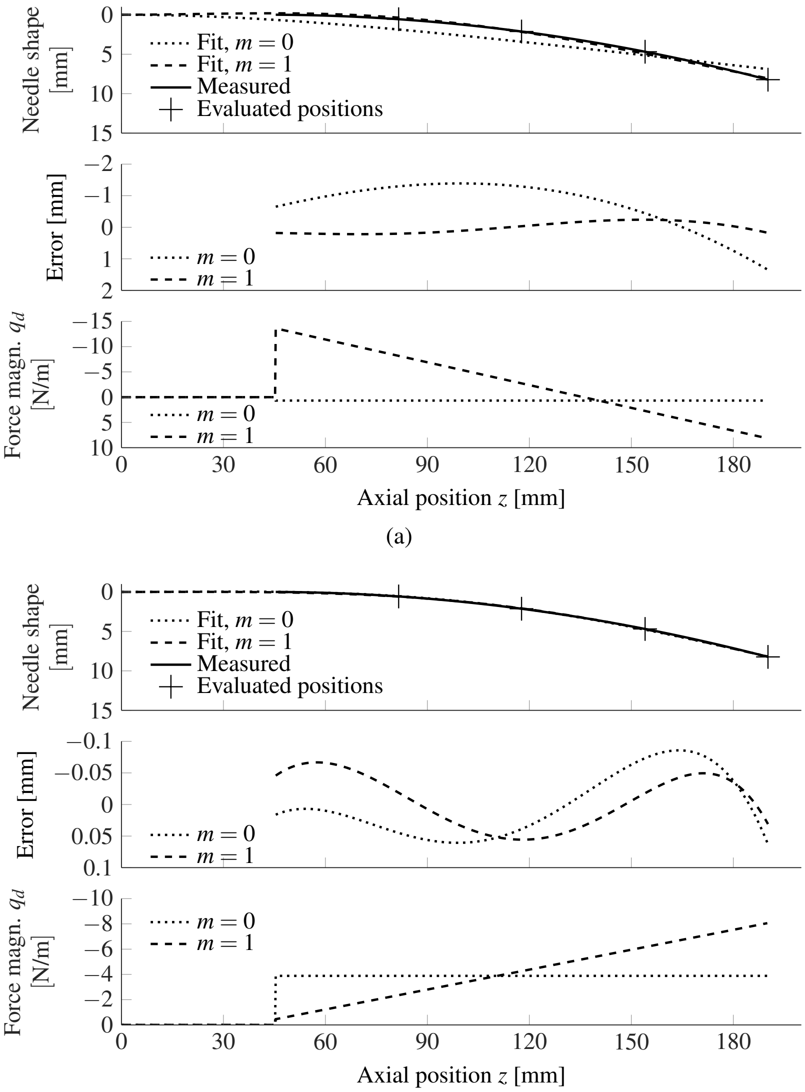

(a)

(b)

Figure 3.5: The optimization result with $m = 0$ and $m = 1$, insertion velocity 5 mm/s and Tissue 1. Optimization results (a) without considering F_t and (b) with considering F_t. The middle plots shows the error between measured and fitted shape. The identified load parameters shown in the bottom plot of (a) are $\mathbf{q} = [0.67]$ N/m for $m = 0$ and $\mathbf{q} = [-13.64 \quad 21.78]$ N/m for $m = 1$, and of (b) are $\mathbf{q} = [-3.88]$ N/m and $F_t = 0.33$ N for $m = 0$ and $\mathbf{q} = [-0.45 \quad -7.61]$ N/m and $F_t = 0.44$ N for $m = 1$.

incrementing m in each iteration are performed. A comparison of the mean absolute error (MAE) between the measured and estimated needle shaft shape for different m reveals the necessary minimum order for $q_d(z)$.

Table 3.2: The optimization performance for different values of m measured in MAE for insertion velocity 5 mm/s. σ is the standard deviation of the error between measurement and estimate.

m	Tissue 1 MAE [mm]	Tissue 1 σ [mm]	Tissue 2 MAE [mm]	Tissue 2 σ [mm]	Required load parameters
0	0.8733	0.8675	1.0741	1.2605	q_0, F_t
1	0.7923	0.4984	0.2897	0.3516	q_0, q_1, F_t
2	0.9372	0.3391	0.4371	0.1288	q_0, q_1, q_2, F_t
3	0.939	0.3327	0.391	0.1061	$q_0, ..., q_3$, F_t
4	0.9368	0.3341	0.3483	0.0953	$q_0, ..., q_4$, F_t

Step 1: A cost function is devised, which determines the residual R between estimated and measured needle shaft shape at the final insertion depth. Measured shape $u(\mathbf{z})$ with $\mathbf{z} = [82, 118, 154, 190]$ mm is acquired from the same experimental data as described in Section 3.3.3. The estimated shape $\hat{u}(\mathbf{z})$ is obtained from (3.23). R is minimized by optimizing the selection of the load parameters $\mathbf{q} = [q_0, q_1, ..., q_i, ..., q_m]$ and F_t. The cost function is

$$R(\hat{\mathbf{q}}, \hat{F}_t) = \left(\sum_{j=1}^{4} \left| \hat{u}(\mathbf{z}_j, \hat{\mathbf{q}}, \hat{F}_t) - u(\mathbf{z}_j) \right|^2 \right)^{1/2} \tag{3.24}$$

where $\hat{\mathbf{q}} = [\hat{q}_0, \hat{q}_1, ..., \hat{q}_i, ..., \hat{q}_m]$ is the vector of parameter estimates for the distributed load $q_d(z)$, $\hat{F}_t$ is the parameter estimate for the point load magnitude and j is the component index of $\mathbf{z}$.

To fit the measured shape to the estimated shape through optimizing $\hat{\mathbf{q}}$ and $\hat{F}_t$, R is minimized via MATLAB®'s *GlobalSearch* class with `fmincon` chosen as solver.

Step 2: To identify m, *Step 1* is carried out multiple times while m is incremented starting from zero in each iteration. Two different scenarios are considered. The first scenario includes the load F_t and in the second scenario, F_t is set to zero. We expect the distributed load q_d to change accordingly if F_t is omitted, to incorporate the needle tip's cutting force. The reason for considering the second scenario is that the amount of required load parameters is reduced by one while the needle-tissue interaction load modelling still closely resembles the physical needle-tissue interactions.

Figure 3.5 shows plots of two estimates ($m = 0$ & $m = 1$) versus the measured needle shaft shape at the final insertion depth b of 140 mm at an insertion velocity of 5 mm/s

Algorithm 3.1 Estimation of needle deflection

```
procedure DEFLECTION_ESTIMATOR
    Real-time loop for deflection u estimation during insertion:
    while $b <$ depth_final do
        $\mathbf{m} \leftarrow$ read_ftsensor()        ▷ Obtain the measurements for the current insertion step
        $\mathbf{q} = \mathbf{C}^{-1}\mathbf{m}$        ▷ Solve system of equations (3.25)
        u$\leftarrow \hat{u}(z, \mathbf{q})$        ▷ Use $\mathbf{q}$ in (3.23) to obtain $\hat{u}(z)$
    end while
end procedure
```

for Tissue 1 (see Section 3.3.3). In Figure 3.5a, F_t is omitted while in Figure 3.5b, F_t is included during parameter fitting. The plots illustrate the optimization performance for different values of m and the two considered scenarios. It can be observed that q_d adjusts accordingly when F_t is omitted.

Table 3.2 reports the error between the measured and estimated needle shaft shape expressed as MAE at insertion depth b =140 mm for insertion velocity 5 mm/s and two gelatin tissue samples (Tissue 1 and Tissue 2) with different stiffness (see Section 3.3.3). The data show that case $m = 1$ with omitted F_t and case $m = 0$ with considered F_t both show a small MAE $\ll$ 1 mm. Therefore, both of the above cases need to be considered for force/torque-based deflection estimation. It can also be concluded that only two measurements are necessary for obtaining an accurate needle shape and tip deflection estimate, which is helpful for the following section.

Deflection Estimation

To find the deflection estimate analytically, two measurements are assembled into a system of two equations. As measurements, we use the force and torque measured at the needle base by a force/torque sensor. The base force/torque measurements are the shear force and bending moment, respectively, at $z = 0$. Hence, for example, in order to obtain the two load parameters $\mathbf{q} = [\ q_0 \ \ q_1\ ]^T$, the following system of equations, consisting of (3.19) and (3.21) is solved for

$$\underbrace{\begin{bmatrix} q_0 \\ q_1 \end{bmatrix}}_{\mathbf{q}} = \mathbf{C}^{-1} \underbrace{\begin{bmatrix} V(0) = F_b \\ M(0) = M_b \end{bmatrix}}_{\mathbf{m}} \tag{3.25}$$

Figure 3.6: The ex-vivo tissue sample consisting of porcine loin muscle tissue embedded in gelatin.

with

$$\mathbf{C} = \begin{bmatrix} b & b/2 \\ b(-L+b/2) & b/2(-L+b/3) \end{bmatrix}$$

where $\mathbf{m} = [\ F_b \quad M_b\ ]^T$ is the vector of measurements. To obtain the deflection estimate $\hat{u}(z)$ at the current insertion depth b for $z \in (0, L)$, load parameters $\mathbf{q}$ obtained from (3.25) are inserted into (3.23). Then the deflection $u(z)$ expressed as a function of the measurements is

$$\hat{u}(z, \mathbf{q}) = \frac{1}{EI}\left[\sum_{i=0}^{1} \frac{\mathbf{q}_{i+1}}{b^i \prod_{j=1}^{4}(i+j)} \langle z - a\rangle^{i+4} - \frac{d_1}{6} z^3 - \frac{1}{2}\left(d_2 - d_1 L\right) z^2\right] \tag{3.26}$$

with $d_1 = b \sum_{i=0}^{1} \frac{\mathbf{q}_{i+1}}{i+1}$ and $d_2 = b^2 \sum_{i=0}^{1} \frac{\mathbf{q}_{i+1}}{\prod_{j=1}^{2}(i+j)}$. Algorithm 3.1 illustrates the procedure to obtain a real-time deflection estimate during needle insertion.

3.3.3 Experimental Validation

This section presents the experimental validation of the model-based quasi-static needle deflection estimation approach introduced in Section 3.3.1 and Section 3.3.2. Needle insertion experiments into phantom tissue made from gelatin (Knox®, NBTY Inc., Ronkonkoma, NY, USA) and porcine tissue are carried out with a standard hollow 18G (∅ 1.27 mm) brachytherapy needle (Eckert & Ziegler BEBIG Inc., Oxford, CT, USA), which has a length of 200 mm and is made from stainless steel. The effective needle length is, however, 190 mm due to the clamping at the needle's base. The insertion velocity is kept constant at 5 mm/s and the final insertion depth is 140 mm. The deflection measurements obtained from camera images of these insertions serve as the ground truth for model performance analysis.

Needles are inserted into two phantom tissue samples, Tissue 1 and Tissue 2, made with a gelatin to water ratio of 160 g/l and 194 g/l, respectively. This results in a significantly

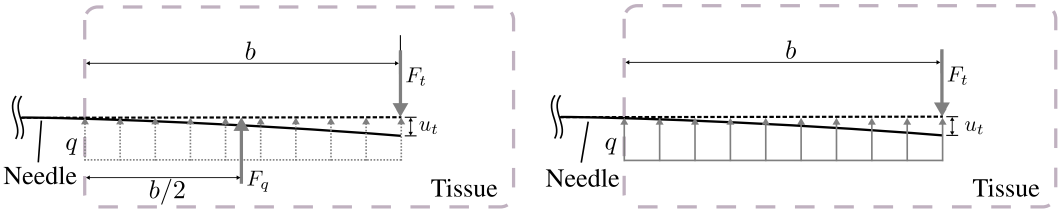

(a) Model 3 (b) Model 4

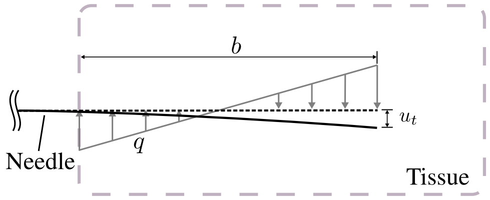

(c) Model 5

Figure 3.7: The model variants considered for performance analysis. (a) Model 3: Introduced in Section 3.2. The uniformly distributed load is reduced to the point load F_q. (b) Model 4: The uniformly distributed load is not reduced to a point load. (c) Model 5: A superposition of a uniform and triangular load ($m = 1$).

different tissue stiffness. The stiffness, estimated through indentation tests, is approximately 45 kPa for Tissue 1 and 60 kPa for Tissue 2. The values found for the two phantom tissues are similar to the properties of animal tissue [89]. Moreover, insertions into a sample of porcine loin muscle tissue, Tissue 3, are carried out. The porcine tissue sample is embedded into gelatin with a gelatin to water ratio of 150 g/l. A picture of the porcine tissue sample is given in Figure 3.6. Needles are inserted from the left hand side into the sample. Six insertion trials are performed into each of the three tissue samples with a new location chosen for each insertion. Thus in total, 18 insertions are carried out. Prior to the start of each trial, the needle is inserted 10 mm into phantom tissue and 15 mm into porcine tissue, respectively. This is done to ensure that the needle is visible in the initial US image.

The deflection estimation performance of two variants of the model introduced in this work and a comparable quasi-static model presented in Section 3.2, as shown in Figure 3.7, are compared in Figure 3.8 and Figure 3.9.

- Model 3 (see Figure 3.7a) models needle-tissue interactions as a uniformly distributed load along the inserted needle portion, which is reduced to a point load acting at the distributed load's centre of gravity, and a point load at the needle tip related to cutting force, as introduced in Section 3.2.

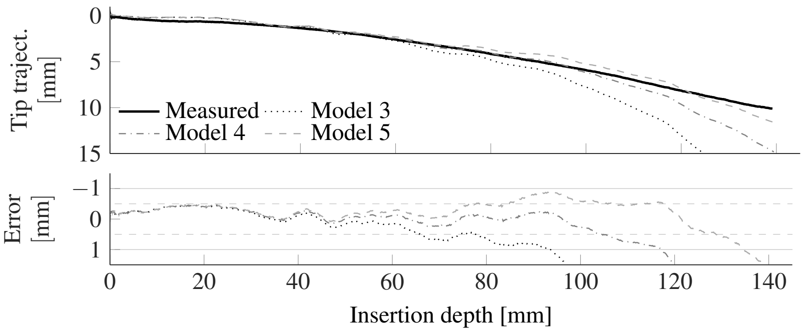

(a) Tissue 1

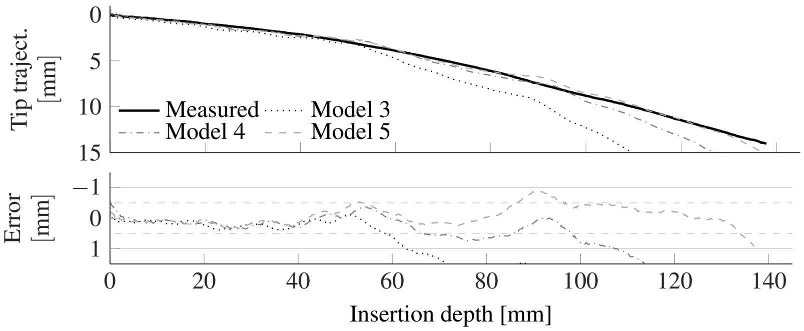

(b) Tissue 2

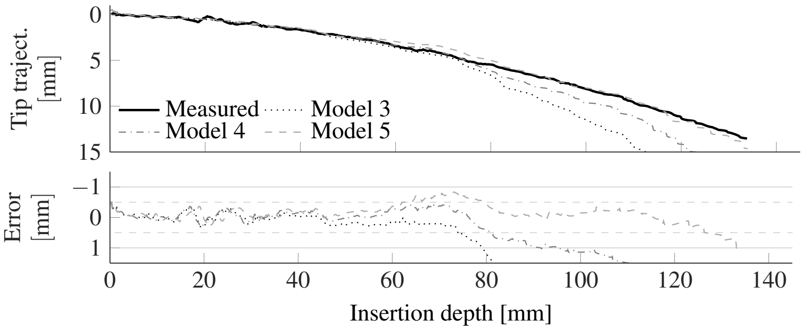

(c) Tissue 3

Figure 3.8: The average of six insertion trials is plotted for estimated and measured tip trajectory for three quasi-static model variants (Model 3, Model 4 and Model 5) for Tissue 1 (a), Tissue 2 (b) and Tissue 3 (c). The bottom plot contains the error between measured and estimated trajectory for all three models.

- Model 4 (see Figure 3.7b) is based on the methodology introduced in Section 3.3. Needle-tissue interactions are modelled as a uniformly distributed load ($m = 0$) and a point load at the needle tip.

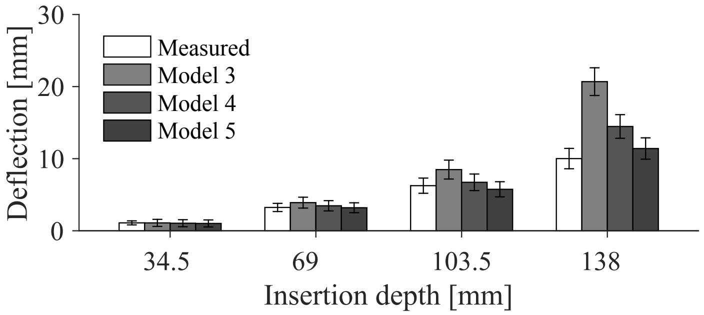

(a) Tissue 1

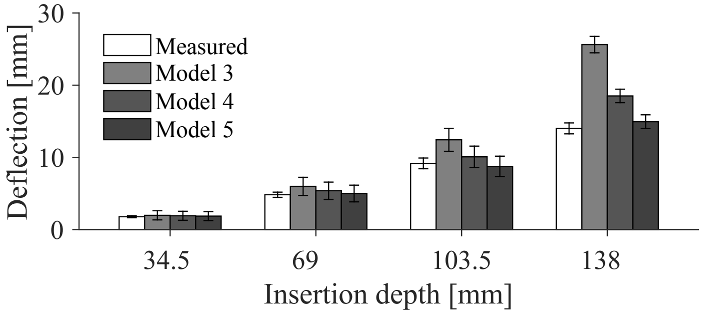

(b) Tissue 2

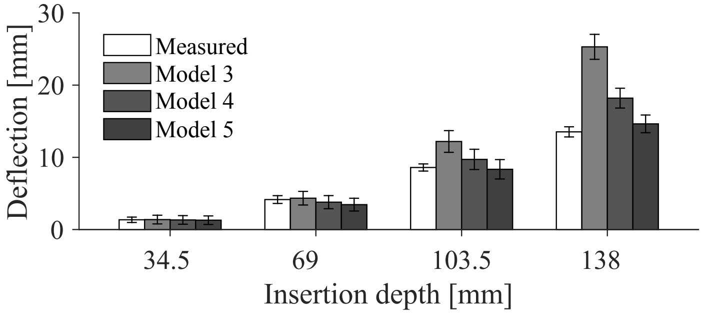

(c) Tissue 3

Figure 3.9: The average of six insertion trials is plotted for estimated and measured tip deflection for three quasi-static model variants (Model 3, Model 4 and Model 5) for Tissue 1 (a), Tissue 2 (b) and Tissue 3 (c) at discrete insertion depths. The error bars show the standard deviation σ.

- Model 5 (see Figure 3.7c) is also based on the methodology introduced in Section 3.3. It models the needle-tissue interactions as a triangularly distributed load with superimposed uniform load (first order, $m = 1$).

A comparison between measured and estimated needle tip trajectory for Tissue 1, Tissue 2 and Tissue 3 is given in Figure 3.8a, Figure 3.8b and Figure 3.8c, respectively. The average of the measured and estimated needle tip deflection for 6 trials is plotted along with the error between average estimated and measured tip deflections. Initially, up to a depth of approximately 50 mm, all models show a very similar performance as the estimation errors show only minor deviations among the models. At 50 mm depth, however, Model 3 starts to over-estimate tip deflection followed by Model 4 at approximately 100 mm depth. Model 5 maintains the best accuracy up to an insertion depth of approximately 130 mm as the estimation error remains below 1 mm.

Figure 3.9a, Figure 3.9b and Figure 3.9c show the average measured and estimated deflections for four discrete insertion depths across 6 trials for Tissue 1, Tissue 2 and Tissue 3, respectively as a bar chart. Each error bar depicts a standard deviation σ. It can again be observed that Model 5 performs the best especially at higher insertion depths and for all three tissues. The plotted error bars show overlapping standard deviations for Model 5 with the standard deviation of the measured tip deflection throughout insertion. The standard deviation for Model 3 and Model 4, however, do not overlap with the standard deviation of the measured deflection at a depth of 138 mm. This implies that the over-estimations of Model 3 and Model 4 are statistically significant while the slight over-estimation of Model 5 is not statistically significant. Table 3.3 presents the results of a two-sample t-test. The null hypothesis is that the mean of the measured deflection is equal to the mean of the estimated deflection over six trials. The variable r denotes that the null hypothesis must be rejected at the 5% significance level and $\bar{r}$ denotes that the null hypothesis can not be rejected. The results confirm the argument made based on Figure 3.9 that the over-estimation of Model 3 and Model 4 are statistically significant. Only for Model 5 can the null hypothesis not be rejected for all investigated insertion depths meaning that the mean difference between measured and estimated deflection is not statistically significant. As the error of Model 3 and Model 4 increases during insertion, the null hypothesis must be rejected at higher insertion depths meaning that the model inaccuracy is statistically significant.

Figure 3.10a, Figure 3.10b and Figure 3.10c show the needle shapes for Tissue 1, Tissue 2 and Tissue 3, respectively. For all three tissues, the deflection shape at a final insertion depth of 140 mm is plotted. As expected, based on the observation in Figure 3.8, the shape estimated by Model 5 follows the measured shape more closely than those estimated by Model 4.

Table 3.3: Results of a two-sample *t*-test.

Tissue #	Model #	Insertion depth [mm]			
		34.5	69	103.5	138
1	3	$\bar{r}$	$\bar{r}$	r	r
	4	$\bar{r}$	$\bar{r}$	$\bar{r}$	r
	5	$\bar{r}$	$\bar{r}$	$\bar{r}$	$\bar{r}$
2	3	$\bar{r}$	$\bar{r}$	r	r
	4	$\bar{r}$	$\bar{r}$	$\bar{r}$	r
	5	$\bar{r}$	$\bar{r}$	$\bar{r}$	$\bar{r}$
3	3	$\bar{r}$	$\bar{r}$	r	r
	4	$\bar{r}$	$\bar{r}$	$\bar{r}$	r
	5	$\bar{r}$	$\bar{r}$	$\bar{r}$	$\bar{r}$

r denotes that the null hypothesis must be rejected and $\bar{r}$ denotes that it can not be rejected at the 5% significance level.

Table 3.4: The mean absolute error between measured and estimated tip trajectory for all tissue samples and models in millimetres.

Tissue #	Mean absolute error [mm]		
	Model 3	Model 4	Model 5
1	1.90	0.68	0.40
2	2.30	0.79	0.26
3	2.23	0.84	0.26

3.3.4 Discussion

The needle tip deflection estimation results show that a more accurate needle tip deflection and needle shape estimation is in fact achieved with a first-order load distribution (proposed Model 3) as opposed to a zeroth-order distribution. As pointed out in Section 3.3.2, the accuracy of the deflection estimate does not increase significantly when an order higher than first is chosen for the load distribution, meaning that two distributed load parameters are enough to obtain an analytic estimation to $\hat{u}(z)$ with high accuracy (within a 1 mm margin of error). The results also show that it is possible to reduce the loads modelling needle-tissue interactions to only the distributed load while omitting the cutting induced point load F_t at the needle tip as a more precise estimate is obtained with Model 3 than Model 4. An inherent and obvious advantage of Model 5 is that the amount of necessary measurements can be reduced to one force and one torque at the needle base outside of tissue while maintaining a better accuracy up to a higher insertion depth. The comparison between the estimation performance of Model 3 in which the uniformly distributed load is reduced to a point load,

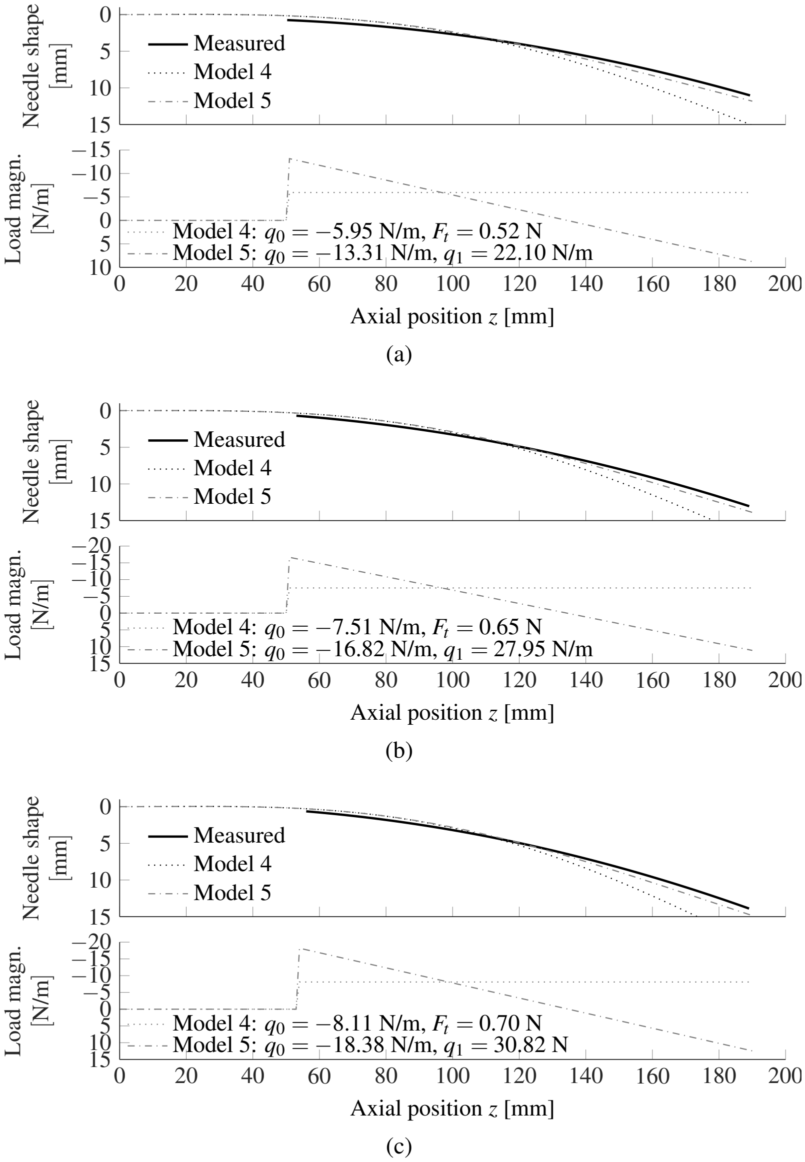

(a)

(b)

(c)

Figure 3.10: The measured and estimated needle shape at an insertion depth of 140 mm with estimates of Model 4 and Model 5 for (a) Tissue 1, (b) Tissue 2 and (c) Tissue 3. Insertion trial number three is plotted in the graphs for all tissue samples.

and models 4 and 5 shows that not reducing the distributed load to a point load results in better estimation performance.

By including biological tissue (Tissue 3) in the experimental validation of the deflection estimate, it is shown that the newly introduced needle-tissue interaction model not only shows good performance with homogeneous phantom tissue but also with ex-vivo, non-homogeneous, multi-layer tissue.

A novelty with respect to previously proposed models is that besides needle tip deflection, the entire needle shape (see Figure 3.10) is estimated. The plots in Figure 3.10 show that the estimated needle shape for Model 5 follows the measured needle shape inside tissue closely, which further indicates that the needle-tissue interaction loads considered in Model 5 are representative of the physical loads occurring along the inserted needle shaft.

Overall, the generalized quasi-static model for needle-tissue interaction newly proposed in this work also provides a framework for the identification of needle-tissue interactions as shown in Section 3.3.2. It proposes a general and adaptive pseudo-static model that is capable of modelling a variety of loads. Section 3.3.2 is only one example of applications for the proposed model.

The same limitation of Euler-Bernoulli beam theory brought forward in Section 3.2.2 also applies here. The issue is, however not as prevalent here as the maximum needle deflection at the final insertion depth ($\sim$14 mm) is within the acceptable amount of deflection. Another limitation of the experimental setup that is likely the cause for significant fluctuation in the deflection estimate is the relatively high dynamic range of the available force/torque sensor used to record the forces and moments at the needle base. The maximum forces and moments measured at the needle base are approximately 0.5% of the sensor's dynamic range.

3.3.5 Concluding Remarks

This chapter introduces an approach for sensing the needle deflection in real time during insertion into soft tissue. The only physical sensing device necessary is a force/torque sensor making it independent of explicit a priori characterization of tissue properties. In Section 3.2, the underlying needle-tissue interaction model and the resulting deflection model are derived and experimentally verified. It is shown that the newly introduced model (Model 3) achieves the best accuracy in estimating needle tip deflection compared to the other two tested models. In Model 3, a uniform load distribution ($q_{u,1}$, see Figure 3.2d) is assumed.

In Section 3.3, the investigation of the distributed load shape is further pursued. Moreover, the modelling approach is expanded to be more adaptive such that the deflection estimator's performance is improved during insertion into tissue having non-homogeneities and higher friction. The pseudo-static modelling framework for needle-tissue interactions presented here is applied to estimating the needle tip deflection and the needle shape during needle insertion. Experimental validation shows that the estimate obtained from the further improved method is more accurate than previously proposed needle-tissue interaction models of similar type (e.g., Model 3), in particular for greater insertion depths and for a multi-layer, non-homogeneous tissue sample.

Chapter 4

Needle Steering Using Force/torque-based Deflection Estimation

In this chapter, the best performing deflection estimator version introduced in Section 3.2 is used for needle tip trajectory prediction and control. Since the needle-tissue interaction loads assumed in Chapter 3 do not model the needle-tissue interactions after rotation, the bicycle model is applied to predict deflection after rotation. Therefore, this chapter proposes a method for predicting a needle tip trajectory with one axial needle rotation taking advantage of the force/torque-based deflection estimator in combination with a kinematic bicycle model. The trajectory prediction is then used to obtain an ideal rotation depth that brings the needle tip towards a pre-defined target.

The chapter is structured as follows. The kinematic bicycle model is first introduced and the fitting of the bicycle model parameters to the estimated needle tip trajectory then is described. The method for predicting the needle tip trajectory including one needle rotation using the kinematic bicycle model with the previously identified parameters is then presented (Section 4.1). Next, the approach for finding the optimal rotation depth is explained. Finally, results of insertion experiments with one rotation at the determined optimal rotation depth are presented in Section 4.2.

4.1 Needle Tip Trajectory Prediction

A flowchart depicting the individual steps involved in finding the best needle rotation depth for minimum targeting error is shown in Figure 4.1. Algorithm 4.1 further illustrates the procedure for finding the optimal rotation depth. The needle is first inserted in tissue without any axial needle rotation. The deflection estimator (I) takes as input the recorded force/torque data from this insertion and outputs an estimate of the tip trajectory. Parameter fitting (II)

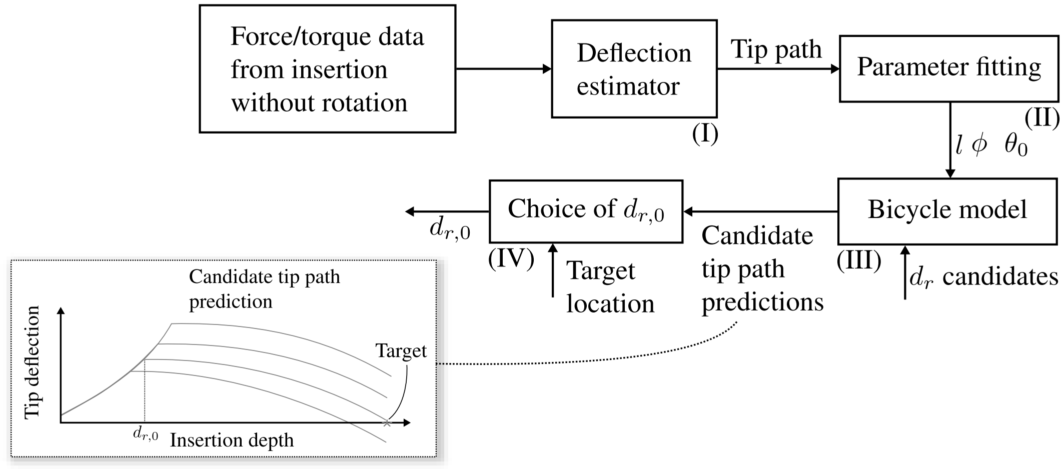

Figure 4.1: A flowchart depicting the method for finding the ideal rotation depth $d_{r,0}$ from candidate rotation depths d_r. (I) represents the deflection estimator proposed in Section 3.2, (II) identifies the bicycle model parameters wheel distance l, steering angle ϕ and initial angle of rotation θ_0 to the estimated tip trajectory obtained from (I), (III) creates candidate trajectories at different rotation depths d_r and (IV) chooses the rotation depth, which steers the tip towards the target.

is carried out to fit the parameters of the bicycle model to the estimated tip trajectory. The identified parameters are then supplied to the bicycle model (III), with which several candidate predicted trajectories are calculated for different rotation depths. Finally, we find the best rotation depth (IV), which leads to the least targeting error. The involved steps are introduced in the following sections.

Algorithm 4.1 The procedure for finding the optimal rotation depth $d_{r,0}$

```
$\hat{\mathbf{u}}_t \leftarrow$ DEFL_ESTIMATOR($\mathbf{F}_b$, $\mathbf{M}_b$)        ▷ $\hat{\mathbf{u}}_t$: Estimated needle tip trajectory vector
                                  ▷ $\mathbf{F}_b$, $\mathbf{M}_b$: Measured base force and moment vectors, respectively
[$l^*$, $\phi^*$, $\theta_0^*$] $\leftarrow$ LSQCURVEFIT(COSTFUNCTION, $\hat{\mathbf{u}}_t$)        ▷ $l^*$, $\phi^*$, $\theta_0^*$: Optimal bicycle parameters
$\mathbf{d}_r \leftarrow$ [0:2:$d_{r,ub}$] mm        ▷ $\mathbf{d}_r$: Vector of candidate rotation depths with a resolution of 2 mm
                                  ▷ $d_{r,ub}$: Upper rotation depth boundary
for $i$ from 1 to LENGTH($\mathbf{d}_r$) do
    $d_r \leftarrow \mathbf{d}_r[i]$
    $\mathbf{u}_{t,f}[i] \leftarrow$ BICYCLE($l^*$, $\phi^*$, $\theta_0^*$, $d_r$)        ▷ $\mathbf{u}_{t,f}$: Vector of needle tip deflections at target depth
end for
$i_{min} \leftarrow$ FIND_INDEX(ABSMIN($\mathbf{u}_{t,f}$))
$d_{r,0} \leftarrow \mathbf{d}_r[i_{min}]$

function COSTFUNCTION($l$, $\phi$, $\theta_0$, $d_r$)
    $\hat{\mathbf{u}}_{t,b} \leftarrow$ BICYCLE($l$, $\phi$, $\theta_0$, $d_r$)        ▷ $\hat{\mathbf{u}}_{t,b}$: Needle tip trajectory estimated by bicycle model
    return $\hat{\mathbf{u}}_{t,b}$
end function
```

4.1.1 Kinematic Bicycle Model

To find an optimal rotation point such that the needle tip reaches a desired target location, a model for predicting the trajectory that the needle tip will follow is needed. In related work, commonly a kinematic model of a bicycle is used, which was first introduced and adapted for the purpose of modelling multi-bend needle tip trajectories by Park *et al.* [41] and Webster *et al.* [37]. Since then, the kinematic bicycle model has become the most commonly used method for needle trajectory planning.

A schematic of the bicycle model is shown in Figure 4.2. The kinematic equation for a bicycle model in Euclidean space is [90]

$$\begin{bmatrix} \dot{z} \\ \dot{y} \\ \dot{\theta} \\ \dot{\phi} \end{bmatrix} = \begin{bmatrix} \cos\theta \\ \sin\theta \\ \tan\phi/l \\ 0 \end{bmatrix} v + \begin{bmatrix} 0 \\ 0 \\ 0 \\ 1 \end{bmatrix} \omega \tag{4.1}$$

where v is the bicycle's translational velocity and hence the needle insertion velocity, ϕ is the front wheel's steering angle and ω is the angular velocity of the front wheel's steering angle and therefore $\dot{\phi} = \omega$. θ is the angle between the horizontal axis and the bicycle. z is the horizontal and y the vertical position of the bicycle back wheel and thus the position of the needle tip. To relate the needle tip trajectory to the bicycle model's planar trajectory, the centre of the rear wheel is attached to the needle tip. To model needle rotation about 180°, the sign of the bicycle's front wheel angle ϕ is inverted. Furthermore, at the rotation depth, the bicycle angle θ is set to zero, which sets the bicycle parallel to the horizontal axis. This causes the bicycle model to account for the instant change in direction of the needle tip trajectory at the rotation depth.

4.1.2 Parameter Fitting

Now, we need to identify the constant parameters ϕ, l and θ_0 as shown in Figure 4.1, step (III) with a needle tip trajectory estimate obtained from the deflection estimator. θ_0 is the initial angle θ when insertion starts. Insertion data without needle rotation is considered for parameter identification. As (4.1) contains nonlinearities, the MATLAB® func-

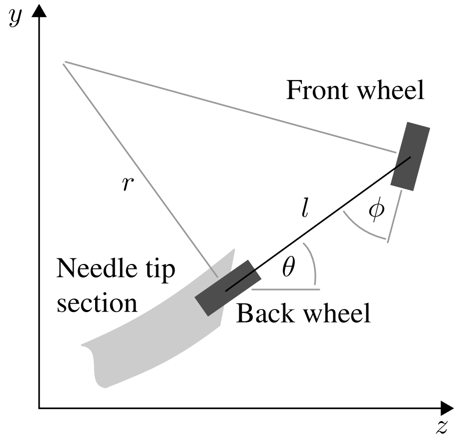

Figure 4.2: A schematic representation of the kinematic bicycle model. ϕ is the front wheel's steering angle, l is the length of the bicycle measured from the front wheel's centre to the back wheel's centre, and r is the radius of the circular trajectory of the bicycle's back wheel. θ is the angle of rotation between the horizontal coordinate and the bicycle. The centre of the bicycle's back wheel is attached to the needle tip.

tion `lsqcurvefit`, which implements a nonlinear least squares solver, is used. The `lsqcurvefit` solver, as shown in Algorithm 4.1, line 3, minimizes the distance between $\hat{\mathbf{u}}_{t,b}$ and $\hat{\mathbf{u}}_t$ in a least squares sense by adjusting the bicycle parameters l, ϕ and θ_0. The results of the parameter identification for two different phantom tissue samples are presented in Section 4.2.

4.1.3 Optimal Rotation Depth

Once we have identified the model parameters, the bicycle model is used with the previously identified parameters for the particular phantom tissue sample to find the rotation depth d_r at which the needle needs to be rotated such that the needle tip reaches a desired target at the final insertion depth. Furthermore, after the point of rotation, θ is re-set to zero. Preliminary experiments showed that this results in the best trajectory prediction after rotation.

Multiple different candidate tip trajectories are constructed using the bicycle model with one rotation at different depths. The final position of the needle tip is different for each candidate trajectory. The optimal rotation depth is now chosen by finding the candidate trajectory, which shows the smallest absolute distance between desired and actual tip location at the final insertion depth. This is done by iteratively searching for the smallest absolute distance between desired and actual tip location at the target depth (see Algorithm 4.1, line 10).

To verify the accuracy of the chosen optimal rotation depth, insertions in phantom tissue are carried out with one axial needle rotation by 180° at the optimal rotation depth with the experimental setup presented in Chapter 2. The good match between measured and predicted tip trajectories shows the successful performance of the trajectory prediction.

4.2 Experimental Results

In order to collect data for the identification of the bicycle parameters and for the validation of deflection estimates, insertion experiments are performed using two phantom tissue samples made from agar of type *A360-500* (Fisher Scientific International Inc., Hampton, NH, USA). The agar to water ratio for Tissue 1 is 8.3 grams per litre (g/l) and for Tissue 2 is 13.33 g/l. The used needle type is a standard 18-gauge prostate seeding needle of length 200 mm (Eckert & Ziegler BEBIG, Inc. Oxford, CT, USA).

Two types of insertion are carried out in each tissue sample: one without needle rotation and one with needle rotation by 180° at the optimal rotation depth calculated by the proposed method. The velocity of all insertions is kept constant at 5 mm/s. Six insertions are carried out without rotation to a final depth of 107 mm and three insertions are carried out with rotation at the optimal rotation depth to a final depth of 160 mm.

The estimated needle tip trajectory using the force/torque sensor approach, along with the measured needle tip deflection in camera images, and the bicycle model fit to the estimated tip trajectory are shown in the top panel of Figure 4.3. The estimated tip trajectory via the force/torque sensor is smoothed with a Savitzky-Golay filter prior to parameter fitting. The maximum error between the bicycle model trajectory and the measured tip trajectory is

Table 4.1: The bicycle model parameter identification and rotation depth prediction results. The mean is taken over six trials. σ is the standard deviation.

Tissue #	l [mm]		ϕ [rad]		θ_0 [rad]		$d_{r,0}$ [mm]
	Mean	σ	Mean	σ	Mean	σ	
1	33.33	11.94	0.03	0.003	0.04	0.02	63
2	27.36	7.37	0.03	0.009	0.09	0.02	55

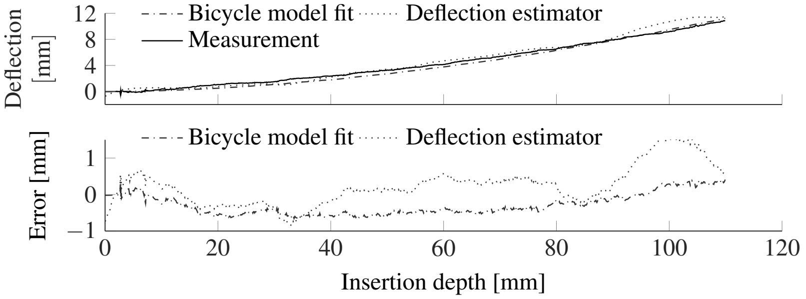

(a) Tissue 1, insertion 1

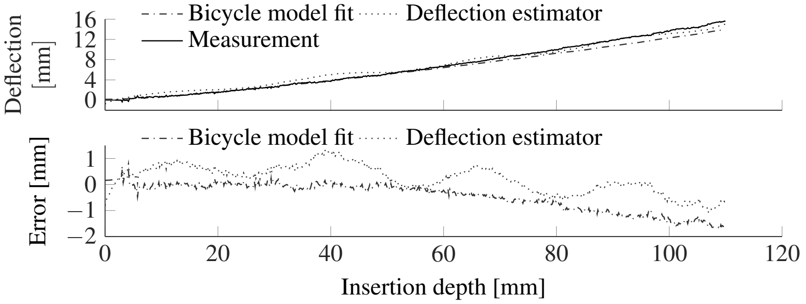

(b) Tissue 2, insertion 1

Figure 4.3: The bicycle model fit to the estimated tip trajectory (top plots). The bottom plots show the error between bicycle model trajectory and measured tip trajectory, and the error between deflection estimator and measured tip trajectory.

1.5 mm. The results of the bicycle parameter identification are shown in Table 4.1 along with the resulting estimate for the optimal rotation depth $d_{r,0}$. Figure 4.4 shows the measured tip trajectories for six insertions and both tissue samples, and the bicycle model trajectory resulting from the parameters listed in Table 4.1. The fact that the bicycle trajectory is in close proximity to the measured tip trajectories further demonstrates the quality of the parameter estimate.

Table 4.2: The bicycle model prediction results for insertions with rotation at the identified $d_{r,0}$. MAE is the Mean Average Error and σ is the standard deviation. Accuracy is the accuracy with which the needle tip reached the target location.

Tissue	Run	Before rotation		After rotation		Accuracy [mm]
		MAE	σ	MAE	σ	
1	1	0.38	0.18	0.63	0.6	-1.05
	2	0.18	0.11	0.40	0.47	-1.30
	3	0.32	0.12	1.13	0.55	-2.26
2	1	0.69	0.31	0.69	0.16	0.6
	2	1.01	0.36	1.01	0.17	1.33
	3	0.84	0.37	0.73	0.2	0.57

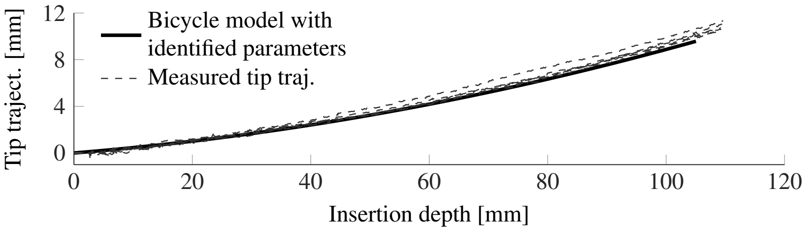

(a) Tissue 1

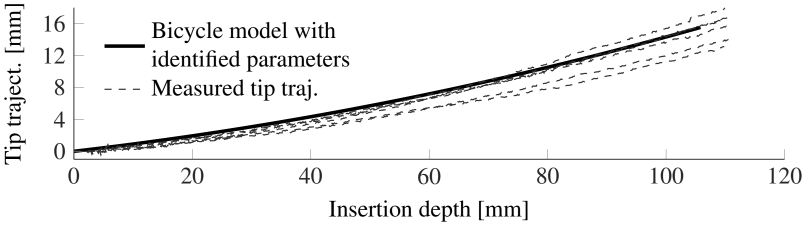

(b) Tissue 2

Figure 4.4: Measured tip trajectories of six insertions for each tissue and the bicycle model trajectory obtained from the parameter fit.

To find $d_{r,0}$, i.e. 63 mm and 53 mm, the mean values for ϕ, l and θ_0 presented in Table 4.1 are used. The needle is then re-inserted in tissue and rotated at the found rotation depths to validate the prediction performance. Results are shown in Figure 4.5. The error between measured and predicted trajectory does not exceed 1 mm throughout insertion. Table 4.2 gives a statistical evaluation of the tip trajectory prediction performance with insertions including one axial rotation. The mean absolute error (MAE) is separately evaluated for the trajectory before and after the depth of rotation in order to show that the needle tip trajectory after rotation can be approximated with the identified bicycle parameters with a good accuracy. The maximum MAE for Tissue 1 before rotation is 0.38 mm. After rotation, the maximum MAE increases to 1.13 mm. For Tissue 2, the maximum MAE is 1.01 mm before rotation and 1.01 mm after rotation. The targeting accuracy is better for Tissue 2 as only Run 2 shows a higher error than 1 mm whereas all insertion runs for Tissue 1 show an accuracy slightly lower than 1 mm. Overall, the average accuracy is -1.54 mm for Tissue 1 and 0.83 mm for Tissue 2, with an absolute average error of 1.19 mm across both tissues.

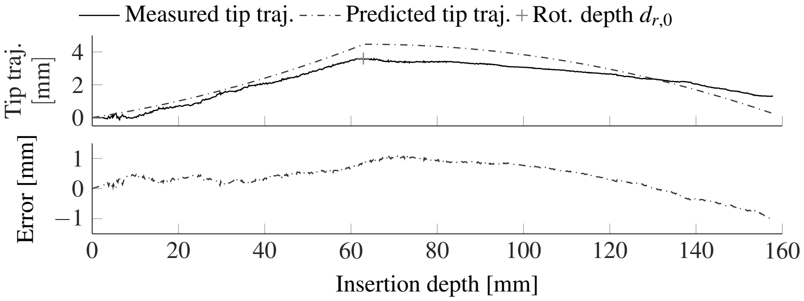

(a) Tissue 1, insertion 1

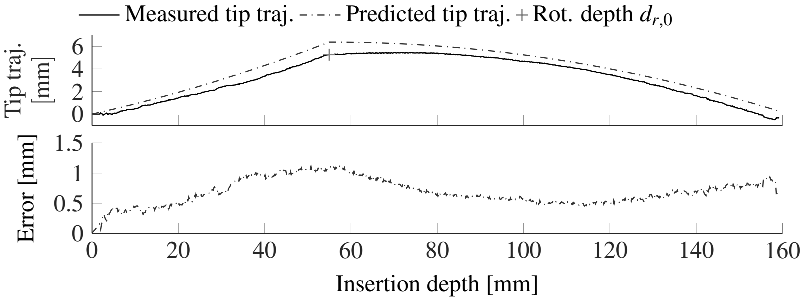

(b) Tissue 2, insertion 1

Figure 4.5: The predicted (bicycle model) and measured tip trajectory (top plot) with one rotation, and the error between measured and predicted tip trajectory (bottom plot) for insertions into both tissues.

4.3 Discussion

It is stated in Section 4.2 that only insertions up to a depth of 107 mm are considered for parameter identification. This is due to a loss of the defection estimator's accuracy beyond an insertion depth of approximately 110 mm. The experimental results, however, show that the limited insertion depth consideration for parameter identification is not an issue as it is still possible to obtain a parameter fit with good accuracy. Furthermore, the standard deviation σ in Table 4.1 for parameter l is fairly high. This is likely due to a variation in the tip trajectory among insertions as Figure 4.4 shows. Another likely reason is the noise in the force/torque sensor's signal causing variation in the deflection estimate.

It is shown in Section 4.2 that the predicted tip trajectory follows the measured tip trajectory closely according to a maximum MAE of 1.13 mm after the rotation depth across both tissues and insertions. The error occurring in the trajectory before the depth of rotation can be attributed to the fact that the tip trajectory estimate contains some remaining imprecision. Furthermore, Figure 4.4 shows variation in the observed needle tip trajectories among insertions. This variation would also appear in insertions with rotation.

4.4 Concluding Remarks

In this work, a method for needle trajectory prediction and control is proposed without the need for image feedback. The method consists of a force-sensor-based deflection estimator, which is used to parameterize a kinematic bicycle model for the prediction and control of the needle tip trajectory towards a desired target. It is experimentally validated that the introduced methodology can predict the necessary rotation depth to steer the needle tip towards a pre-defined target and that the target is reached within an absolute average error of 1.19 mm, which is an improvement compared to the current achievable clinical accuracy.

Chapter 5

Needle Steering Using Lateral Actuation and Axial Rotation

5.1 Introduction

During prostate brachytherapy, the needle deflection needs to be controlled by an experienced surgeon such that the deflected needle shape at the final insertion depth is as close to the unbent needle as possible through the choice of an appropriate insertion depth at which the intermittent axial rotation is carried out (rotation depth). A further needle steering input used manually by surgeons is the application of lateral force onto the needle. The force is applied near the needle's entry point in tissue against the direction of deflection using the finger early on during insertion. The lateral force enacted by the finger results in lateral needle displacement against the direction of deflection caused by the bevelled needle tip. Lateral needle actuation allows for direct manipulation of needle deflection inside tissue and can be used to counter the deflection caused by the bevelled needle tip and therefore bring the needle to a desired trajectory. It also increases the configuration space and dexterity of the needle tip to essentially relax the constraint to travel along the path cut by the needle tip. These two advantages have direct applications in prostate brachytherapy where the added dexterity can help to steer the needle towards the desired straight path. Naturally, the bevelled tip of the needle is constrained to move on a circular trajectory during insertion. This constraint can be significantly relaxed through lateral force as the needle tip can now be directly moved laterally thus increasing the needle tip's dexterity. The lateral force is a continuous input to a deflection control algorithm meaning that the deflection can also be influenced in a more continuous manner as opposed to intermittent axial rotation. If the goal is to keep the needle tip on a straight line (as it is assumed in seed deposition planning during prostate brachytherapy), the axial rotation input needs to be invoked continually to keep the tip deflection under a threshold. This is physically understandable due to the effect of the bevelled tip, since as long as the needle insertion velocity is non-zero, its trajectory will diverge from a straight line. Since excessive use of axial rotation results in tissue drilling effects [68], the availability of an additional control input (the lateral force) that can reduce the amount of necessary axial needle rotations is highly beneficial.

While in the past intermittent or continuous axial needle rotation has been the primary steering action [17, 37, 91, 40], the second above-mentioned steering action being the lateral application of force somewhere on the needle (near the needle entry point into tissue) has not been considered extensively for robotic needle steering. Robotic systems have been developed, specifically for prostate brachytherapy, that provide actuated guides that either complement or replace the fixed grid template (see Figure 1.1) for needle guidance and deflection manipulation during insertion [55, 77, 81, 92, 79]. However, to the best of the author's knowledge, none of these systems use the proposed arrangement of a fixed and actuated needle guide (see Section 2.2) specifically for needle steering.

Furthermore, as the methods developed particularly in the second part of this thesis are aimed towards assisting the surgeon during needle insertion without the need for excessive changes to the work flow of the prostate brachytherapy procedure, surgeon-in-the-loop robotic assistance is introduced in this chapter and compared to other available automation levels. The needle steering concepts and robotic systems for needle steering available in the literature can be divided into the three automation levels fully automated steering, semi-automated steering (surgeon-in-the-loop) and assisted manual steering (enhancing the surgeon's awareness through haptic cues, etc.) as introduced in Section 1.2. Each of these automation levels has various advantages and disadvantages, which will be further elaborated on in Section 5.2.

In this chapter, an initial analysis of the effect of lateral actuation on reducing needle deflection is provided while also introducing a collaborative approach between human and machine that provides robotic assistance for steering actions. The advantages of using steering inputs axial rotation and lateral actuation simultaneously for minimizing both the needle tip deflection and achieving an unbent needle shaft at the final insertion depth are presented. A combination of the two steering actions that are currently carried out manually during brachytherapy are performed automatically by a robotic assistance system while the needle is inserted fully manually by the surgeon such that the surgeon is in charge of the most safety-critical tasks during the needle insertion procedure. Thus, this system represents a

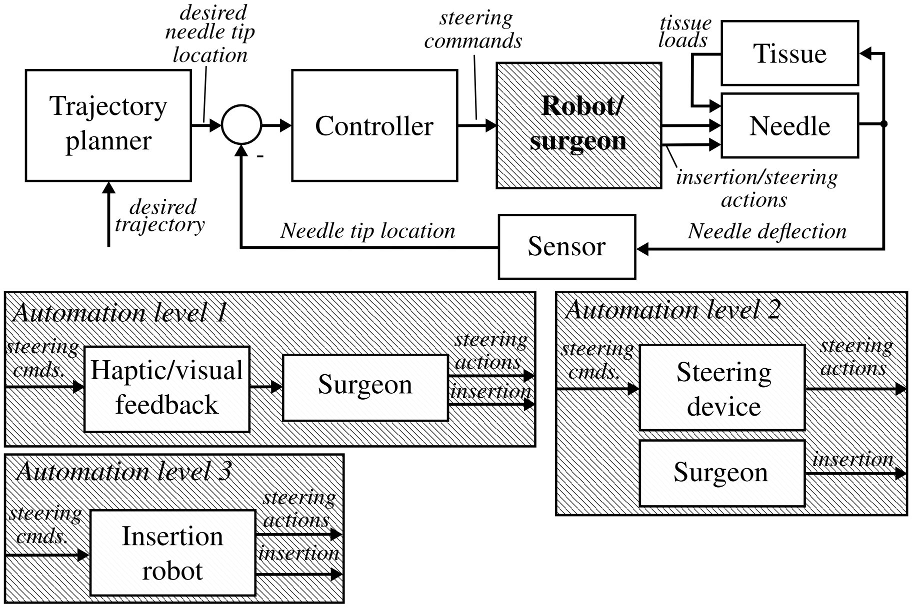

Figure 5.1: The three automation levels for robotics-assisted needle steering.

human-in-the-loop collaborative robotic assistant system. With this assignment of responsibilities, the steering accuracy of fully automated insertion is retained while the procedure's safety remains guaranteed by keeping the surgeon in the loop. Particularly the requirement of an unbent needle at the final insertion depth is important during prostate brachytherapy to ensure seed placement along a straight line. When, however, axial rotations alone are used to steer the needle and the number of rotations needs to be limited in order to avoid tissue trauma [68], this objective is difficult to achieve.

5.2 Semi-automatic Needle Insertion

Figure 5.1 shows the concept of needle steering as a block diagram. A needle steering system consists of the needle-tissue system where the needle deflects as it is inserted into tissue. The needle tip location can be tracked using medical imaging modalities for feedback control of the needle deflection. A trajectory planner determines the desired needle tip location based on a desired trajectory and a controller minimizes the error between desired and measured needle tip location through supplying appropriate steering commands to either the robotic system or surgeon, depending on the automation level.

The allocation of actions to either a machine or the surgeon is classified into three categories, namely automation levels 3, 2 and 1. For a system of the type automation level 3, an autonomous robotic system is in complete control of the insertion and carrying out the steering actions commanded by the controller. In this automation level, human involvement is entirely eliminated from the needle insertion procedure. A major challenge with automation level 3 is, however, to guarantee the stability and safety of the robotic system, which is difficult in an uncertain environment such as the human body. This causes issues with clinical acceptance, which makes clinical implementation of systems with automation level 3 difficult.

To help mitigate these issues, automation levels 1 or 2 can be considered where the surgeon remains in charge of safety-critical tasks such as the insertion itself or steering actions, depending on the automation level. Considering a system of automation level 2, the controller provides steering commands to a device that automatically carries out commanded steering actions while the surgeon remains in charge of needle insertion. This scenario is commonly referred to as surgeon-in-the-loop. Finally, automation level 1 represents the least automated level where only visual or haptic information, guidance and suggestions are provided to the surgeon based on the controller output. The final decision as to whether the action is carried out remains solely with the surgeon, which makes automation level 1 the safest. When considering the example of needle insertion, however, executing both steering actions simultaneously and manually while also inserting the needle, as would be the case in automation level 1 can be overwhelming for the human, which leads to sub-optimal performance and inaccurate needle steering. Therefore in this work, the robotic assistant system controls the steering actions while the surgeon remains in charge of needle insertion in accordance with automation level 2. The hypothesis is that the lateral force can help with this goal while the amount of necessary needle rotations can be limited to only one in order to minimize tissue trauma.

To show that using both steering inputs simultaneously helps reduce the needle bending at the final insertion depth, insertion experiments are carried out where a constant lateral force is applied during a section of the insertion. During the same insertion, one rotation is carried out at a depth that minimizes the needle tip deflection at the final insertion depth. Two more scenarios are considered where only one of the steering inputs is used in each scenario. The three scenarios and parameter settings of the steering inputs are listed in Table 5.1.

5.3 Simulation of Lateral Actuation

Before carrying out the experimental study, a simple needle deflection model based on Euler-Bernoulli beam theory is introduced in this section for the simulation of the needle's deflection when a lateral point load is applied. The purpose of this simulation study is to illustrate the needle's displacement and shape when applying the lateral force at varying insertion depths. Of particular interest is how the insertion depth impacts the needle displacement, especially the deflection slope at the needle tip. From this information, conclusions concerning the insertion depth at which the lateral force should be applied in order to achieve the maximum reduction in needle deflection at the final insertion depth can be drawn. Figure 5.2a shows the modelled forces and moments acting on the needle as it is displaced by the lateral point load F_l. q_t is the reaction load enacted by tissue onto the needle caused by the displacement. For the sake of simplicity, q_t is assumed to be uniform. F_R and M_R are the reaction force and moment, respectively, enacted by the fixed needle guide that is modelled as a clamping.

The clamped needle-tissue system shown in Figure 5.2a can be expressed as

$$EI\frac{d^4u(z)}{dz^4} = F_l\langle z - c_2\rangle^{-1} - q_t\langle z - c\rangle^0 \tag{5.1}$$

where $u(z)$ is the needle deflection, c_2 is the distance between the fixed to the actuated needle guide and $c = c_1 + c_2$ is the distance between the fixed needle guide and the tissue. The loads F_l and q_t in (5.1) are modelled by the following discontinuous function [88]

$$\langle z - c\rangle^n = \begin{cases} 0 & \text{when } z \leq c \\ (z-c)^n & \text{when } z > c \end{cases} \quad \text{if } n = 0, 1, 2, ... \qquad \begin{cases} +\infty & \text{when } z = c \\ 0 & \text{when } z \neq c \end{cases} \quad \text{if } n = -1.$$

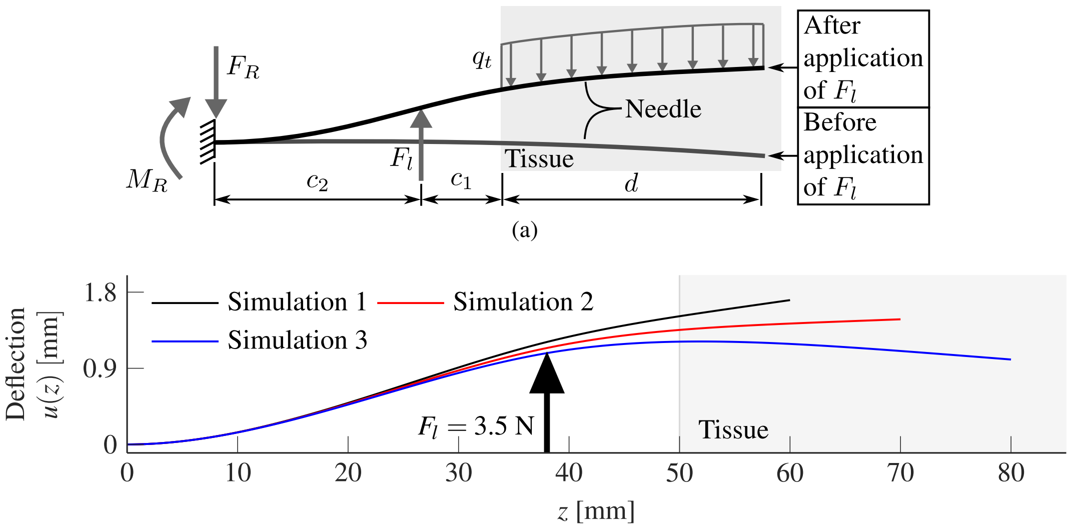

(a)

(b)

Figure 5.2: (a) A schematic representation of the clamped needle inserted into tissue with a lateral point load F_l applied at $z = c_2$ and the reactions due to needle clamping (F_R and M_R), and tissue displacement q_t. (b) Simulation results considering the three simulated needle insertion depths 10, 20 and 30 mm.

To solve for the needle deflection $u(z)$, (5.1) needs to be integrated four times. The first integration of (5.1) yields the shear force $V(z)$

$$V(z) = F_l \left(1 - \langle z - c_2 \rangle^0\right) + q_t \left((l - c) - \langle z - c \rangle^1\right) \tag{5.2}$$

when using the known boundary condition at the needle tip $V(l) = 0$ to solve for the constant of integration. Integrating (5.2) yields the bending moment $M(z)$

$$M(z) = F_l \left[(z - c_2) - \langle z - c_2 \rangle^1\right] + q_t \left[(l - c)z - \frac{\langle z - c \rangle^2}{2} + \frac{c^2 - l^2}{2}\right] \tag{5.3}$$

when using the known boundary condition at the needle tip $M(l) = 0$ to solve for the constant of integration. Integrating (5.3) twice more yields the needle deflection $u(z)$

$$\begin{aligned} u(z) = \frac{1}{24EI} \Bigg[& F_l \left(4z^3 - 4\langle z - c_2 \rangle^3 - \frac{c_2}{2} z^2\right) \\ & - q_t \left(\langle z - c \rangle^4 - 6(l - c)z^3 - 6\left(c^2 - l^2\right) z^2\right)\Bigg] \end{aligned} \tag{5.4}$$

when using the known boundary conditions at $z = 0$ where $u'(0) = 0$ and $u(0) = 0$ to solve for the constants of integration.

The next step is to find a linear system of three equations to solve for the unknowns F_R, M_R and q_t. For the first equation, (5.2) can be used in combination with the boundary condition $V(0) = F_R$:

$$V(0) = F_R = -q_t(l - c) - F_l \rightarrow F_l = -F_R - q_t(l - c) \tag{5.5}$$

and for the second equation, (5.3) can be used in combination with the boundary condition $M(0) = -M_R$:

$$M(0) = -M_R = -F_l c_2 + \frac{q_t\left(c^2 - l^2\right)}{2} \rightarrow F_l = \frac{M_R}{c_2} - \frac{q_t\left(c^2 - l^2\right)}{2} \tag{5.6}$$

A third equation can be established as follows:

$$M(c) = -F_R c - M_R + q_t \frac{d^2}{2} + F_l c_1 = 0 \rightarrow F_l = \frac{F_R c}{c_1} + \frac{M_R}{c_1} - q_t \frac{d^2}{2c_1} \tag{5.7}$$

when considering that equilibrium must be maintained. The linear system of equations is then

$$\begin{bmatrix} -1 & 0 & -(l-c) \\ 0 & \frac{1}{c_2} & -\frac{c^2-l^2}{2} \\ \frac{c}{c_1} & \frac{1}{c_1} & -\frac{d^2}{2c_1} \end{bmatrix} \begin{bmatrix} F_R \\ M_R \\ q_t \end{bmatrix} = F_l \mathbf{1}_{3\times 1} \tag{5.8}$$

Simulation results for the three insertion depths 10, 20 and 30 mm are plotted in Figure 5.2b. The plots show that the orientation of the needle tip and therefore its heading can be directly manipulated by using lateral force where the insertion depth at which the force is applied influences the amount of achievable tip orientation change. For each insertion depth, the needle tip heading and deflection differ such that at shallower depth (e.g., Simulation 1), the change in needle tip heading is much higher.

Supposing that the needle is further inserted beyond the depths shown in Figure 5.2b while the lateral force F_l is still applied, the most reduction of needle deflection could presumably be achieved with force application according to Simulation 1. This simulated behaviour of the needle makes physical sense due to a combination of the needle's decreased resistance to bending and a greater amount of the needle being embedded in tissue with increased length. Moreover, the needle shapes plotted in Figure 5.2 show a similar needle tip deflection compared with the experimental measurements of the needle tip deflection plotted in Figure 5.5b and Figure 5.6b at equivalent insertion depths. This indicates that the deflection model represents the physical behaviour of the needle when applying the lateral force F_l. The conclusion from this simulation is thus that lateral force needs to be applied early to maximize its effect with respect to reduction of deflection.

5.4 Experimental Study

5.4.1 Protocol

To evaluate the ability to minimize needle deflection for various combinations of the two needle steering inputs lateral actuation and axial rotation, three scenarios are considered. The scenarios are listed in Table 5.1 where in the first two scenarios, only one of the steering inputs is considered while in scenario 3, both inputs are used simultaneously. In each scenario, a standard 18 gauge brachytherapy needle (Type RP-1100-1820, Riverpoint Medical, Portland, OR, USA) is inserted manually into a phantom tissue sample made from Plastisol (Type Super Soft Plastic, M-F Manufacturing Co., Inc, Fort Worth, TX, USA) and an ex-vivo porcine loin tissue sample using the Hand-held Needle Steering Assistant described in Section 2.2 and [35]. The final insertion depth d_f is 140 mm. The stiffness of the phantom tissue sample was adjusted to 11 kPa using a ratio of 1/4 plastic softener to Plastisol.

The optimal values of the steering action parameters rotation depth d_r, and lateral force profile F_l were determined empirically during preliminary experiments informed by the sim-

Table 5.1: The three considered experimental scenarios. Rotation and lateral actuation are done by machine, insertion manually.

Scenario	Rotation	Lateral actuation	Rotation depth [mm]	Applied force(s) [N]
1	yes	no	35	n/a
2	no	yes	n/a	-[2, 2.5, 3, 3.5]
3	yes	yes	50	-3.5

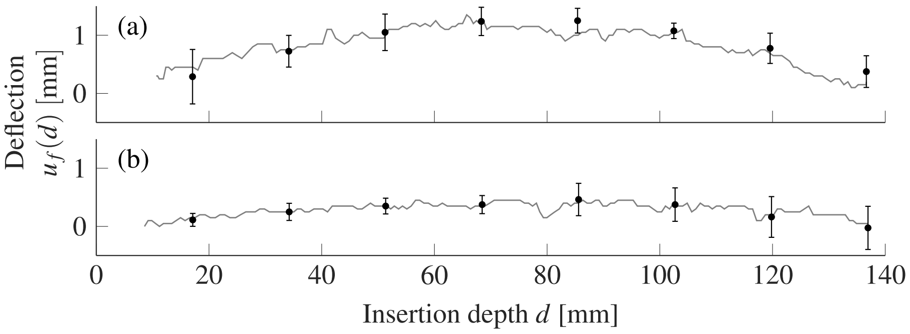

Figure 5.3: The needle deflection at the final insertion depth $u_f(d)$ for one insertion during (a) scenario 1 and (b) scenario 3 after the needle is inserted into *phantom* tissue. Average deflection including error bars is plotted in both (a) and (b).

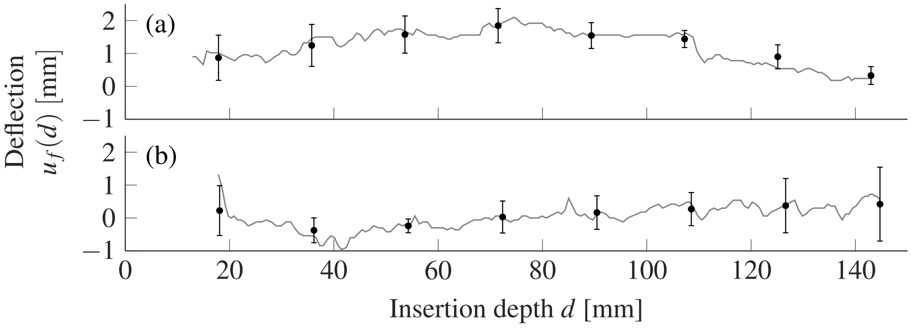

Figure 5.4: The needle deflection at the final insertion depth $u_f(d)$ for one insertion during (a) scenario 1 and (b) scenario 3 after the needle is inserted into *porcine* tissue. Average deflection including error bars is plotted in both (a) and (b).

ulation results presented in Section 5.3 and by the advice of an oncologist carrying out prostate brachytherapy procedures.

The choice of the steering action parameters is made so that the needle tip deflection at the final insertion depth and also the deflection of the entire needle are at a minimum as it is desired in prostate brachytherapy. The rotation depth d_r for scenario 1 and 3 was chosen so that the needle tip deflection at the final insertion depth is minimized. The lateral force quantity F_l was chosen for the same purpose but also to minimize the deflection of the entire needle at the final insertion depth. Four runs were carried out under scenario 1 and 3. Regarding scenario 2, it was found during the preliminary experiments that the achievable reduction of needle deflection when using only lateral force is rather limited. For this reason, no single optimal lateral force could be found and therefore only the results of the preliminary experiments (see Table 5.1, row 2) are presented in the following.

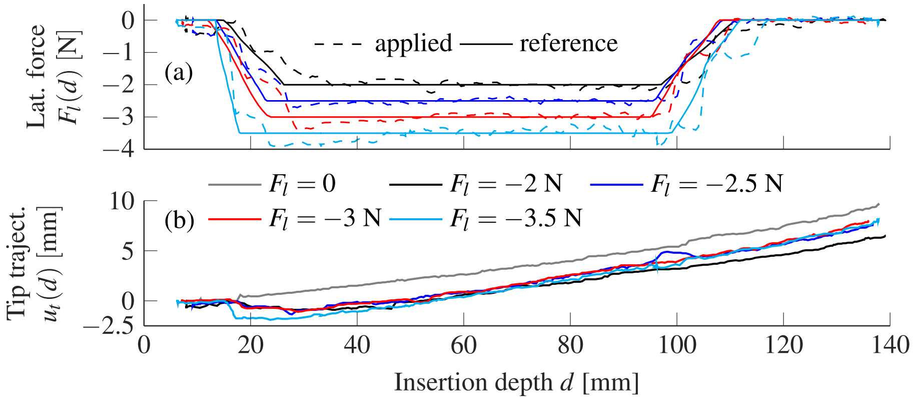

Figure 5.5: Needle insertion during scenario 2 into *phantom* tissue: (a) various applied lateral force profiles and (b) the corresponding needle tip trajectories (e.g., the paths cut by the needle tip) during insertion.

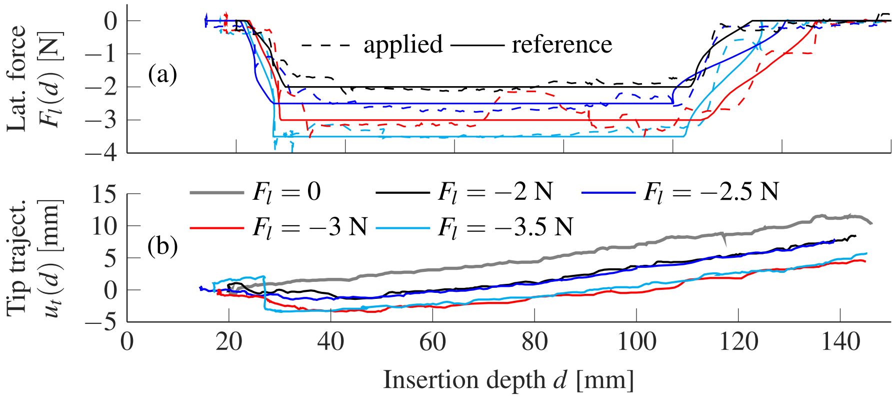

Figure 5.6: Needle insertion during scenario 2 into *porcine* tissue: (a) various applied lateral force profiles and (b) the corresponding needle tip trajectories (e.g., the paths cut by the needle tip) during insertion.

In all scenarios where lateral actuation is used, the constant force indicated in Table 5.1 is applied for an insertion depth range of 20 to 100 mm (see also Figure 5.5a and Figure 5.6a). This range was empirically determined based on a maximization of the lateral force's effect so that the force is removed when its influence on needle tip deflection is no longer apparent. To record the needle deflection after stopping insertion at the final depth, the actuated US transducer was moved from the needle tip towards the needle entry point into tissue at a velocity of 15 mm/s.

The only necessary interactions between human and machine are to signal the start of an insertion with the press of a button and the display of the current insertion depth on a screen.

5.4.2 Results

In Figure 5.3, the needle deflections at the final insertion depth for one run and during scenario 1 (Figure 5.3a) and 3(Figure 5.3b) are plotted along with averages among all four runs at various depths and error bars. When comparing the amount of deflection $u_f(d)$ shown in Figure 5.3a and Figure 5.3b, and Figure 5.4a and Figure 5.4b, less deflection can be observed during scenario 3 than during scenario 1 for both the phantom and porcine tissue.

Figure 5.5 and Figure 5.6 illustrate the results under scenario 2 for phantom and porcine tissue, respectively, according to Table 5.1 where Figure 5.5a and Figure 5.6a plot the applied forces, and Figure 5.5b and Figure 5.6b plot the corresponding needle tip trajectories. The needle tip deflection at the final insertion depth does not fall below approximately 7 mm regardless of the applied lateral force for the phantom tissue and not below 5 mm for the porcine tissue. For comparison, the needle tip trajectory for an insertion with no steering actions is also plotted in Figure 5.5b and Figure 5.6b. The 2 mm and 6 mm reductions in needle tip deflection at the final insertion depth are not by themselves substantial.

In Table 5.2, statistical results comparing the deflection shapes for scenarios 1 and 3 are listed. Scenario 2 was omitted in the analysis provided in Table 5.2 as the results depicted in Figure 5.5 clearly show insufficient reduction of deflection and thus no need for additional analysis. The mean of the absolute area under the needle shape $|A_e|$ is significantly lower for insertions carried out under scenario 3 compared to scenario 1 with a difference of approximately 70 mm^2 for phantom tissue and 104 mm^2 for porcine tissue. The same can be observed for the mean of the maximum needle deflection $\max(u_f)$ with a difference of approximately 0.9 mm for phantom tissue and 1 mm for porcine tissue. A two-sampled *t*-test evaluates whether a statistically significant difference between scenarios 1 and 3 for the average $|A_e|$ and the average $\max(u_f)$ exists. This shows whether significant improvement in needle deflection minimization was made under scenario 3 compared to scenario 1. The test decision given in Table 5.2 for both phantom and porcine tissue, indicates that for both cases the null hypothesis must be rejected at the 5% significance level so that the $|A_e|$ and the average $\max(u_f)$ are statistically significantly different. This implies that the means are unequal. The average needle tip deflection at the final insertion depth $u_f(140\ mm)$ for scenario 1 and 3 is given in the last column of Table 5.2. Although differences of 0.4 mm

Table 5.2: Statistical results for scenarios 1 and 3. $|A_e|$ is the absolute area under the needle shape, $\max(u_f)$ is the maximum of the observed needle deflection u_f, and $u_t(d_f)$ is the needle tip deflection at the final insertion depth d_f.

Scenario	Tissue		Average $\lvert A_e \rvert$ [mm^2]	Average $\max(u_f)$ [mm]	Average $u_t(d_f)$ [mm]
1	Phantom		112.87±29.33	1.39±0.23	0.4±0.3
	Porcine		165.37±50.57	2.07±0.32	0.28±0.34
3	Phantom		42.22±24.15	0.53±0.25	0±0.3
	Porcine		61.78±23.01	1.05±0.47	0.46±0.34
t-test	Phantom	h	unequal	unequal	equal
		p-value	0.01	0.002	0.09
	Porcine	h	unequal	unequal	equal
		p-value	0.01	0.01	0.77

for the phantom tissue and 0.18 mm for the porcine tissue exist, the *t*-test decision shows no statistically significant difference.

5.5 Discussion

The comparison between scenario 1 and 3 shows that using both steering inputs according to scenario 3 results in an almost entirely straight needle at the final insertion depth with very little remaining deflection. Both the maximum needle deflection and the absolute area under the needle (see Table 5.2, $|A_e|$) are significantly smaller for scenario 3 compared to scenario 1. The results presented for scenario 3 show that the needle deflection can be successfully minimized while both steering inputs axial rotation and lateral actuation are automated and insertion is carried out manually. This indicates a lower learning curve for novice surgeons, and helps to level out the seed placement accuracy curve for both experienced and novice surgeons. When only lateral actuation is used as needle steering input (scenario 2), although the needle deflection is reduced, the ability to minimize needle deflection is limited (see Figure 5.5 and Figure 5.6) meaning that the steering effect is also limited. When combined with axial needle rotation as steering input, however, considerable improvements are obtained. It is shown that the lateral force plays a supplementary but vital role along with axial rotation as far as reducing the needle deflection is concerned. It should be noted that during the experiments, the distance between the fixed needle guide (guide 1) and the tissue sample was

50 mm. It is presumed that the impact of the lateral actuation steering input with respect to needle deflection might significantly improve with reduced distance between fixed guide to tissue.

It could be argued that lateral needle actuation can cause safety issues for the patient in case of instability of the force controller. This issue can be avoided by inhibiting the lateral force by mechanically limiting the maximum displacement such that the maximum force that may be applied by the actuator is also limited. Furthermore, the actuator can be chosen so that its maximum mechanical energy does not exceed the maximally allowed energy introduced into the body.

5.6 Concluding Remarks

In this chapter, it is experimentally shown that using the steering input lateral needle actuation along with axial needle rotation can help to further minimize needle deflection. The experimental results confirm that lateral force application can significantly reduce deflection to an extent that is not possible with only one axial rotation. This chapter also introduces a collaborative human-in-the-loop approach for needle steering in prostate brachytherapy.

Chapter 6

Deflection Modelling for a Laterally Actuated and Axially Rotated Needle

6.1 Introduction

Towards the goal of utilizing lateral needle actuation during robot-assisted needle insertion, this chapter provides a mechanics-based model that accounts for both steering actions: lateral force and axial needle rotation. The model is intended to be used for both estimation and prediction of needle deflection during model-based needle steering. A detailed schematic depiction of the lateral needle actuation system, the modelling of the lateral force and tissue reaction is provided in Figure 6.1a. When using lateral force for needle steering, significant benefits exist, as found in Chapter 5. As the needle can be regarded as a highly under-actuated manipulator, the application of lateral force near the entry point into tissue provides an additional control input affecting the needle deflection more directly.

A question this chapter seeks to further explore particularly in the context of prostate brachytherapy is, to what extent can lateral force be used to manipulate the needle shape for minimizing needle deflection and what are the existing limitations? It is assumed that the effect of the lateral force with respect to steering is reduced with increasing insertion depth. Responsible for this is decreasing resistance to needle bending with increasing needle length and confinement of the needle within tissue during insertion. Therefore, lateral needle tip displacement caused by the lateral force and thus steerability are reduced at greater depths of lateral force application. This has likewise been hypothesized by Cowan *et al.* [93]. Moreover, it is of interest to know how lateral displacement and intermittent axial needle rotation should be combined to influence needle deflection and to properly steer the needle. Due to the needle-tissue system's nonlinearity and constraints (e.g., limited needle maneuverability due to under-actuation and non-holonomic properties), a model-based predictive

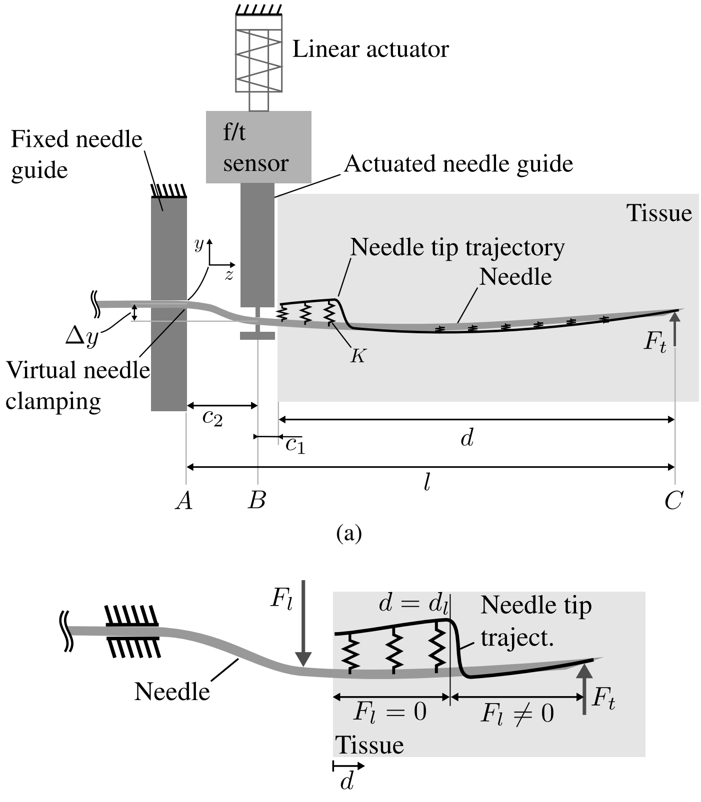

(a)

(b)

Figure 6.1: (a) A schematic of the needle being inserted into tissue with constraints enacted by the fixed needle guide and the actuated needle guide. The length l is the (variable) length of the needle section relevant for modelling and estimation. F_l is the force applied to the needle by the displacement of the actuated needle guide by Δy, which is measured by the f/t sensor. F_t is a tip-cutting-related point load. K is the tissue elasticity per unit distance modelled as elastic springs. (b) A close-up of the needle inside tissue with a force F_l applied laterally near the needle entry point illustrating F_l's effects on the needle shape. The difference between the needle shape and tip trajectory determines the elongation of the elastic springs.

control approach is necessary, which takes informed decisions based on prediction of needle deflection and on-line trajectory re-planning. A requirement of controlling needle deflection in a predictive manner is therefore the development of a model, with which the needle shape can be estimated and predicted based on the lateral needle displacement and axial needle rotation inputs. In this work, we introduce a model for the estimation of needle deflection resulting from a combination of applied lateral force and axial needle rotation. The model is energy-based and quasi-static, and its output is the needle shape that occurs at a given insertion depth d.

6.1.1 Related Work

In order to construct the model, the principle of minimum potential energy is used. This approach has been commonly applied in the past to model needle-tissue interactions and needle deflection during insertion. Misra *et al.* presented an energy-based mechanical model that takes into account needle bending (strain energy), needle-tissue interaction (compression and elasticity) and tip cutting work (tip force and rupture) [29, 20]. Roesthuis *et al.* [30] extended the model proposed by Misra *et al.* by modelling the resistive force due to tissue compression by a distributed load acting along the inserted needle portion and incorporating needle steering through axial rotation into the model. Another model that used an energy-based approach was proposed by Lee and Kim [34]. Rossa *et al.* [33, 35] in their version of an energy-based model considered also a cutting-related tip force and a load along the inserted needle portion modelled by a set of elastic springs. The springs model the tissue's resistance to compression. The spring stiffness is the tissue's Young's modulus. To determine the amount of tissue compression at a given position along the needle, the difference between the needle shaft shape and the needle tip trajectory, also referred to as the tip trajectory, is considered. Moreover, the (stationary) grid template commonly used in prostate brachytherapy is included in the model.

6.1.2 Objectives & Contributions

This chapter further investigates a novel method for automated needle trajectory manipulation during needle insertion into soft tissue based on two needle deflection manipulation methods commonly used during prostate brachytherapy, i.e., lateral force application and axial needle rotation. First, a model is presented which describes the needle-tissue system during insertion with the two manipulation methods applied. The model is developed for the purpose of predicting and estimating needle deflection during insertion into single- and multi-layer tissue. It extends the approach proposed by Rossa *et al.* to incorporate the actuated needle guide depicted schematically in Figure 6.1a.

The model is validated through insertion experiments carried out into phantom tissue samples under varying experimental conditions. The tuned conditions are lateral force magnitude F_l, depth of force application F_l and depth of 180° axial needle rotation. The experimental validations of the model are carried out with the prototype robotic assistant system described in Section 2.2. Further, control simulation and parameter sensitivity studies are performed to assess the added benefits of the lateral force on needle deflection reduction and the limitations of the lateral force application for control. The results of these studies can inform model-based deflection controllers.

The rest of this chapter is structured in the following order. In Section 6.2, the energy-based needle-tissue interaction model and solution for needle deflection are introduced. Section 6.3 presents the results of the model validation experiments. In Section 6.4 and Section 6.5, the results of the deflection control simulation and sensitivity study, respectively, are given. The results of Section 6.3, Section 6.4 and Section 6.5 are then discussed in Section 6.6. Finally, Section 6.7 offers concluding remarks.

6.2 Needle-tissue Interaction Modelling & Deflection Estimation

This section introduces the modelling approach for needle-tissue interactions, followed by solving the model for needle shape. The inputs to the model are the tip force F_t, with which needle rotation by 180° can be modelled, and the applied lateral force F_l. The model's output is needle deflection $u(z)$ with $z \in (0, l)$. The work presented in [33] is extended to incorporate a formulation for the actuated needle guide schematically depicted in Figure 6.1a. As the needle represents a slender beam that is clamped at one end and free at the other end, it is modelled as a cantilever beam. For the mathematical modelling of the needle-tissue system and the needle deflection occurring during insertion into tissue, Euler-Bernoulli beam theory is applied. A requirement for using Euler-Bernoulli beam theory for modelling of beam deflection is that the maximum deflection must be limited to approximately 10$\%$ of the overall beam length. With an overall needle length of up to 200 mm (e.g., a standard brachytherapy needle) and a maximum deflection of approximately 10 mm (see Section 6.3.1), this requirement is satisfied. The model is quasi-static as in each insertion step, equilibrium conditions are assumed.

As shown in Figure 6.1a, in contrast to previous work [35], only the needle section from points A to C is considered for modelling since the needle bending to the left side of the fixed needle guide is not relevant. This also decreases the mathematical complexity of the model, which is an important advantage for computational efficiency. The fixed needle guide is modelled as a virtual clamping at point A and the needle is considered as a beam with increasing length in each step during insertion such that the needle length l is a variable. Two point loads are applied at points B and C, respectively, and a distributed load modelled as linear springs acts along the inserted needle portion. The actuated needle guide applies a lateral point force (F_l) onto the point B proximal to the needle's entry point into tissue. The needle is displaced laterally through the applied force F_l by the guide. The needle guide essentially acts as a fulcrum, which can be displaced perpendicularly relative to the needle's insertion axis and about which the needle can pivot such that its slope can change. By applying lateral force and thus displacement in the appropriate direction, the trajectory that the needle follows inside tissue can be manipulated (see Figure 6.1b). The model is also designed to model multi-layer tissue where the amount of discrete layers is theoretically unlimited provided that the layer thickness is known.

6.2.1 Needle-Tissue System Model

The principle of minimum potential energy is used to formulate a mathematical model of the actuated needle-tissue system. The formulation captures the energy stored in the bent needle during insertion and the work applied to the needle-tissue system in the form of a functional, which is then transformed into a linear system of equations using the Rayleigh-Ritz method [94]. Finally, the linear system of equations is solved for the needle shape.

The system potential, which is the energy stored in the bent needle and tissue during insertion and the work applied to the needle-tissue system, is

$$\Pi(u) = U(u) + V = U_s(u) + U_d(u) + V_l + V_c \tag{6.1}$$

where $U(u)$ is the energy stored in the system due to needle displacement and V is the work applied to the system by the actuated needle guide (force F_l) and the needle tip (force F_t). U_s is the strain energy due to the bending of the needle and U_d is the energy stored in the displaced tissue. V_l and V_c are the works done by the actuated needle guide (F_l) at point B and the tip force F_t at point C, respectively. In the following, each of the terms appearing in (6.1) are detailed.

Strain energy U_s

As the needle bends during insertion into tissue, strain energy is stored in the needle, which is expressed as

$$U_s(u) = \int_0^l \frac{EI}{2} \left(\frac{\partial^2 u(d,z)}{\partial z^2} \right)^2 \, dz \tag{6.2}$$

where z is the horizontal coordinate, E and I are the needle's Young's modulus and area moment of inertia, respectively, l is the needle length and $u(d,z)$ is the needle shape at insertion depth d and z.

Potential Energy Stored in Displaced Tissue U_d

As the needle deflects as it is inserted into tissue, the tissue surrounding the needle is displaced. The energy stored in compressed single-layer tissue can be expressed as:

$$U_d(u) = \frac{K}{2} \int_{l-d}^{l} \Big(u(d,z) - u_t(d,z) \Big)^2 \, dz \tag{6.3}$$

where $u_t(d,z)$ is the (recorded or estimated) trajectory taken by the needle tip during insertion (needle tip trajectory, see Figure 6.1), K is the tissue stiffness expressed as force per unit length and d is the insertion depth. The tissue reaction is represented as virtual springs acting along the inserted needle portion as shown in Figure 6.1. The springs connect the needle shaft to the needle tip trajectory. Thus, the loading of the springs is dependent on the difference between the needle tip trajectory u_t and the needle shaft deflection u at a point z along the needle as shown in (6.3) and Figure 6.1a.

When for example two-layer tissue is considered, the integral in (6.3) can be separated as follows:

$$U_d(u) = \frac{K_1}{2} \int_{l-d}^{l-d_K} \Big(u(d,z) - u_t(d,z) \Big)^2 \, dz + \frac{K_2}{2} \int_{l-d_K}^{l} \Big(u(d,z) - u_t(d,z) \Big)^2 \, dz \tag{6.4}$$

where d_K is the depth at which the tissue layer and therefore the tissue stiffness changes. Extending the modelling of tissue to an arbitrary amount of discrete layers is now trivial provided the tissue layer thickness or depth of stiffness change is known.

Work Done by the Actuated Guide

The work done by the lateral force F_l applied by the actuated needle guide at point B at distance c_2 from the fixed needle guide is expressed as

$$V_l = F_l u(d, c_2) \tag{6.5}$$

where $u(d, c_2)$ is the needle deflection at point B.

Work Done by the Tissue Cutting Force (F_t)

The tip force shown as F_t in Figure 6.1a is the predominant reason for needle deflection during insertion into tissue and is caused by the asymmetric geometry of the bevelled needle tip. Due to the asymmetry, the tissue is displaced by the needle tip as the needle cuts through it. As a result of this, the needle deflects in the same direction as the bevel. Thus, the direction of F_t and the direction of deflection is determined by the orientation of the bevel. Upon needle rotation, the sign change of F_t needs to be carried out gradually (e.g., within 3 seconds, see Figure 6.4) in order to avoid a sudden jump in the needle deflection estimate. The work done by F_t is expressed as

$$V_c = F_t u(d, l) \tag{6.6}$$

where $u(d, l)$ is the needle tip deflection. It should be noted that the needle tip trajectory $u_t(d, l)$ is different from the needle tip deflection $u(d, l)$ in that the needle tip trajectory is constructed from tip deflections at past insertion steps and therefore depends on the horizontal coordinate z.

Finally, equations (6.2) - (6.6) are inserted into (6.1) to obtain the system energy model in the form of a functional:

$$\begin{aligned}\Pi(u) = &\int_0^l \frac{EI}{2} \left(\frac{\partial^2 u(d,z)}{\partial z^2} \right)^2 dz + \frac{K_1}{2} \int_{l-d}^{l-d_K} \Big(u(d,z) - u_t(d,z) \Big)^2 dz \\ &+ \frac{K_2}{2} \int_{l-d_K}^{l} \Big(u(d,z) - u_t(d,z) \Big)^2 dz - F_l u(d, c_2) - F_t u(d, l)\end{aligned} \tag{6.7}$$

where the two-layer tissue case is considered in (6.7) and is also used for the following derivation of the deflection model.

6.2.2 Solving for Needle Deflection

In order to solve the above introduced energy-based model of the needle-tissue system for the needle shape, as in previous works, the the Rayleigh-Ritz method is used. It is a variational method frequently applied to solve energy minimization problems and states that a differential equation in the form of a functional can be approximated by a finite sum of weighted shape functions. The following finite series represents the weighted shape functions [94]:

$$u_n(d,z) = \sum_{i=1}^{n} q_i(z) g_i(d) \tag{6.8}$$

Here, $q_i(z)$ is the i^{th} shape function and $g_i(d)$ is the corresponding weighting coefficient. $q_i(z)$ is given by [95, 26]:

$$q_i(z) = \frac{1}{\kappa_i}\left(\sin(\beta_i \frac{z}{l}) - \sinh(\beta_i \frac{z}{l}) - \gamma_i \Big[\cos(\beta_i \frac{z}{l}) - \cosh(\beta_i \frac{z}{l}) \Big] \right). \tag{6.9}$$

and represents the i^{th} vibration mode. κ_i and γ_i are computed as

$$\begin{aligned} \gamma_i &= \frac{\sin\beta_i + \sinh\beta_i}{\cos\beta_i + \cosh\beta_i} \\ \kappa_i &= \sin\beta_i - \sinh\beta_i - \gamma_i(\cos\beta_i - \cosh\beta_i). \end{aligned} \tag{6.10}$$

The values of the constants β_i for a cantilever beam (clamped-free) are $\beta_1 = 1.857$, $\beta_2 = 4.695$, $\beta_3 = 7.855$, $\beta_4 = 10.996$, and $\beta_i \simeq \pi(i - 1/2)$ for $i > 4$ [95]. The next step is to insert (6.8) into (6.7):

$$\begin{aligned} \Pi(u_n) =& \frac{EI}{2}\int_0^l \left(\sum_{i=1}^{n} q_i''(z) g_i(d)\right)^2 dz + \frac{K_1}{2}\int_{l-d}^{l-d_K} \left(\sum_{i=1}^{n} q_i(z) g_i(d) - u_t(d,z)\right)^2 dz \\ &+ \frac{K_2}{2}\int_{l-d_K}^{l} \left(\sum_{i=1}^{n} q_i(z) g_i(d) - u_t(d,z)\right)^2 dz - F_l \sum_{i=1}^{n} q_i(c_2) g_i(d) \\ &- F_t \sum_{i=1}^{n} q_i(l) g_i(d) \end{aligned} \tag{6.11}$$

where $q''(z)$ denotes the second derivative of $q(z)$ with respect to z. The condition for minimizing the potential $\Pi(u_n)$ is that $\frac{\partial \Pi}{\partial g_j} = 0$ for $j = 1, \ldots, n$. Using this condition, a linear system of equations can be established and solved for the unknown weighting coefficients g_i. In the following step, we take the partial derivative of $\Pi(u_n)$ with respect to $g_j(d)$ while considering that $q_i(l) = q_j(l) = 1, \forall i, j$, (see (6.9)) and that $q_j(c_2), \forall j$, is a known quantity:

$$\begin{aligned}\frac{\partial \Pi(u_n)}{\partial g_j(d)} =& EI \int_0^l \left(\sum_{i=1}^n q_i''(z) g_i(d) \right) q_j''(z)\, dz \\ &+ K_1 \int_{l-d}^{l-d_K} \left(\sum_{i=1}^n q_i(z) g_i(d) - u_t(d,z) \right) q_j(z)\, dz \\ &+ K_2 \int_{l-d_K}^{l} \left(\sum_{i=1}^n q_i(z) g_i(d) - u_t(d,z) \right) q_j(z)\, dz \\ &- F_l q_j(c_2) - F_t = 0. \end{aligned} \tag{6.12}$$

In order to simplify (6.12), the sum over index $i = 1, \ldots, n$ and $g_i(d)$ are extracted to obtain

$$\sum_{i=1}^n \phi_{ji} g_i(d) - \omega_j - \gamma_j - F_t = 0 \tag{6.13}$$

with

$$\begin{aligned}\phi_{ji}(z) &= EI \int_0^l q_i''(z) q_j''(z)\, dz + K_1 \int_{l-d}^{l-d_K} q_i(z) q_j(z)\, dz + K_2 \int_{l-d_K}^{l} q_i(z) q_j(z)\, dz \\ \omega_j(z) &= K_1 \int_{l-d}^{l-d_K} u_t(d,z) q_j(z)\, dz + K_2 \int_{l-d_K}^{l} u_t(d,z) q_j(z)\, dz \\ \gamma_j &= F_l q_j(c_2).\end{aligned}$$

(6.13) can now be re-written into a matrix formulation:

$$\Phi(z)\mathbf{g}(d) = \Gamma + F_t \mathbf{1}_{n\times 1} + \Omega(z) \tag{6.14}$$

with

$$\Phi = \begin{bmatrix} \phi_{11} & \cdots & \phi_{1n} \\ \vdots & \ddots & \vdots \\ \phi_{n1} & \cdots & \phi_{nn} \end{bmatrix};\ \Gamma = \begin{bmatrix} \gamma_1 \\ \vdots \\ \gamma_n \end{bmatrix};\ \Omega = \begin{bmatrix} \omega_1 \\ \vdots \\ \omega_n \end{bmatrix};\ \mathbf{g} = \begin{bmatrix} g_1 \\ \vdots \\ g_n \end{bmatrix}$$

and where $\mathbf{1}_{n\times 1}$ is a column vector of ones of size n. Finally, we can solve for the unknown vector $\mathbf{g}$

$$\mathbf{g} = \Phi^{-1}\big(\Gamma + F_t\mathbf{1}_{n\times 1} + \Omega\big) \tag{6.15}$$

and insert (6.15) into (6.8) in order to calculate the estimated needle shape $u_n(d, z)$.

6.2.3 Model Parametrization

The model takes as parameters the tissue stiffness K and the needle tip force F_t. Here, the methods for obtaining K and F_t are introduced.

Tissue Stiffness K

The tissue stiffness K is measured physically via compression tests. The fact that the parameter K in the model is not dependent on u suggests that K is constant for the considered deflection. Thus, to determine K, Hooke's law $\sigma = K\epsilon$ is used where σ is the stress resulting from the applied strain ε during the compression test. More specifics regarding the experimental setup used for compression tests are given in Section 6.3.1.

Tip force F_t

The second parameter to be obtained is the tip force F_t. To estimate the parameter, the needle tip deflection measured during insertion is used, combined with a modified version of (6.14) and the measured K. The measured needle tip deflection u_t and a special case of (6.9), which occurs at $z = l$ where $q_i(l) = 1 \; \forall \; i$, can be used to obtain

$$u(d, l) = \sum_{i=1}^{n} g_i(d) = u_t. \tag{6.16}$$

Using (6.16), we can now expand (6.14) to $n + 1$ equations as follows [35]:

$$\underbrace{\begin{bmatrix} \Phi & -\mathbf{1}_{n\times 1} \\ \mathbf{1}_{1\times n} & 0 \end{bmatrix}}_{\Phi^*} \underbrace{\begin{bmatrix} \mathbf{g} \\ F_t \end{bmatrix}}_{\mathbf{g}^*} = \underbrace{\begin{bmatrix} \Gamma \\ 0 \end{bmatrix}}_{\Gamma^*} + \underbrace{\begin{bmatrix} \Omega \\ 0 \end{bmatrix}}_{\Omega^*} + \underbrace{\begin{bmatrix} \mathbf{0}_{n\times 1} \\ u_t \end{bmatrix}}_{\Lambda}. \tag{6.17}$$

Table 6.1: The four considered experimental scenarios.

Scenario #	Lateral force F_l [N]	Depth of application d_l [mm]	Rotation depth d_r [mm]	Tissue type
1	0	x	x	single layer
2	-2.5	20	x	
3	-2.5	20	100	
4	-2.5	45	x	
5	0	x	x	multi layer
6	-2.5	20	100	

Finally, (6.17) can be solved for $\mathbf{g}^*$ as

$$\mathbf{g}^* = \Phi^{*-1}\big(\Gamma^* + \Omega^* + \Lambda\big) \tag{6.18}$$

in order to obtain the tip force F_t.

6.3 Model Validation

In this section, an experimental validation of the model proposed in Section 6.2 is given. The insertions are carried out with the experimental setup described in Section 2.2. The performance of the model in estimating the needle tip deflection during insertion into phantom tissue made from plastisol is presented. The needle tip deflection measured during insertion is compared to the tip deflection estimate through a statistical analysis.

6.3.1 Experimental Results

Six different experimental scenarios are chosen. The scenarios are listed in Table 6.1. The variables listed in Table 6.1 are described as follows. F_l is the magnitude of the lateral force applied onto the needle by the actuated guide near the needle's entry point into tissue, d_l represents the needle insertion depth in millimeters after which the lateral force F_l is applied by the actuated needle guide (see Figure 6.1b) and d_r is the 180° axial rotation depth in millimeters. In all scenarios where $F_l \neq 0$ N, the force F_l is removed at an insertion depth of 100 mm. The above choices were purposefully made with the intention to mimic steering actions performed by surgeons in a clinical scenario to reduce the deflection of the needle inside tissue. The sign of F_l is chosen such that its direction is against the direction of deflection caused by the needle tip bevel. By choosing scenarios with different depths d_l for application of the lateral force F_l, its effect on the magnitude of a deflection reduction will be shown. Since a combination of needle rotation and lateral force is modelled, the combined effects of F_l and rotation towards minimization of deflection is presented in scenario 3 (see Table 6.1). Thus, d_r is chosen such that the combined effect of F_l and rotation further reduce needle deflection. During scenario 5 and 6, the needle is inserted into a phantom tissue sample consisting of two tissue layers with different Young's moduli. These scenarios are considered to validate the multi-layer version of the deflection model where the model is provided with the two different layer stiffnesses and the thickness of the first layer. The interface depth of the two layers d_K is chosen to be 50 mm, a depth at which a human prostate is commonly located. Details regarding the quantification of the Young's moduli of the two layers are given in the following section.

For each scenario, six insertions are carried out. The needle used for the insertions is a standard hollow 18G (∅ 1.27 mm) brachytherapy needle (Eckert & Ziegler BEBIG Inc., Oxford, CT, USA), which has a length of 200 mm and is made from stainless steel (Young's modulus $E = 200$ GPa). During scenario 1 to 4, the needle is inserted 24 times into the single-layer sample of phantom tissue made from Plastisol (5.0 Soft Plastisol, M-F Manufacturing, Fort Worth, TX, USA) and during scenarios 5 and 6, the needle is inserted 12 times into a two-layer plastisol tissue sample. The distance $c = c_1 + c_2$ (see Figure 6.1a) is set to 36 mm during scenario 1 to 4 and to 42 mm during scenario 5 and 6. In all scenarios, the distance c_1 is set to 9 mm.

Model Parameter Identification

Before a model estimate can be obtained, the parameters K and F_t need to be identified for the two tissue samples described above. Figure 6.2a shows the setup used for the compression tests. One of the cylindrical samples used for the tests is depicted in Figure 6.2b. The sample is made from the same tissue batches as used for insertion experiments. The tissue sample is clamped in between a rigid surface on the right hand side of Figure 6.2a and an indenter with a circular area on the left hand side. The indenter is connected to a force sensor to measure the forces applied to the tissue sample. In order to apply pressure, the indenter

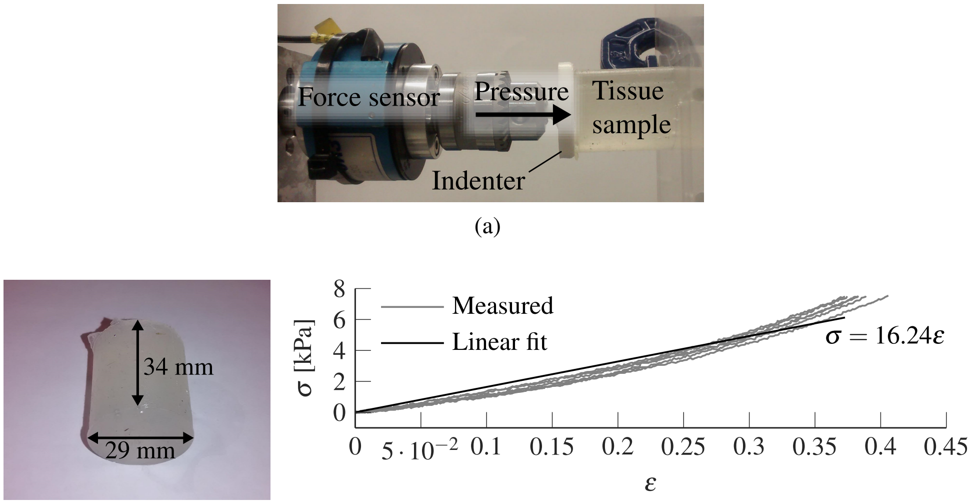

(a)

(b)

(c)

Figure 6.2: (a) The setup and (b) the tissue sample used for compression experiments. (c) Stress-strain curves for six trials of compression tests including a linear fit. The following stiffness was calculated for the homogeneous tissue sample: $K = \frac{\sigma}{\varepsilon} = 16.24$ kPa.

is displaced to the right hand side with a constant rate of 1 mm/s for a maximum distance of 20 mm or until a force of 5 N is measured by the force sensor. Six trials of this experiment are carried out. A sample result of the compression test for the single-layer tissue sample is shown as a stress/strain curve in Figure 6.2c. Also shown in Figure 6.2c is the linear fit to the measured data, which indicates that Hooke's law $\sigma = K\varepsilon$ applies where σ is the stress occurring within the tissue sample caused by the applied strain ε. Finally, the measured tissue Young's modulus K for the single-layer tissue is 16.24 kPa. This value is close to the Young's modulus of prostate tissue [96]. The measured K for the first layer of the two-layer tissue is 21.59 kPa (K_1) and for the second layer it is 13.36 kPa (K_2).

In order to estimate the force F_t occurring at the needle tip for the phantom tissue samples, the measured needle tip deflection obtained from scenario 1 and 5 (see Table 6.1) for the single-layer and two-layer tissue samples, respectively, is used. It should be noted that needle tip deflection measurements obtained only from scenario 1 and 5 are used to identify the needle tip force F_t for the single- and two-layer tissue. Tip deflection measurements taken during insertions of the other scenarios are only used as ground truth for model validation. The proposed model for estimating the needle shape during insertion does not take as input measured needle tip deflection. In Figure 6.3, the mean tip force estimate obtained from (6.18) for six insertion trials is plotted against the insertion depth. To determine the fi-

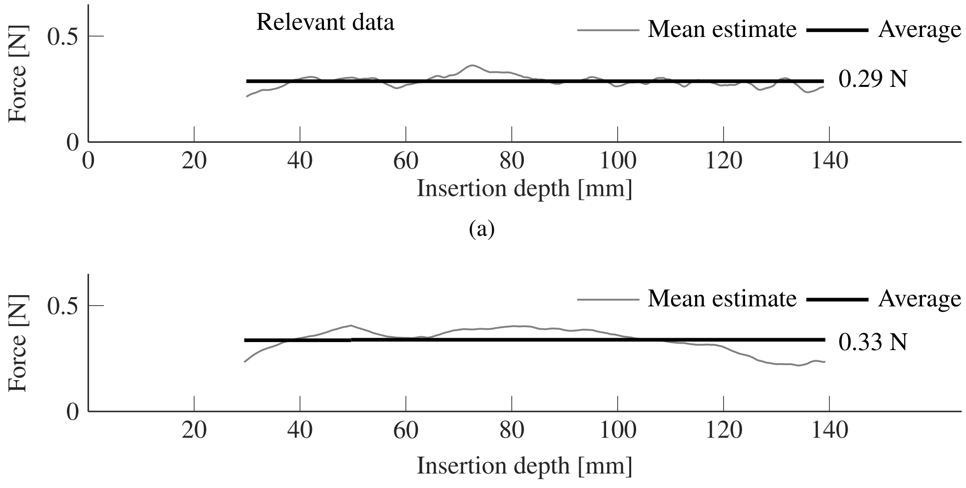

(a)

(b)

Figure 6.3: The needle tip force estimation results. The mean tip force estimate of six insertions according to (a) scenario 1 and (b) scenario 5 (see Table 6.1) obtained from (6.18) are plotted along with the averaged constant tip force F_t. The final estimate of the needle tip force is $F_t = 0.29$ N for the single-layer tissue sample and $F_t = 0.33$ N for the two-layer tissue sample.

nal constant F_t, the average of the estimated mean tip force curve is taken. Only data beyond a depth of 30 mm is considered (see Figure 6.3) for obtaining the constant tip force F_t since the data at shallower depths is rather noisy (not reflected in the plots). This is due to the fact that the needle tip deflection measured by the image-based needle tip tracking algorithm (see Section 2.3.2) contains more noise at shallow insertion depths. The resulting average tip force is $F_t = 0.29$ N for the single-layer tissue (see Figure 6.3a). To identify the tip force for the two-layer tissue, the two-layer version of the model is applied. The tip force for each layer is calculated separately but as the difference between the two is negligible, the same tip force of $F_t = 0.33$ N for each layer of the two-layer tissue is used (see Figure 6.3b). As can be observed, the estimates of F_t are roughly constant, which is physically understandable because the amount of tissue displacement effected by the bevelled tip is constant.

Validation Results

The measured and estimated needle tip trajectory curves are plotted in Figure 6.4a to Figure 6.4f against the insertion depth. The plots show one out of the six insertions for each scenario. Plotted below the tip deflection is the error between measured and estimated tip deflection, the tip force F_t, and the applied lateral force F_l. The plot showing the progres-

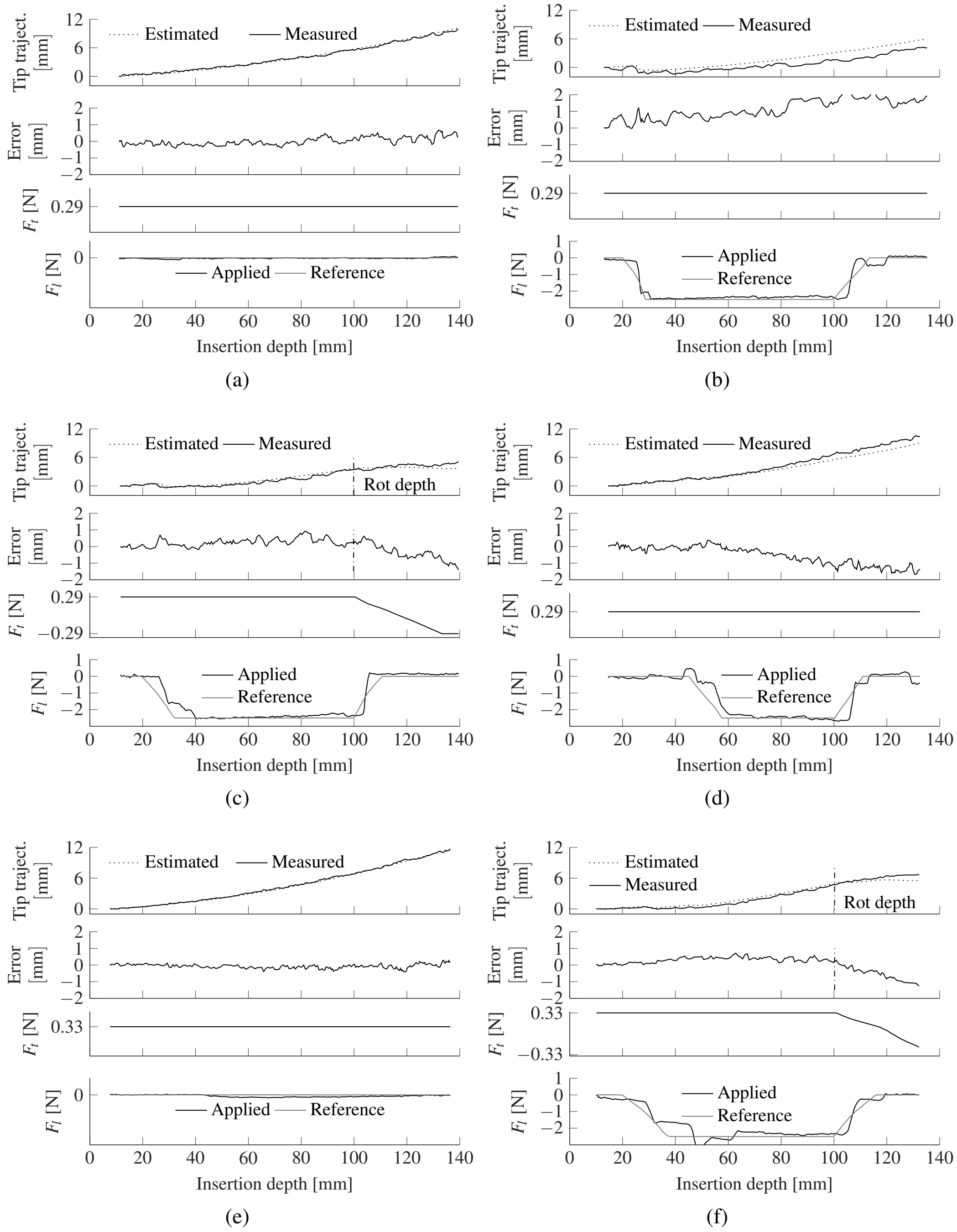

Figure 6.4: Results for needle tip trajectory estimation for experimental scenarios (a) without any corrective measures, (b) $F_l = -2.5$ N and $d_l = 20$ mm, (c) $F_l = -2.5$ N, $d_l = 20$ mm, and $d_r = 100$ mm, (d) $F_l = -2.5$ N and $d_l = 45$ mm, (e) without any corrective measures and two-layer tissue, and $F_l = -2.5$ N, $d_l = 20$ mm, $d_r = 100$ mm and two-layer tissue.

Table 6.2: Statistical results of the experimental scenarios. Results of a two-sample t-test are shown (h). The mean error between measured and estimated needle tip deflection ($\bar{e}$) and the standard error ($\sigma/\sqrt{n}$) over six trials for four insertion depths are listed (units mm). Measured and estimated tip deflections over 6 trials are compared.

Trial #	Insertion depth [mm]									
	30		60		90		120		140	
	h	$\lvert\bar{e}\rvert \pm \frac{\sigma}{\sqrt{n}}$	h	$\lvert\bar{e}\rvert \pm \frac{\sigma}{\sqrt{n}}$	h	$\lvert\bar{e}\rvert \pm \frac{\sigma}{\sqrt{n}}$	h	$\lvert\bar{e}\rvert \pm \frac{\sigma}{\sqrt{n}}$	h	$\lvert\bar{e}\rvert \pm \frac{\sigma}{\sqrt{n}}$
1	$\bar{r}$	0.19±0.1	$\bar{r}$	0.33±0.21	$\bar{r}$	0.51±0.27	$\bar{r}$	0.7±0.37	$\bar{r}$	0.83±0.44
2	r	0.87±0.22	r	1±0.21	r	0.92±0.25	r	1.26±0.39	r	1.29±0.39
3	$\bar{r}$	0.25±0.15	$\bar{r}$	0.55±0.24	$\bar{r}$	0.65±0.3	$\bar{r}$	0.86±0.38	$\bar{r}$	1.22±0.5
4	$\bar{r}$	0.38±0.2	$\bar{r}$	0.41±0.18	r	0.89±0.1	r	1.24±0.12	r	1.48±0.18
5	$\bar{r}$	0.11±0.05	$\bar{r}$	0.11±0.05	$\bar{r}$	0.35±0.14	$\bar{r}$	0.29±0.22	$\bar{r}$	0.46±0.21
6	$\bar{r}$	0.15±0.09	$\bar{r}$	0.36±0.19	$\bar{r}$	0.43±0.23	$\bar{r}$	1.11±0.37	r	1.98±0.41

r denotes that the null hypothesis must be rejected and $\bar{r}$ denotes that it can not be rejected at the 5% significance level.

sion of the 'Applied' force F_l is the lateral force provided to the needle-tissue model. As expected, scenario 1 and 5 depicted in Figure 6.4a and Figure 6.4e, respectively, show a very accurate estimate. The error remains within 0.8 mm for scenario 1 and 0.5 mm for scenario 5. During scenario 2, which is plotted in Figure 6.4b, the error monotonously increases to roughly 2 mm at the final insertion depth. The result of scenario 3 is shown in Figure 6.4c. Compared to scenario 2, a needle rotation is added to the otherwise equal conditions. The estimate is more accurate than the one in scenario 2 throughout insertion. After 100 mm depth, the model begins to slightly under-estimate the needle tip trajectory with a maximum error of approximately -1.5 mm at the final depth of 140 mm. A tip trajectory measurement and estimate for scenario 4 is shown in Figure 6.4d. Here, the error remains below 1 mm up to an insertion depth of 60 mm but slightly increases as the model under-estimates the tip trajectory beyond 60 mm depth with a maximum error of approximately 1.5 mm at the final insertion depth. Scenario 6, where two-layer tissue is used, shows an accurate estimate with an error of less than 1 mm below 100 mm insertion depth. The estimation performance is very similar to scenario 2 where the same lateral force profile and axial needle rotation depth are applied, while during scenario 6, the needle is inserted into two-layer tissue. Beyond a depth of 100 mm, the error monotonously increases to roughly 2 mm at the final insertion depth.

To further examine the accuracy of the needle-tissue model, a statistical analysis is provided. In order to show whether the estimation error is statistically significant, a two-sample *t*-test is carried out. The null hypothesis of the test states that no significant difference exists between the measured and estimated needle tip trajectory. The test has a 5% significance level and the sample size is six. The results listed in Table 6.2 indicate whether the null hypothesis must be rejected or not. Furthermore, in Table 6.2, the mean absolute error $|\bar{e}|$ between the measured and estimated needle tip trajectory and the standard error $\sigma/\sqrt{n}$ across the $n = 6$ runs are listed. The results presented in Table 6.2 confirm the observations made in Figure 6.4 and described further above.

6.4 Deflection Control Simulation

A needle tip deflection control simulation study is carried out with the purpose of assessing the performance and limitations of a simple ad-hoc controller that combines the two control inputs lateral force and axial needle rotation. Moreover, advantages of combining the two control inputs are explored. The needle tip deflection is controlled through a combination of 180° axial needle rotation and lateral force F_l application. The control method is schematically illustrated in Figure 6.5. The controller for needle rotation is based on a bang-bang controller where a needle rotation by 180° is triggered when a tip deflection magnitude of $\tau = 1$ mm is exceeded. The applied lateral force F_l is adjusted by a PI controller where the reference tip deflection is zero. The previously identified model parameter values $K = 16.24$ kPa and $F_t = 0.29$ N for the single-layer phantom tissue sample are used for the simulation. The four considered control scenarios are listed in Table 6.3. In control scenario 1, the needle tip deflection is deliberately not controlled for performance assessment of control scenario 2 to 4. The PI gains of the lateral force controller are empirically determined to result in the best possible performance. Figure 6.6 shows the simulation results for the four control scenarios where the top sub-plot shows the needle tip deflection trajectories and the bottom sub-plot shows the applied lateral force F_l during control scenario 3. While only using lateral force to control needle tip deflection (control scenario 3), the controller is initially able to minimize the tip deflection but fails with increasing insertion depth. It can be observed that the needle tip deflection can not be reduced at greater insertion depths despite

Table 6.3: The control input combinations.

Control scenario	Lateral force application	Axial rotation
1	no	no
2	no	yes
3	yes	no
4	yes	yes

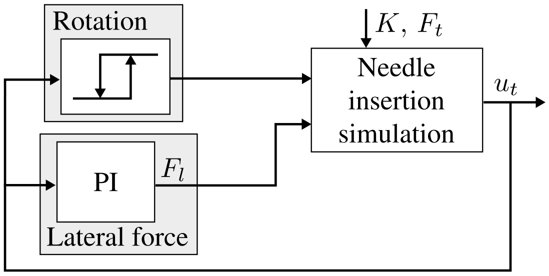

Figure 6.5: The schematic for simulated control of needle tip deflection (u_t) using multiple 180° axial needle rotations and application of lateral force F_l. The 180° axial needle rotation is commanded by a bang-bang controller. The needle rotations from 0° to 180° and vice versa are triggered when a tip deflection threshold is exceeded.

the increasing magnitude of F_l until the saturation point of 10 N is reached. The reason for the decreased ability of the lateral force actuation to move the needle tip laterally is due to the needle being supported by tissue and the needle's decrease in resistance to bending with increasing length. The limitations of the lateral force with respect to needle insertion depth is further studied in Section 6.5. When controlled axial needle rotation is added to lateral force control during insertion (control scenario 4), the needle tip deflection can be reduced to below 1 mm at the final insertion depth with three rotations. When only axial rotation is considered without lateral force as in control scenario 2, the needle tip deflection also remains within 1 mm during insertion. However, four axial needle rotations are necessary to achieve the same outcome compared to control scenario 4.

6.5 Sensitivity Analysis

This section provides results of a sensitivity analysis with respect to the lateral force F_l and its depth of application d_l in order to highlight achievable steering goals with a focus on minimizing the needle's deflection and the influence of d_l on needle deflection.

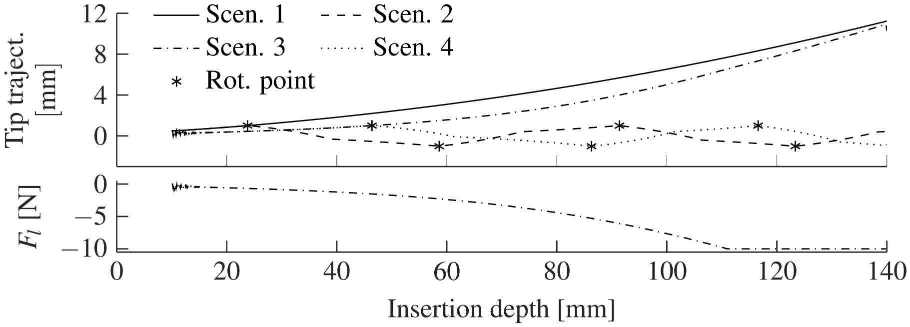

Figure 6.6: The needle tip deflection trajectories during needle insertion (top sub-plot) and the lateral force F_l applied during control scenario 3 (bottom sub-plot).

Needle insertion simulations using the proposed model are carried out with the same parameters $F_t = 0.29$ N and $K = 16.24$ kPa as obtained for the phantom tissue used for experimental validation. Three different constant lateral force magnitudes, F_l = [-1.5 -2.5 -3.5] N, and seven depths at which application of F_l is started, d_l = [10 15 20 30 40 50 60] mm, are considered, resulting in 21 simulations.

The simulation results are plotted in Figure 6.7 where Figure 6.7a shows simulated needle shapes at the final insertion depth of 140 mm. Each plot shows needle shapes for one of three investigated lateral forces and all considered depths of force application. By increasing the lateral force magnitude applied to the needle shaft, a smaller needle deflection can be achieved compared to a lower force magnitude. Moreover, shallower depths of force application, e.g., $d_l \leq 20$ mm, result in the least needle deflection, which is expected. The reasons for this are further discussed in Section 6.6. Figure 6.7b provides a supplementary analysis of the plots provided in Figure 6.7a with an emphasis on the needle tip deflection at the final insertion depth of 140 mm and how it is influenced by the depth of application of the lateral force. It shows the amount by which needle tip deflection can be reduced (in percent) for increasing lateral force magnitudes and their associated depths of application. The comparison is made with respect to needle deflection without steering inputs. An application depth of 10 mm and a lateral force magnitude of -3.5 N shows a $\sim$90% (the highest) reduction, while a magnitude of -1.5 N shows an approximately 40% (the lowest) reduction. The curves furthermore suggest a decline in the reduction in tip deflection at increasing force application depths with almost no reduction occurring at a force application depth of 60 mm.

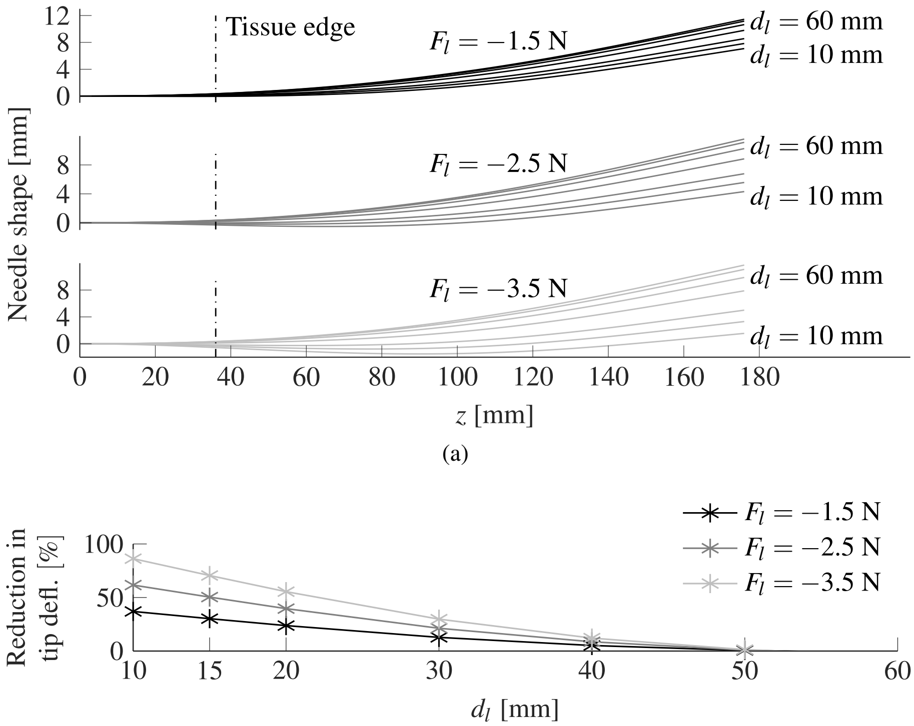

(a)

(b)

Figure 6.7: The effect of lateral force applied at various d_l. (a) Simulation results for needle shape with three different lateral forces F_l applied at seven different depths $d_l = [10 \;\; 15 \;\; 20 \;\; 30 \;\; 40 \;\; 50 \;\; 60]$ mm. (b) The influence of d_l on needle tip deflection after needle insertion is stopped. The plot shows the amount of reduction of needle deflection in percent at the final insertion depth for various d_l and F_l. The comparison is made with respect to needle deflection with $F_l = 0$ and no axial rotation.

6.6 Discussion

The results of the experimental validation show that the differences between the measured and estimated trajectories are not statistically significant for most cases up to 120 mm insertion depth according to Table 6.2. This suggests that the lateral needle displacement caused by the application of the lateral force F_l is modelled well. According to the t-test results, the estimated and measured tip trajectories are significantly different during scenario 2 and scenario 4 where the error does not exceed 1.5 mm at the final insertion depth. This demonstrates that the proposed model represents the physical needle-tissue system well considering that the tissue stiffness K used as input to the model represents a physical property of the phantom tissue sample. When considering scenarios 5 and 6, the multi-layer version of the deflection model performs similarly to the single-layer version.

The error significance, however, increases during most scenarios as the needle approaches the final insertion depth. According to Table 6.2, the error significance increases with an overall maximum $|\bar{e}|$ of 1.98 mm occurring during scenario 6 and insertion depth 140 mm. Considering that a standard brachytherapy needle's inner diameter and thus the radioactive seed diameter is about 1 mm, and that the error compared to the tip deflection without correction is approximately 80% less, this error is an acceptable deviation. Moreover, when the deflection model is applied to needle steering, where a model-based controller would adjust the needle deflection using lateral actuation and axial rotation to reach a defined target, the controller can also adjust the model parameters in order to account for and correct model prediction errors using online feedback of the needle deflection (e.g., ultrasound-based).

In Section 6.4, a rudimentary ad-hoc control simulation is presented for the minimization of needle tip deflection during insertion. The control parameters are empirically determined to yield the best possible results for the specific combination of model parameters K and F_t. Due to the limitations of lateral force application on needle tip deflection shown in Section 6.5, the lateral force controller is not able by itself to minimize needle tip deflection at greater insertion depths. Therefore, using a controller that is based purely on the feedback of the current needle tip deflection is not enough for reliable and adaptive needle deflection control. To achieve the deflection minimization results shown in Section 6.5 by applying lateral force only, a more sophisticated controller is needed that uses the proposed model for prediction-based control decisions and takes into account the knowledge gained from Section 6.5.

When a combination of lateral force and axial rotation is applied for needle tip deflection control, less needle rotations are necessary to achieve a similar needle tip trajectory than when only axial needle rotation is used. Due to the nonlinear nature of the needle-tissue system that has no equilibrium point other than when the insertion speed is zero, as long as the needle moves, its trajectory will diverge from a straight line, which is physically understandable due to the effect of the bevelled tip. Therefore, if the goal is to keep the needle tip on straight line (as it is in prostate brachytherapy due to assumptions made during seed deposition planning), the axial rotation input needs to be invoked continually to keep the tip deflection below a given threshold. However, with two control inputs, namely the axial rotation and the lateral force, the level of activity or magnitude of each control input

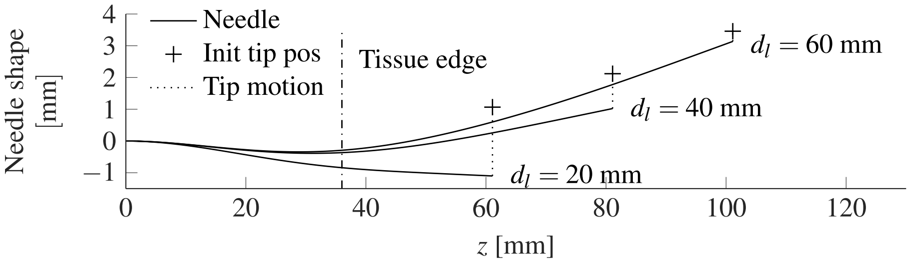

Figure 6.8: Needle shapes for three different simulations with various depths of application d_l. The change in needle tip position is shown during the switch from $F_l = 0$ N to the full magnitude of $F_l = -3.5$ N.

is less. Thus, since excessive use of axial rotation results in tissue drilling effects [68], the availability of an additional control input (the lateral force) is highly beneficial.

The results of the sensitivity analysis with respect to reduction of needle deflection presented in Section 6.5 are a somewhat expected outcome based on the observations made in Section 6.4. The behaviour of the needle when the lateral force is applied at varying depths is further illustrated in Figure 6.8. There is more tissue support as the needle is inserted deeper into tissue, and the needle's bending stiffness with increasing length is reduced. As a result of this, a needle that is inserted deeper into tissue bends more rather than the entire needle shaft being moved laterally. Therefore, the needle tip is also subject to less lateral motion when F_l is applied at greater depths, which in turn significantly diminishes the potential to reduce needle deflection as shown in Figure 6.7b.

The results presented in Section 6.5 show that a combination of lateral force F_l and depth of application d_l exists that results in a 90% reduction of needle tip deflection ($F_l = -3.5$ N and $d_l = 10$ mm, see Figure 6.7b). Therefore, it is possible to fully eliminate needle deflection by only applying lateral force. Combining lateral force with rotation, however, provides an additional method of steering, meaning that less lateral force is necessary to obtain the same outcome for a given level of reduction of needle tip deflection.

The possible applications for the model presented in this work are on-line needle deflection estimation and prediction. A control algorithm using a model-based predictive control (MPC) approach can be designed for automated needle steering using an appropriate combination of lateral force F_l and needle rotation based on the knowledge gained from Section 6.4 and Section 6.5. The control algorithm will also be able to correct for the model errors apparent from Section 6.3 by adjusting model parameters or control inputs accordingly.

6.7 Concluding Remarks

This chapter proposes a novel method for automated needle steering during insertion into soft tissue, and a model that is used to estimate the needle deflection during insertion based on the novel steering method. The method combines the application of a lateral force near the needle entry point into tissue with axial needle rotation. An energy-based model is introduced for the estimation and prediction of needle deflection during insertion taking into account the lateral force and the axial rotation. The model is appropriate for model-based needle deflection control. It is experimentally validated and shown to estimate needle tip deflection with good accuracy for single- and two-layer tissue. Simulations of needle insertions using the proposed model exhibit the steering effects, potentials and limitations of lateral force application in terms of reducing needle tip deflection. The simulation results confirm the assumption that the influence of lateral force on needle shape inside tissue is reduced with increasing insertion depth, but also demonstrate that it is possible to reduce needle deflection by as much as 90%. The model presented in this chapter represents a first step towards designing control methods for needle deflection using a combination of lateral force and axial rotation.

Chapter 7

Model-based Needle Steering Using Lateral Actuation

This chapter proposes a novel needle steering method that uses lateral needle actuation near the needle entry point into tissue. As described in Section 1.1.1, controlling the needle (tip) deflection towards a desired trajectory during insertion, e.g., zero tip deflection, is commonly done through axial needle rotation in case of a bevel tip needle.

As demonstrated in Section 6.5, at higher insertion depths, the influence of lateral force on the needle tip deflection declines. This is due to a combination of the needle being constrained by tissue and the needle's loss of resistance to bending with increasing needle length. The amount of force applied at a shallow insertion depth is therefore crucial in reducing the amount of needle deflection at the depth section of interest. As shown in Section 6.4, a primitive control law such as a simple PID controller is not sufficient to control deflection using lateral needle actuation. A deflection controller must be able to project the lateral force that needs to be applied at a shallow depth to achieve the desired deflection at the final insertion depth. The behaviour of the needle at a given insertion depth can be estimated and predicted with the deflection model presented in Section 6.2.

In this chapter, a model-based approach for needle steering using only lateral actuation is investigated. Only lateral actuation as steering input is considered as this further exposes possible limitations and explores the actuation method's potential beyond the simulations provided in Section 6.4 and Section 6.5.

The steering approach consists of two phases where during the first phase, the trajectory planning phase, the desired needle tip trajectory is found that brings the needle to a desired target. During the second phase, as the needle is inserted, a real-time model-based algorithm for needle tip trajectory adjustment uses the US-image-based needle tip deflection measurement in order to adjust the applied lateral force such that the error between the pre-planned needle tip trajectory and the measured needle tip deflection is minimized. In a scenario where the deflection model represents the needle deflection inside tissue entirely correctly,

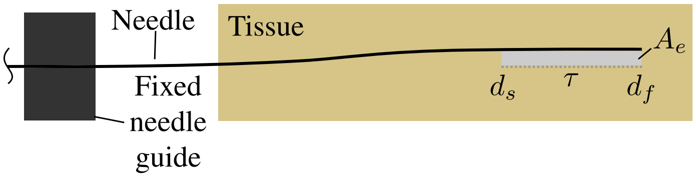

Figure 7.1: The considered control objective commonly occurring during prostate brachytherapy, which is to minimize the area A_e under the line segment τ.

the second phase of real-time trajectory re-planning would not be needed. As, however, the deflection model introduced in Section 6.2 does not, as most models representing physical systems do not, perfectly represent the needle-tissue system, adjusting the lateral force online as needed is required to account for model inaccuracies.

7.1 Needle Steering

In any needle steering scenario, either the needle tip is steered towards a target point or a section of the needle must reach a desired line segment. Figure 7.1 shows the latter needle steering objective where the needle's distance to the line segment τ at the final insertion depth must be minimized. In this study, the above steering objective is chosen as it is commonly encountered in prostate brachytherapy for the reasons presented in Section 1.1.1. As indicated by the simulation results presented in Section 6.5, this can be achieved solely through the use of the control input lateral actuation.

Given the desired steering target, the proposed control method first iteratively determines an optimal needle tip trajectory that achieves the steering objective using the deflection model introduced in Section 6.2.

7.1.1 Needle Tip Trajectory Planning

During the first phase, the trajectory planner uses the needle deflection model from Section 6.2 to find the optimal needle tip trajectory that steers the needle towards its target. The model is used to establish a cost function that minimizes the area A_e (see Figure 7.1). Considering that generally, the search space for the lateral force profile $F_l(d)$ is infinite, the simplified function

$$F_l(d, d_{l,1}, d_{l,2}) = F_{l,c}\left[h(d - d_{l,1}) - h(d - d_{l,2})\right] \tag{7.1}$$

is chosen for the force profile to reduce the search space. The function $h(\cdot)$ is a step function, $F_{l,c}$, $d_{l,1}$, and $d_{l,2}$ represent the constant force magnitude, and the start and end depths at which $F_{l,c}$ is applied, respectively. The cost function constructed from (7.1) that returns the residual between the target line section τ and the needle shape at the final insertion depth is given as

$$R(F_{l,c}, d_{l,1}) = \sum_{z_\tau \in (d_s, d_f)} \Big(u_f(z_\tau, F_{l,c}, d_{l,1}) - \tau\Big)^2 \tag{7.2}$$

and constitutes a sum of squared differences. u_f is the simulated needle deflection at the final insertion depth obtained from the deflection model. The inputs to the cost function that are adjusted to minimize R are the constant lateral force magnitude $F_{l,c}$ and the application depth of $F_{l,c}$, $d_{l,1}$. The depth $d_{l,2}$ is chosen to be a depth where the lateral actuation ceases to be effective based on prior information apparent from experimental and simulation studies. The optimization algorithm chosen to find the optimal values of the parameters $F_{l,c}$ and $d_{l,1}$ is pattern search [97]. Pattern search is an iterative optimization algorithm that does not require a gradient and therefore can be applied to any function that is not continuous or differentiable. The algorithm evaluates the objective function at defined distances in all dimensions around the current point and chooses the evaluated point with the lowest objective function value as the starting point for the following iteration. This way, the algorithm gradually approaches the objective function's minimum. The identified optimal tip trajectory is then used as a reference trajectory for the on-line deflection control algorithm operating during insertion.

7.1.2 On-line Tip Trajectory Adjustment

During insertion, the lateral force applied to the needle is adjusted based on the error between the pre-planned needle tip trajectory and the measured needle tip deflection. To predict the lateral force required to bring the needle tip from its current deflection to a desired deflection, an inverse deflection model is needed that returns the lateral force based on a desired needle deflection. In the following, such a model is derived from the deflection model introduced in Section 6.2. The model is based on the linear system of equations

$$\Phi(z)\mathbf{g}(d) = \Gamma + F_t\mathbf{1}_{n\times 1} + \Omega(z) \tag{7.3}$$

with

$$\Phi = \begin{bmatrix} \phi_{11} & \cdots & \phi_{1n} \\ \vdots & \ddots & \vdots \\ \phi_{n1} & \cdots & \phi_{nn} \end{bmatrix};\ \Gamma = F_l \begin{bmatrix} q_1(c_2) \\ \vdots \\ q_n(c_2) \end{bmatrix};\ \Omega = \begin{bmatrix} \omega_1 \\ \vdots \\ \omega_n \end{bmatrix};\ \mathbf{g} = \begin{bmatrix} g_1 \\ \vdots \\ g_n \end{bmatrix}$$

as derived in Section 6.2.2.

Provided that the needle tip deflection u_t is known through measurement and F_l is considered to be unknown, Γ is moved to the right-hand side and merged into Φ. The new system of equations is then

$$\underbrace{\begin{bmatrix} \Phi & -\mathbf{q}(c_2) \\ \mathbf{1}_{1\times n} & 0 \end{bmatrix}}_{\Phi^\dagger} \underbrace{\begin{bmatrix} \mathbf{g} \\ F_l \end{bmatrix}}_{\mathbf{g}^\dagger} = \underbrace{\begin{bmatrix} \Omega \\ 0 \end{bmatrix}}_{\Omega^\dagger} + \begin{bmatrix} F_t\mathbf{1}_{n\times 1} \\ 0 \end{bmatrix} + \underbrace{\begin{bmatrix} \mathbf{0}_{n\times 1} \\ u_t \end{bmatrix}}_{\Lambda} \tag{7.4}$$

where $\mathbf{q}(c_2) = [q_1(c_2), \ldots, q_j(c_2), \ldots, q_n(c_2)]^T$. Finally, (7.4) is solved for $\mathbf{g}^\dagger$ as

$$\mathbf{g}^\dagger = \Phi^{\dagger -1}\left(\Omega^\dagger + F_t\mathbf{1}_{n\times 1} + \Lambda\right) \tag{7.5}$$

and the lateral force is $F_l = g^\dagger_{n+1}$.

With (7.5), we can predict F_l for given parameters K, F_t, and desired (pre-planned) $u_t(d)$. The advantage of this method of direct calculation of the lateral force F_l is that no time consuming iterative search is needed, which is crucial given sample time constraints during real-time trajectory re-planning.

During insertion, multiple criteria are enforced at the satisfaction of any of which the lateral force is removed. Their purpose is to detect whether the influence of the lateral force on needle deflection has declined to a degree where the steering effect is no longer given, to prevent instability of the lateral actuator and to prevent application of excessive force. The criteria are that a maximal force limit $F_{l,\max}$ is exceeded, the limit for a change in lateral force between samples ΔF_l is exceeded and $d > d_{l,2}$. If any of these criteria is met, the lateral actuator's reference force is set to zero.

7.2 Experimental Study

To assess the steering accuracy of the proposed needle steering method, an experimental needle insertion study is carried out. The setup used for the experiments is described in Section 2.2. The distance between the fixed needle guide and tissue is set to 36 mm. A standard brachytherapy needle (Type RP-1100-1820, Riverpoint Medical, Portland, OR, USA) is inserted into phantom tissue made from Plastisol (Type Super Soft Plastic, M-F Manufacturing Co., Inc, Fort Worth, TX, USA). To parameterize the deflection and force models, the tissue Young's modulus K and needle tip force F_t need to be identified. To measure the tissue Young's modulus, the indentation method described in Section 8.4.2 is used. The identified Young's modulus K of the phantom tissue is 12.16±2.5 kPa.

To identify the tip force, six insertions are carried out to a final depth of 140 mm without applying lateral force. The tip force F_t is then quantified using the method introduced in Section 6.3.1. The identified tip force is 0.25 N. With the deflection model now parameterized, the optimal needle trajectory can be determined using the method described in Section 7.1.1. The identified parameter values of the constant lateral force $F_{l,c}$ and the force's application depth $d_{l,1}$ with which the optimal trajectory is achieved are -2.98 N and 10.5 mm, respectively.

During the insertions, the needle is steered in real time through the application of lateral actuation only and using the algorithm introduced in Section 7.1.2. Six insertions are carried out into the Plastisol tissue sample while a lateral force is applied that steers the needle to the pre-planned target. The experimental results are plotted in Figure 7.2. The measured needle tip trajectories of the six insertions where lateral actuation is used are plotted in Figure 7.2a. To assess the steering accuracy and amount of deflection reduction, the pre-planned tip trajectory and a tip trajectory without lateral actuation are plotted. The maximum error between the measured and pre-planned needle tip deflection is approximately 2 mm at the final insertion depth. A substantial reduction of needle deflection of approximately 80% can be observed when the needle is steered using lateral actuation. To provide an assessment of the amount of residual needle deflection at the final insertion depth, the measured needle deflection at the final insertion depth for all 6 steered insertions and one non-steered insertion

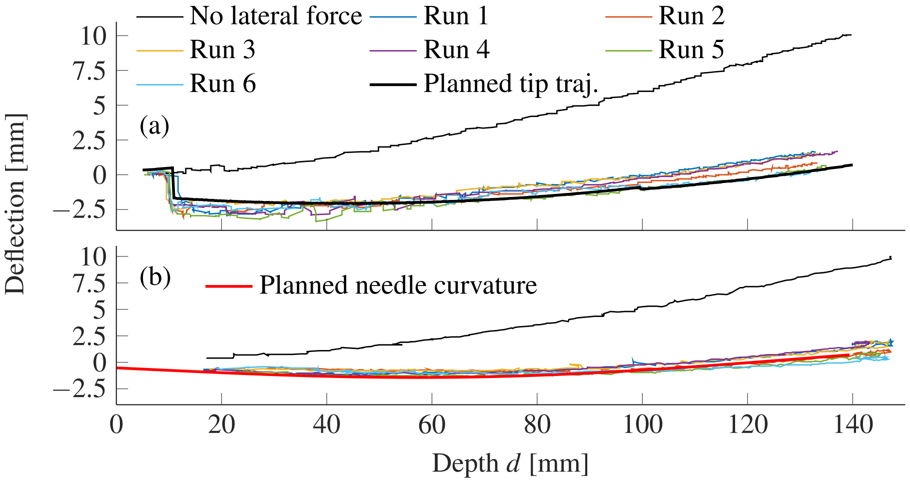

Figure 7.2: (a) The planned and measured needle tip trajectories and (b) the measured needle shape at the final insertion depth (140 mm) for all six insertion trials. The needle tip trajectories in (a) are measured during insertion as the ultrasound probe tracks the tip. The shapes in (b) are measured after the final insertion depth has been reached and insertion is stopped. The method for translating the ultrasound probe to measure the needle shape at the final insertion depth is described in Section 2.3.

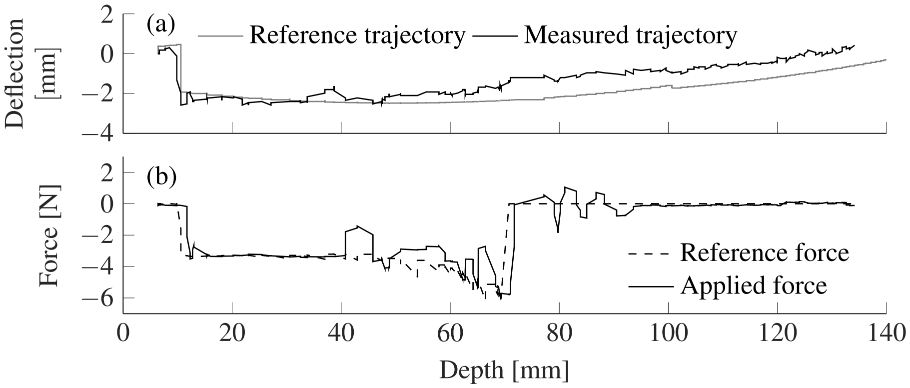

Figure 7.3: (a) The reference and measured needle tip trajectory during Run 6 and (b) the model-predicted and applied lateral force.

is plotted in Figure 7.2b. The plots show that the deflection remains below approximately 2 mm throughout the entire needle length.

In Figure 7.3a, the pre-planned and measured tip trajectory of Run 6 are plotted and in Figure 7.3b, the corresponding reference and applied lateral force are plotted. In Figure 7.3b it can be observed that the lateral force is removed at a depth of roughly 70 mm. The reference force is set to zero when one of the above-mentioned criteria is met, which in this case are $F_{l,\max} = 8$ N, $\Delta F_l = 4$ N and $d_l = 100$ mm.

7.3 Discussion

A significant reduction of needle deflection can be achieved while only using lateral actuation as steering input as described in Section 7.2. This partially confirms the findings presented in Section 6.5 where simulations indicate that a lateral force applied continuously from a shallow insertion depth onward can entirely eliminate needle deflection. The experimental results also show that a significant amount of needle deflection remains (see Figure 7.2b) that the online algorithm for needle adjustment can not account for. This error could be further corrected by adjusting the model parameters tissue Young's modulus K and tip force F_t in an intelligent manner based on the error between predicted and measured deflection.

Furthermore, Figure 7.3b shows that the absolute maximum lateral force magnitude predicted on-line by the model and thus applied during the experiments is at 6 N much higher than the pre-planned absolute constant force of 2.98 N. In a clinical scenario, forces of such magnitude could exceed a limit that would prevent trauma to the patient. Given this limitation potentially imposed on lateral actuation, the steering objective might not be reachable entirely. To mitigate this issue, axial needle rotation would need to be used additionally to lateral actuation to reach the target with better accuracy. This limitation suggests that lateral actuation alone as control input is not enough to completely eliminate needle deflection and therefore a combination of lateral actuation and axial rotation should be used.

7.4 Concluding Remarks

This chapter proposes a method for needle steering using only lateral needle actuation as steering input. It is shown experimentally that the steering method can achieve a good performance for a steering objective that is pertinent to the efficient placement of seeds during prostate brachytherapy. It is also experimentally shown that it is possible to almost entirely eliminate needle deflection at the final insertion depth when applying only lateral needle actuation as steering input. However, limitations with respect to the reachability of a target potentially exist when the lateral force must be limited during a clinical scenario to avoid inflicting trauma to the patient. Thus a combination of intermittent axial rotation and lateral actuation should be considered.

Chapter 8

Intraoperative Tissue Young's Modulus Identification Using Lateral Needle Actuation

8.1 Introduction

Most of the mechanics-based (physical) models for needle deflection found in the literature [29, 20, 21, 30, 34, 32, 26, 33, 35] require the tissue's Young's modulus to model tissue compression occurring due to the deflecting needle shaft during insertion.

The tissue Young's modulus can be difficult to obtain in a clinical setting prior to or during the surgical procedure due to a lack of equipment, limited access, or interference with standard surgical routines for each procedure. Common methods to quantify the Young's modulus of biological tissue are palpation [98, 99], compression tests, and ultrasound elastography (e.g., shear wave measurement based on the Acoustic Radiation Force Impulse (ARFI) imaging technique) [100, 101, 102]. While these methods are capable of accurately quantifying tissue Young's modulus, they are not always or widely available during or even prior to a prostate brachytherapy intervention. Some of the past research proposes that initially one or multiple insertions are done without needle steering in order to obtain needle deflection measurements that can then be used to identify the tissue Young's modulus, enabling model-based steering of the needles in future insertions [23, 35].

This chapter proposes a novel method for identifying tissue Young's modulus using a needle that is being inserted into tissue, provided the needle can also be laterally displaced outside of tissue by the actuated needle guide. A schematic representation of the needle with lateral displacement applied by the actuated guide is shown in Figure 8.1. The needle, which is fixed in terms of lateral motion and rotation by a fixed needle guide (i.e., the fixed guide template), is inserted into tissue up to a depth d_K and then laterally displaced by the actuated needle guide. The resulting deflection causes the tissue surrounding the needle to

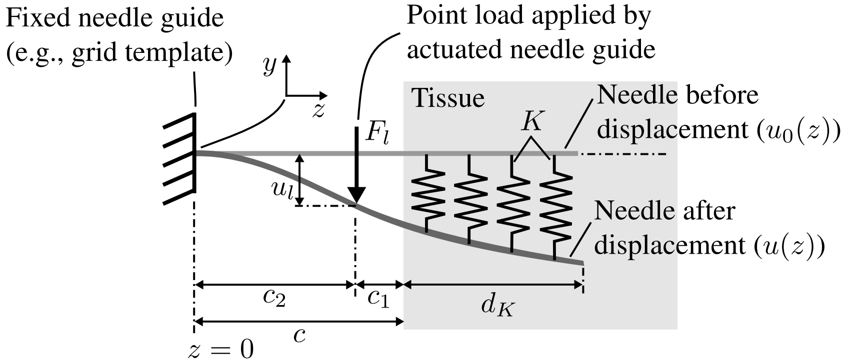

Figure 8.1: A schematic representation of the needle inside tissue with a lateral point load F_l applied onto the needle at point c_2.

be deformed. The mechanical work of the actuated guide and the needle deflection shape can be measured using a force/torque sensor and an ultrasound (US) probe, respectively. The needle-tissue system is governed by the conservation of energy principle, which states that the work applied to a system must equal its potential energy in steady state. With the force applied by the actuated guide to the needle-tissue system (F_l) and the needle deflection shape known, the tissue Young's modulus K can be determined. The identified tissue Young's modulus can then be used in mechanics-based needle deflection models.

This approach provides a direct method for Young's modulus identification as the needle itself is the tool used to displace the tissue and measure the response. The method can be used intraoperatively where the needle insertion will only need to be paused briefly at a shallow depth to obtain the tissue Young's modulus, meaning that there will not be much interference with the current prostate brachytherapy procedure. Therefore, the method does not increase the needle insertion time or degree of invasiveness noticeably. This additional application of lateral needle actuation facilitates automatic model-based needle steering in that system parameters can be automatically obtained without the need for additional equipment. Thus, the presented method for Young's modulus identification is an important step towards the development of an assistant system that is able to steer the needle in an integrated and intelligent manner.

Lastly, as Rossa *et al.* [35] have shown before, the availability of the tissue Young's modulus can facilitate non-image-based needle deflection prediction and steering in the sense that the US transducer can be used by the surgeon for visualization and monitoring purposes and does not have to be tied to the robotic system for the entire procedure. In this chapter, the proposed method for Young's modulus identification is used to parameterize the model introduced by Rossa *et al.* [35]. The objective is to show the feasibility of the integrated Young's modulus identification method with regards to clinical implementation in robot-assisted needle insertion.

The remaining sections of this chapter are organized as follows. The proposed method for tissue Young's modulus identification is presented in Section 8.2. In Section 8.3, the integration of the method with model-based prediction of needle deflection is presented. The experimental validation of the method follows in Section 8.4.3. An experimental assessment of the tissue parameter identification method's integration with needle steering is provided in Section 8.4.4. In Section 8.5, the experimental results and limitations of the proposed method are discussed. Finally, in Section 8.6, concluding remarks and an outlook on remaining future work are provided.

8.2 Tissue Young's Modulus Identification

A schematic representation of the proposed method for Young's modulus identification is shown in Figure 8.1. The needle is inserted into tissue to a depth d_K. It is then laterally displaced by the actuated needle guide. This causes the needle shaft to deflect, which in turn displaces and deforms the tissue surrounding the needle. The tissue is modelled as linearly elastic springs where the spring stiffness is the stiffness of the tissue per unit length squared. The needle, which is constrained by the fixed needle guide at one end, is modelled as a cantilever beam where the needle deflection and its slope are zero at $z = 0$ (see Figure 8.1). In order to obtain the tissue Young's modulus K, the principle of conservation of energy is applied, which states that the work that is applied to a system must equal the potential energy that is stored in the system in equilibrium. The work in this case is applied by the actuated needle guide and is related to the measurements of a force/torque sensor that measures F_l, which is correlated to the needle deflection $u(z)$ relative to the needle deflection shape before F_l was applied (assumed to be zero). As discussed later, the needle deflection shape inside tissue can be measured through ultrasound images. The needle deflection shape outside tissue can be measured through a camera or other sensing systems or estimated through an interpolation between the fixed needle guide and the tissue entry point, whose positions are known and act as boundary conditions. The estimated deflection shape of the complete needle is then obtained by piece-wise polynomial fitting and interpolation.

In the following, the energy and work terms that represent the needle-tissue system's configuration while a lateral displacement is applied to the needle are introduced. At equilibrium, we have

$$U_s(u) + U_d(u) - V_l = 0 \tag{8.1}$$

where $U_s(u)$ is the strain energy stored in the bent needle, $U_d(u)$ is the energy stored in the displaced tissue and V_l is the work applied by the actuated needle guide.

Strain Energy Stored in the Needle U_s

When the needle is deflected by the actuated needle guide to $u(z = c_2)$, strain energy is stored in the needle which can be formulated as

$$U_s(u) = \frac{EI}{2} \int_0^l u''(z)^2 \, dz \tag{8.2}$$

where l is the needle length, E and I are the needle Young's modulus and area moment of inertia, respectively, $u(z)$ is the needle deflection shape for $z \in (0, l)$, and $(\cdot)''$ is the second derivative with respect to z.

Energy Stored in Tissue U_d

The tissue is modelled as a set of linear elastic virtual springs where the spring stiffness K is the tissue's Young's modulus as expressed in force per unit area. The energy stored in the displaced tissue is

$$U_d(u) = \frac{K}{2} \int_{l-d_K}^{l} \left(u(z) - u_0(z)\right)^2 \, dz. \tag{8.3}$$

where $u_0(z)$ is the deflection shape before the lateral displacement is applied to the needle. Since the lateral displacement can be applied in the perpendicular direction to the plane of needle deflection, the deflection shape $u_0(z)$ during the Young's modulus identification phase can be assumed to be zero.

Work Done by the Actuated Needle Guide V_l

When the actuated needle guide displaces the needle, its displacement at position $z = c_2$ and the lateral force F_l have reached steady state (i.e., are constants) such that the work done by the actuated needle guide can be simply expressed as

$$V_l = F_l u(c_2) \tag{8.4}$$

where $u(c_2)$ is the lateral needle displacement caused by the actuated guide and F_l is the lateral point load enacted onto the needle at $z = c_2$ that caused this displacement.

Inserting (8.2), (8.3), and (8.4) into (8.1) gives

$$EI \int_0^l u''(z)^2 \, dz + K \int_{l-d_K}^l u(z)^2 \, dz - 2F_l u(c_2) = 0. \tag{8.5}$$

Through a trivial re-formulation of (8.5), the tissue Young's modulus K can now be obtained as

$$K = \frac{2F_l u(c_2) - EI \int_0^l u''(z)^2 \, dz}{\int_{l-d_K}^l u(z)^2 \, dz}. \tag{8.6}$$

In order to calculate K, the two variables F_l and u_l, and a closed form for $u(z)$ need to be available. F_l is quantified using a force sensor attached to the actuated needle guide and $u(c_2)$ can be obtained from the actuated needle guide. A labelled depiction of the linear actuation unit including force sensor and actuated needle guide are shown in Figure 2.2. The final component in (8.6) that needs to be found is the needle deflection shape $u(z)$ or a closed-form function representation thereof. A suitable representation of $u(z)$ is the piece-wise polynomial function

$$\hat{u}(z) = \begin{cases} \hat{u}_1(z) & \text{for } z \in (0, c] \\ \hat{u}_2(z) & \text{for } z \in (c, l) \end{cases} \tag{8.7}$$

where c is shown in Figure 8.1, $\hat{u}_1(z)$ for $z \in (0, c]$ is a polynomial interpolation of the needle deflection shape outside tissue, and $\hat{u}_2(z)$ for $z \in (c, l)$ is a polynomial fit of the needle deflection shape inside tissue.

It was found that a third-order polynomial for $\hat{u}_1(z)$ and a second-order polynomial for $\hat{u}_2(z)$ are appropriate, which will be the basis of the rest of the discussion in this section, although higher-order polynomials may be considered for other scenarios. Then, a linear least squares solver is used to fit the second-order polynomial to sampled needle deflection shape measurements. Limiting the polynomial order to two is necessary to prevent overfitting. The needle deflection shape data is obtained using ultrasound imaging. In order to parameterize $\hat{u}_1(z)$, the four polynomial coefficients $\mathbf{a} = [a_3 \ a_2 \ a_1 \ a_0]^T$ are calculated analytically by using the four known boundary conditions $\hat{u}_1(0) = 0$, $\hat{u}_1'(0) = 0$, $\hat{u}_1(c) = \hat{u}_2(c)$ and $\hat{u}_1'(c) = \hat{u}_2'(c)$ where $(\cdot)'$ is the first derivative with respect to z. To calculate $\mathbf{a}$, the linear system of equations

$$\begin{bmatrix} 0 & 0 & 0 & 1 \\ 0 & 0 & 1 & 0 \\ c^3 & c^2 & c & 0 \\ 3c^2 & 2c & 1 & 0 \end{bmatrix} \begin{bmatrix} a_3 \\ a_2 \\ a_1 \\ a_0 \end{bmatrix} = \begin{bmatrix} 0 \\ 0 \\ \hat{u}_2(c) \\ \hat{u}_2'(c) \end{bmatrix} \tag{8.8}$$

is solved.

At this point, $\hat{u}(z)$ is identified and can be inserted into (8.6) in order to obtain the tissue Young's modulus K.

8.3 Integration with Prediction of Needle Deflection

This section presents the integration of the proposed tissue Young's modulus intraoperative identification method with an existing needle deflection model for the prediction of needle deflection. The deflection modelling is based on the method proposed by Rossa *et al.* [35]; it should be noted that any other deflection model that is designed based on the mechanics of needle-tissue interaction, and thus in need of the knowledge of tissue Young's modulus, can be combined with the proposed method. The integration does not require modifications to the needle deflection model introduced in [35], which makes the proposed research appealing from a practical perspective.

Figure 8.2 illustrates the integration of the Young's modulus estimation with the needle insertion procedure. The block diagram shown consists of three components, namely the

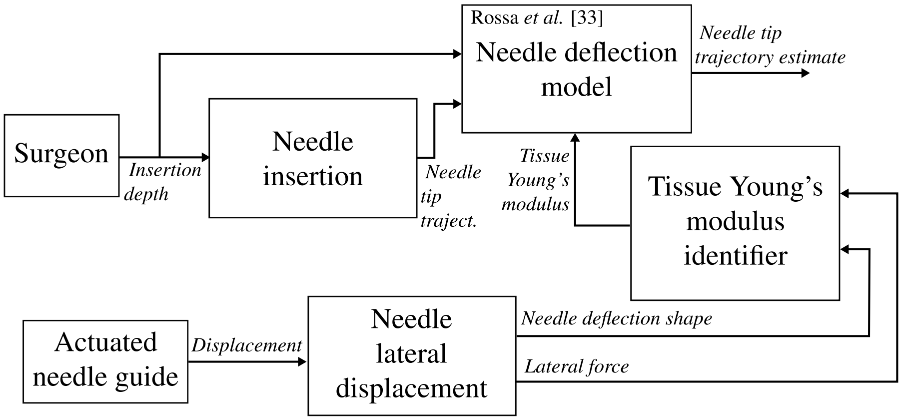

Figure 8.2: A block diagram representing the integration of the proposed method for needle-tissue model parameter identification with the prediction of needle deflection.

actuated needle, the intraoperative tissue Young's modulus identification, and the needle deflection model.

The needle can be actuated by two different means: insertion and lateral displacement (enacted by the actuated needle guide). The former directly influences the needle deflection shape, which can be measured during insertion using ultrasound (US) imaging.

Figure 8.3 depicts a schematic representing the chronological succession of three steps towards predicting needle deflection; 1) identifying tissue Young's modulus K, 2) identifying the needle tip load F_t and 3) predicting needle deflection.

1) Identification of tissue Young's modulus K

When the insertion depth d_K is reached, the needle insertion is paused and the needle is laterally displaced by the actuated needle guide. The needle deflection shape inside tissue $u(z)$ is then measured using transverse ultrasound images. A force sensor attached to the actuated needle guide measures the lateral force F_l applied by the guide to the needle. Subsequently, the tissue Young's modulus K is identified based on the aforementioned measurements $u(z)$ and F_l.

2) Identification of needle tip load F_t

After the lateral needle displacement is removed, the needle is further inserted up to depth d_s while the needle tip trajectory $u_t(d)$ is recorded using transverse ultrasound images. The

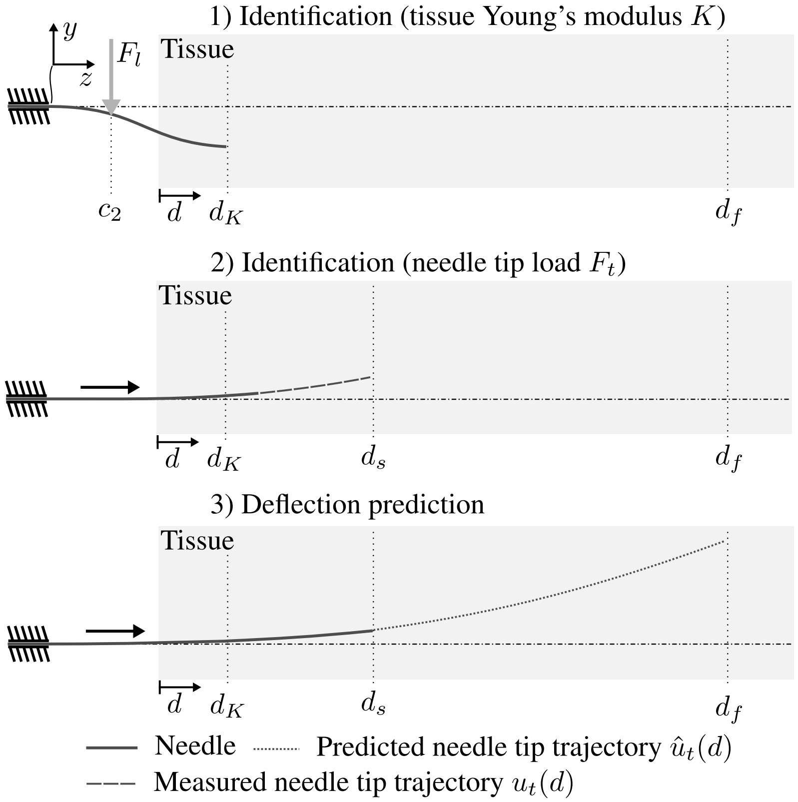
1) Identification (tissue Young's modulus K)

2) Identification (needle tip load F_t)

3) Deflection prediction

Figure 8.3: The three phases of one needle insertion. d_K is the insertion depth at which the tissue Young's modulus K is identified, d_s is the insertion depth up to which the needle deflection is measured for identification of the tip load F_t and d_f is the final insertion depth.

tip load F_t can then be identified using a modified version of the deflection model that takes as input $u_t(d)$ and the previously identified K.

3) Prediction

In the third step, both K and F_t are supplied to the needle deflection model in order to predict the needle deflection beyond depth d_s.

8.3.1 Needle Deflection Model

To model the needle deflection during insertion, the model introduced by Rossa *et al.* [35] is used. A schematic representation of the modelled needle-tissue interactions is illustrated in Figure 8.4. It shows tissue compression along the needle modelled as a sequence of linear elastic springs with stiffness K and the needle tip cutting of tissue as a transverse

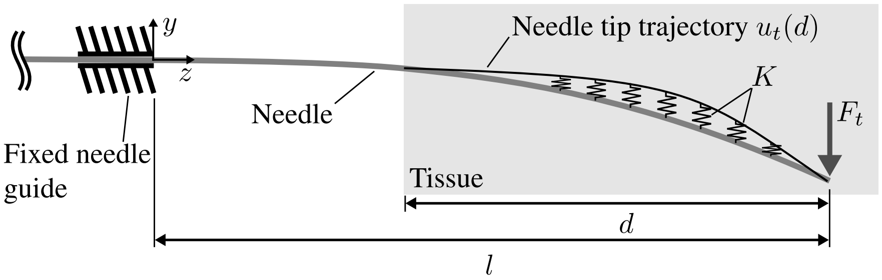

Figure 8.4: A schematic of the modelled needle-tissue interactions as a sequence of linear elastic springs modelling tissue displacement and a point load at the needle tip modelling the tip cutting tissue.

point load F_t. The deflection model is based on an energy-based formulation of the needle-tissue interactions that consists of the sum of the energy stored in the system and the work exerted to the needle-tissue system. The model is similar to the one introduced in Section 6.2 except that the work V_l applied by the lateral needle guide does not exist in Rossa *et al.*'s formulation of the needle-tissue interactions.

8.3.2 Needle Tip Force Identification

The second parameter required by the deflection model is a cutting-related force at the needle tip F_t, which is the primary cause for needle deflection. As the needle is inserted, the bevelled needle tip cuts, displaces and therefore compresses tissue asymmetrically. The one-sided tissue compression causes the needle to deflect in the direction of the bevel. The force F_t is assumed to be constant throughout insertion. Generally, due to the needle deflection slope, the relation between the needle tip load as expressed in the needle tip frame is $F_t' = F_t \cos(\theta)$ where θ is the needle tip deflection slope. Since, however, θ is small ($< 15°$), it can be assumed that $\cos(\theta) \sim 1$. To identify F_t, the *tip force* introduced in Section 6.3.1 is used. The re-formulated model takes as input the needle tip deflection $u_t(z)$ and the parameter tissue Young's modulus K. Needle tip deflection data is obtained as the needle is inserted during the identification step introduced in Section 8.3.

To estimate the tip force that is to be supplied to the deflection model, the tip force samples calculated from the model using measured needle tip deflection samples at insertion depths d_K to d_s are averaged.

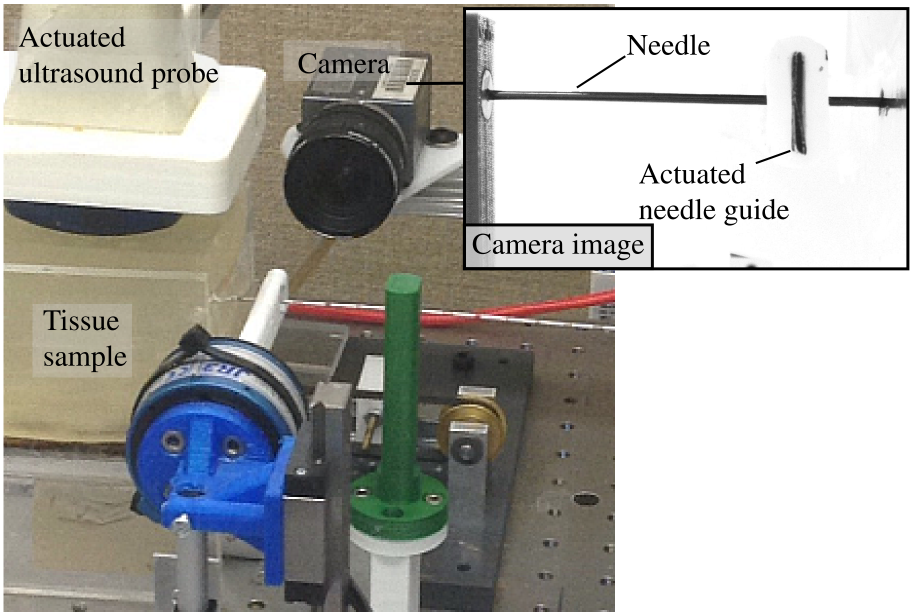

Figure 8.5: The setup for lateral actuation with a camera mounted to observe the position of the actuated needle guide.

8.4 Experimental Studies

In this section, two experimental studies are presented. In the first study, the concept proposed in Section 8.2 for tissue Young's modulus identification is validated and in the second study, the feasibility for incorporation with deflection modelling and prediction is presented.

8.4.1 Experimental Needle Insertion Setup

The experimental setup introduced in Section 2.2 is used for both experimental studies. A camera (Model XCD-SX90CR, Sony Corporation, Tokyo, Japan) captures image sequences from the right side of the needle (see Figure 8.5). The camera image sequences are used to accurately measure the vertical displacement of the actuated needle guide during each experimental trial and thus the needle deflection $u(c_2)$. A basic template matching routine that tracks the location of the actuated guide within an image sequence measures the vertical displacement. The pixel to millimetre conversion ratio for camera images is 0.051 millimetres per pixel. The displacement of the actuated needle guide is obtained through camera images due to the high positional accuracy needed for obtaining the mechanical work V_l (see (8.4)) induced by the actuated needle guide. The linear actuators provide an accuracy of ± 0.3 mm.

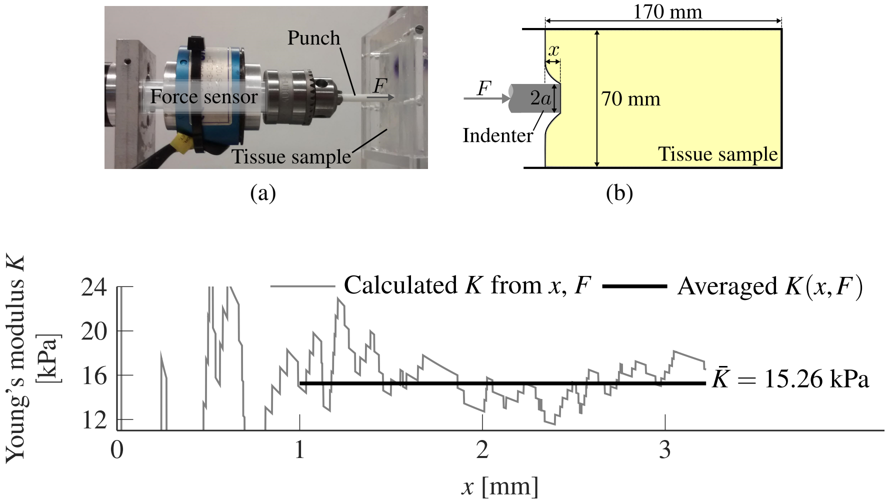

(a) (b)

(c)

Figure 8.6: (a) The experimental setup for the indentation test and (b) a schematic showing the tissue indentation and assigned dimensional labels where $a = 2.1$ mm is the radius of the indenter and F is the force resulting in the indentation depth x. (c) The result of one indentation test run.

8.4.2 Tissue Indentation Experiments

In Section 8.4.3 and Section 8.4.4, two phantom tissue samples with different Young's moduli are used. Both samples are made from Plastisol (Type Super Soft Plastic, M-F Manufacturing Co., Inc, Fort Worth, TX, USA) where plastic softener is used to adjust the tissue stiffness and thus its Young's modulus. In order to establish a ground truth for the two tissue samples' Young's moduli, an independent measurement is needed. The applied method is a tissue indentation test where a blunt cylindrical punch indents the tissue to a defined depth while the indentation force is measured. The indentation setup is shown in Figure 8.6a. During an indentation experiment, the indenter is advanced with a constant velocity of 1 mm/s up to a depth $x_f = 3.5$ mm. The Young's modulus is then calculated with the relation [98]

$$K = \frac{(1-\nu^2)F}{2ax\kappa} \tag{8.9}$$

where x and F are the indentation depth and force, respectively, a is the indenter radius, ν is Poisson's ratio and κ represents a constant, which is unity for a semi-infinite body (see Figure 8.6b). The tissue is assumed linearly elastic, homogeneous and incompressible.

Thus, Poisson's ratio ν is 0.5. As the dimensions of the tissue sample (width 70 mm and depth 170 mm) are large with respect to the indenter and a maximum indentation depth of $x_f = $ 3.5 mm, it is presumed that semi-infinite conditions apply. A sample plot for tissue sample one that plots the Young's modulus K against the indentation depth x is shown in Figure 8.6c. Six runs of the above described experiment are carried out and $\bar{K}$, the averaged K is calculated for each run. Finally, the mean of each run's $\bar{K}$ is taken to obtain the final value for the tissue Young's modulus K_{REF}. The measured K_{REF} is 16.23±2.73 kPa for tissue sample 1, and for tissue sample 2 it is 12.61±2.63 kPa.

8.4.3 Validation of Young's Modulus Identification

Three experimental trials are carried out where the three insertion depths d_K of 20 mm, 30 mm and 40 mm are considered for trial one, two and tree, respectively. For each trial, six runs were performed. Relatively shallow insertion depths are chosen since it is desired to carry out this identification routine early on during insertion. A parameterized needle deflection model will then be available for needle steering algorithms earlier during insertion. Multiple trials with varying insertion depth are selected to show the robustness of the proposed method to different insertion depths. A rather small lateral needle displacement of 1.2 mm at $z = c_2$ is chosen to comply with the assumption that the tissue is linearly elastic.

The needle used for the experiments is a standard 18G brachytherapy needle (Type RP-1100-1820, Riverpoint Medical, Portland, OR, USA), which has a Young's modulus of $E =$200 GPa, an outer radius of 0.635 mm, an inner radius of 0.5 mm, and a bevel angle of 20°. The needle is inserted into tissue sample 1 through the fixed and actuated needle guides as shown in Figure 2.2. Each experimental run is carried out in the following sequence:

1) Displace needle vertically at $z = c_2$ by -1.2 mm using actuated needle guide and hold displacement.

2) Move actuated US transducer from needle entry point ($z = c$) to needle tip ($z = l$) at velocity 1 mm/s to obtain an image sequence of needle cross-sections at varying depth.

3) Remove vertical needle displacement once the US transducer reaches the needle tip.

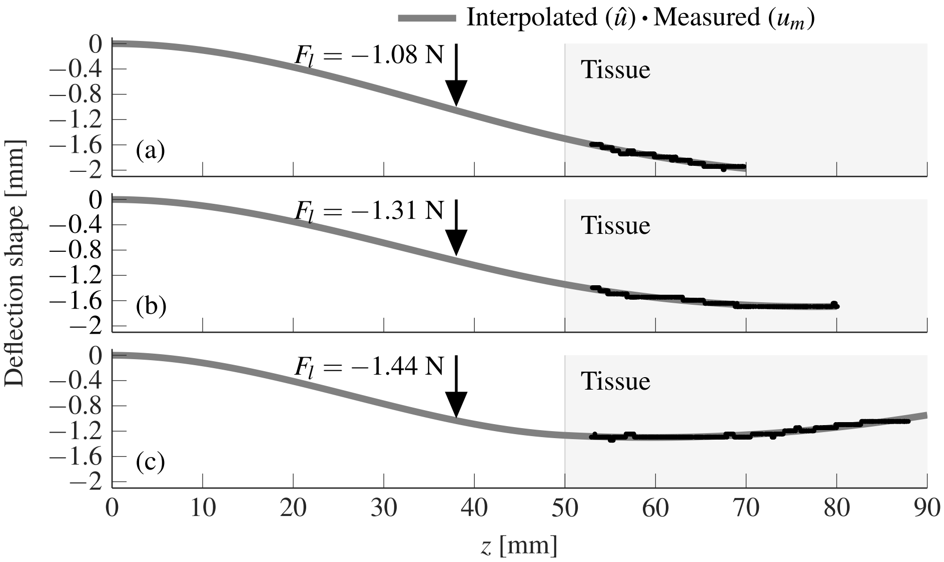

Figure 8.7: The measured needle deflection shape inside tissue and estimated deflection shape for insertion depths (a) $d = 20$ mm, (b) $d = 30$ mm and (c) $d = 40$ mm.

Table 8.1: Results of the tissue Young's modulus identification. K_{ID} is the mean of the identified Young's modulus over 6 experimental runs and σ is the standard deviation. h is the test decision of a two-sample t-test indicating whether the difference between K_{REF} and K_{ID} is significantly different (r) or not ($\bar{r}$).

Insertion depth d_K [mm]	K_{ID} [kPa]	σ	$\lvert K_{REF} - K_{ID}\rvert$ [kPa]	t-test	
				h	p-value
20	16.53	2.63	0.3	$\bar{r}$	0.85
30	14	2.62	2.23	$\bar{r}$	0.18
40	13.94	3.15	2.29	$\bar{r}$	0.21

Figure 8.7 shows the measured needle deflection shape inside tissue (u_m) with applied lateral force F_l at $z = c_2$ and the interpolated deflection shape $\hat{u}(z)$ determined using the method described in Section 8.2. The measured deflection shape's noise is very low and the error is essentially limited to the pixel quantization error of the ultrasound images (0.05 mm). This results in a good quality of fit with a residual sum of squares (RSS) of 0.14 mm^2 for Figure 8.7a, 0.18 mm^2 for Figure 8.7b, and 0.29 mm^2 for Figure 8.7c. The RSS for all other runs is of the same magnitude.

To identify the tissue Young's modulus K, the interpolated needle deflection shape $\hat{u}(z)$, the applied lateral force F_l, and the measured needle deflection $u(c_2)$ are inserted into (8.6). The resulting estimate for the Young's modulus K_{ID} is given in Table 8.1 as an average over

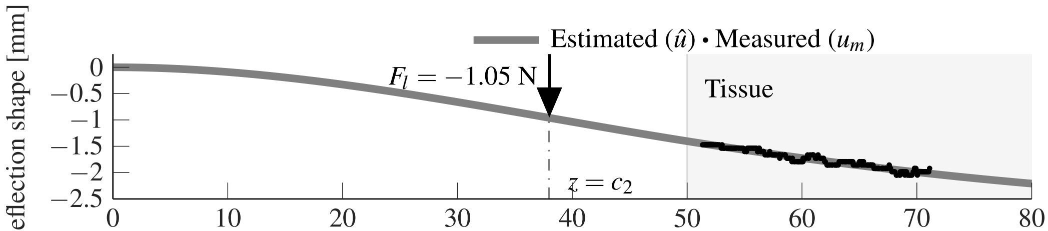

Figure 8.8: The measured needle deflection shape inside tissue and predicted deflection shape for insertion depth $d = 30$ mm (20 mm measured) and tissue sample 2.

the six runs. The standard deviation σ ranges from approximately 16% to 23% of K_{ID}. The absolute error between the Young's modulus ground truth K_{REF} and the estimated K_{ID} is lowest for insertion depth $d_K = 20$ mm with 0.3 kPa and highest for $d_K = 40$ mm with 2.29 kPa. A two-sample t-test decision h, which determines whether K_{ID} and K_{REF} are significantly different and the test's p-value show that for none of the trials, K_{ID} and K_{REF} are significantly different at a significance level of 5%.

8.4.4 Prediction of Needle Deflection

The prediction performance of the deflection model re-introduced in Section 8.3.1 is evaluated when the deflection model is calibrated using the proposed method for Young's modulus identification. For this study, tissue sample 2 is used.

The sequence of steps described in Section 8.3 is followed towards predicting needle deflection. First, the tissue Young's modulus of tissue 2 is identified using the proposed method. Figure 8.8 shows the measured needle deflection shape inside tissue and the resulting deflection shape prediction. The identified tissue Young's modulus is $K_{ID} = 10.36$ kPa.

For evaluating the final two steps that are needle tip force identification and deflection prediction, six insertions are carried out to a final insertion depth of $d_f = 140$ mm while tracking the needle tip deflection with the actuated US transducer. The insertion data is then used to identify F_t from insertion depth $d_K = 30$ mm to d_s.

After depth d_s is reached, the needle tip trajectory $\hat{u}(d)$ is predicted using the identified K_{ID} and F_t. It should be noted that F_t is dependent on K_{ID}. In Figure 8.9, sample needle tip trajectories, the identified F_t and tip trajectory prediction are plotted for two different depths

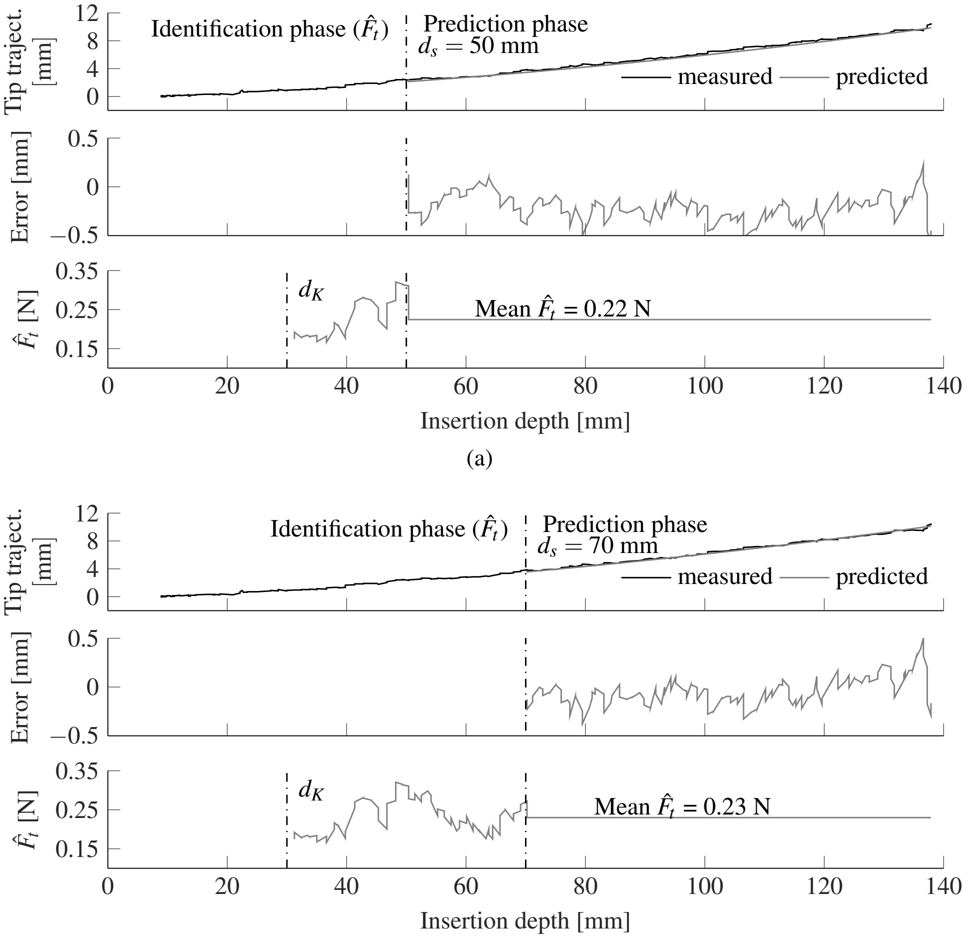

(a)

(b)

Figure 8.9: A sample insertion with a phase for identifying the tip force F_t and a phase for the prediction of the needle tip trajectory based on the tip force estimate $\hat{F}_t$ obtained during the identification phase. The switch from tip force identification to tip trajectory prediction was done at insertion depths (a) $d_s = 50$ mm and (b) $d_s = 70$ mm.

d_s. For both considered d_s, the error between the predicted and measured tip trajectory remains below 0.5 mm. A statistical comparison between the measured and predicted needle tip trajectory is provided in Table 8.2. The mean measured ($u_t(d)$) and predicted ($\hat{u}_t(d)$) needle tip deflections for $i = 1, \ldots, 6$ insertions and at four insertion depths are evaluated along with the mean absolute error (MAE $= \frac{1}{6}\sum_{i=1}^{6} |\hat{u}_{t,i}(d) - u_{t,i}(d)|$) and the respective standard deviations for all listed quantities. Results for both $d_s = 50$ mm and $d_s = 70$ mm are tabulated. The results show a larger MAE for the tip deflection prediction when the identification is stopped at $d_s = 50$ mm. Moreover, for $d_s = 70$ mm, the MAE remains

Table 8.2: The needle tip deflection prediction results where u_t and $\hat{u}_t$ are the measured and predicted needle tip deflection, respectively at insertion depth d. MAE is the mean of the absolute error $|\hat{u}_t - u_t|$. All listed quantities are expressed in millimetres.

Switching depth d_s	Insertion depth d	Mean $\hat{u}_t(d)$	Mean $u_t(d)$	MAE
50	80	4.13±0.49	4.58±0.21	0.48±0.26
	100	5.86±0.66	6.54±0.26	0.72±0.53
	120	7.80±0.93	8.62±0.28	1.02±0.59
	140	9.73±1.16	10.56±0.47	1.24±0.59
70	80	4.38±0.30	4.58±0.21	0.22±0.17
	100	6.24±0.37	6.54±0.26	0.32±0.30
	120	8.30±0.53	8.62±0.28	0.50±0.34
	140	10.36±0.66	10.56±0.47	0.73±0.40

below 1 for all listed insertion depths. This is not the case for $d_s = 50$ mm where the maximum MAE is 1.24 mm at insertion depth 140 mm.

8.5 Discussion

The results presented is Section 8.4.3 show that the tissue Young's modulus can be accurately identified with the proposed method for intraoperative tissue Young's modulus identification using a laterally actuated needle. The fact that the identification method can be applied reliably at varying insertion depths provides additional flexibility with respect to clinical application. With an estimate of the tissue Young's modulus being available early on during insertion, deflection models can potentially be calibrated earlier and a full prediction of deflection can be provided earlier during insertion, which is advantageous for needle steering.

The sources of error during the identification procedure are the US-based needle deflection shape measurement, the measurement of the lateral force F_l, and the measurement of the lateral displacement enacted by the actuated needle guide. The highest measurement error occurs during force measurement as the force sensor's dynamic range of 100 N is relatively high with respect to the measured force magnitude of approximately 1 N. When considering that the standard deviation is consistent for both Young's modulus identification and independent measurement, and that force is the only common measurement among the two methods, then the inaccuracy of the proposed method can be attributed to the force measurement. Therefore, the accuracy of the proposed method can be significantly increased with a more appropriate force sensor. Moreover, the standard deviation of approximately 16% is an indicator of a reliably identified Young's modulus.

The accuracy of the proposed method is on par with other state of the art approaches to identify the Young's modulus, such as indentation and ultrasound-based elastography under similar experimental conditions. Lu *et al.* [99] proposed a hand-held indentation system, where the difference between the ground truth and the identification via indentation probe was found to be 0.48 kPa with phantom tissue. Fu *et al.* [100] investigated the identification of tissue Young's modulus using B-scan ultrasound. The identified average Young's modulus was 10 kPa with a range of 9-12 kPa. The difference to the ground truth was 10.4%, or 1.04 kPa. In both above approaches, the ground truth was established using mechanical stress-strain tests. The proposed method shows an average difference between ground truth and identified Young's modulus of 1.61 kPa for the three considered needle insertion depths.

Experiments showed that the reliability of the proposed identification method is also highly dependent on the accuracy of the US-based needle deflection shape measurement. The quality of the needle shape fit inside tissue is dependent on the amount of noise present in the needle deflection shape measurement and therefore the calculated potential energy. A more robust method for estimating the needle deflection shape from noisy needle deflection shape measurements (e.g., considering beam-related models for needle deflection shape estimation) can be a focus of future work.

The prediction accuracy of the needle tip trajectory given in Section 8.4.4 is dependent on the depth d_s at which the switch to deflection prediction occurs. When the tip force F_t is identified up to a depth of 50 mm, the mean absolute error between measured and estimated needle tip trajectory exceeds 1 mm as opposed to when $d_s = 70$ mm where the MAE does not exceed 1 mm. The increased error for $d_s = 50$ mm can be attributed to the noise present in the needle tip deflection measurement that is reflected in $\hat{F}_t(d)$ for $d \in [d_K, d_s]$ (see Figure 8.9). When more samples of $\hat{F}_t$ are present (e.g., the distance d_K to d_s is larger), the mean of $\hat{F}_t$ for $d \in [d_K, d_s]$ gains in accuracy. Therefore, the predicted needle tip trajectory's accuracy could be significantly improved with a more accurate deflection measurement while the depth d_s can then be reduced. As illustrated in Section 8.3, the

Young's modulus identification using a laterally actuated needle is not time consuming with an estimated identification procedure duration of two to three seconds during which needle insertion needs to be paused. Thus, the method integrates well with clinical practice.

Biological pelvic tissues as well as any other region of the body are structured in layers from the perspective of the needle and therefore varying Young's moduli are expected at various insertion depths. The presented method of Young's modulus identification does not take this into account. In order to mitigate this limitation, the identification procedure could be carried out at multiple insertion depths where a change of tissue layers occurs. In the case of prostate brachytherapy, the identification procedure would have to be carried out twice during the first of roughly 20 insertions for the pre-prostate tissue layer and the prostate. The changing tissue stiffness among layers should then be to a certain extent reflected in the measured needle deflection resulting from lateral force application such that varying Young's moduli can be identified. Moreover, muscle tissue may present some directional dependence based on the muscle's parallel or perpendicular fibre alignment with the direction of lateral needle displacement. To explore the characteristics of biological tissue using the proposed method, the identification procedure may be carried out in multiple lateral directions to identify the fibre alignment of the muscle tissue.

8.6 Concluding Remarks

This chapter proposes an intraoperative method for the identification of tissue Young's modulus during needle insertion using a laterally actuated needle. Experimental evaluation shows a close match between the identified and independently measured tissue Young's modulus. Furthermore, the close integration with the deflection-model-based prediction of the needle tip trajectory is presented. The high accuracy of the predicted needle tip trajectory demonstrates the successful calibration of a deflection model found in the literature using the proposed method for Young's modulus identification.

Chapter 9

Conclusion

This thesis proposes and validates novel technologies for needle deflection sensing and needle actuation. The general objective for the development of these technologies is the facilitation of needle placement and deflection correction during insertion into soft tissue. The first part of the thesis is concerned with the development of a virtual sensor for needle deflection. The sensor, introduced in Chapter 3, estimates needle deflection during insertion using a proposed relation between needle-tissue interactions and measured force and torque at the needle base. The deflection sensor can provide real-time deflection estimation during needle insertion with a high sampling rate and could replace image-based deflection measurement. The only physical sensing device is a force/torque sensor attached to the needle base, making the method independent of explicit a-priori characterization of tissue properties. Shortcomings of previous but similar deflection estimation methods are addressed in the proposed approach such that the final version of the estimator maintains a high estimation accuracy up to an insertion depth of 140 mm, thus far exceeding the performance of previous deflection estimator iterations. Insertion experiments into various homogeneous phantom and non-homogeneous biological tissue samples confirm this. The estimation error is not statistically significant for any of the tested scenarios. While previous iterations of the sensor were only able to estimate the needle tip deflection, the final version introduced in Section 3.3 also estimates the needle deflection shape. Chapter 4 provides a possible application of the deflection estimator. A method for needle trajectory control and prediction is proposed whereby a kinematic bicycle model is parameterized and subsequently used to steer the needle to a desired target. It is experimentally validated that the introduced methodology can adequately predict the necessary rotation depth to steer the needle tip towards a pre-defined target and that the target is reached accurately.

In the second part of the thesis, a novel method of lateral needle actuation is introduced. A linear actuator applies a lateral point force to the needle near its entry point into tissue. The intended purpose of this actuation method is primarily needle steering and the potential for this purpose is investigated.

In Chapter 5, an initial experimental study investigates combining the two needle steering methods axial rotation and lateral actuation to minimize needle deflection at the final insertion depth. The experimental results indicate that when axial rotation is combined with lateral actuation, the needle deflection at the final insertion depth is significantly lower than when only one intermittent axial rotation is used for needle steering during insertion. The results also show that with lateral actuation, an almost entirely straight needle shape can be achieved, which is not possible without lateral actuation when the amount of needle rotations must be minimized to avoid tissue trauma.

To facilitate needle steering using a combination of axial rotation and lateral actuation, in Chapter 6, an energy-based model that predicts the deflection of a laterally actuated and axially rotated needle during insertion is subsequently developed. The model is capable of accounting for single-layer and multi-layer tissue with theoretically no limit on the amount of layers provided the thickness of each layer is known. The model's deflection estimation accuracy is validated experimentally under various lateral force, axial rotation, and tissue scenarios. The results confirm accurate deflection estimation. Using the validated deflection model, a sensitivity analysis is then conducted that investigates potentials and limitations of lateral force application and the possible impact of lateral actuation on needle deflection. The simulation results indicate that depending on the choice of the lateral force profile during insertion, lateral needle actuation alone can reduce needle deflection by as much as 90%. Moreover, a control simulation shows that a simple PID control law is not sufficient to effectively utilize lateral needle actuation, meaning that a more sophisticated control approach is needed to take full advantage of lateral actuation.

Subsequently, such a control approach is proposed wherein the use of lateral actuation for needle steering and trajectory adjustment is further investigated. In Chapter 7 a model-based steering approach is devised that steers the needle in real time based on a pre-planned trajectory which is optimized for needle placement as desired in prostate brachytherapy. The results of an experimental study provided show that the accuracy of the proposed steering method is within approximately 2 mm. Moreover, the experimental results show that the needle deflection can be reduced by 80% with only lateral actuation. Thus, the assertion previously obtained from simulation results is confirmed by these experimental results. The limitation of this steering method is, however, that in the case of force limitations imposed during a clinical scenario where excessive lateral forces should be avoided, the limited lateral force might not suffice to attain the desired needle placement. To mitigate this issue, axial needle rotation can be added as a second steering input.

A further proposed application for lateral needle actuation, which is described in Chapter 8, is an intraoperative method for the identification of tissue Young's modulus. The method is based on the fact that the amount of needle displacement caused by the application of a lateral force depends on the tissue stiffness. Validation experiments show that the identification accuracy of tissue Young's modulus for two different phantom tissue samples is on par with other methods of tissue Young's modulus identification. The proposed identification method is then applied to parameterize a deflection model. It is experimentally confirmed that an accurate deflection estimate can be obtained from the parameterized deflection model.

Throughout the second part of this thesis, it is shown that needle actuation can provide an alternative means of needle manipulation that can significantly improve needle steering when combined with axial rotation. In certain cases, lateral actuation can suffice to steer the needle to minimize needle deflection without the need for axial rotation. With the deflection model introduced in Chapter 6, the first step towards fully automatic, intelligent control of needle deflection using a combination of lateral actuation and axial rotation as needed has been provided. The second proposed application for lateral actuation extends the range of applications for the robotic assistant system and adds to its versatility. The system is able to identify necessary parameters for model-informed needle steering and deflection control. The presented control study that utilizes lateral actuation provides a promising initial step towards a model-based automatic deflection control approach.

9.1 Future Work

The deflection estimator could be further improved by investigating suitable needle-tissue interaction load basis functions through the development of FEM simulations of needle insertion. With more suitable basis functions, the tissue displacement could potentially be modelled better given the limited amount of force/torque measurements and thus limited amount of parameters available to adjust the load shape. Moreover, due to the limitation of Euler-Bernoulli beam theory to only remain accurate for small deflections, the use of nonlinear beam theory should be investigated. The needle steering approach introduced in Chapter 4 can also be further developed to identify the rotation depth for optimal needle placement online during insertion. This will greatly improve the steering approach's clinical relevance and applicability due to added autonomy of the robotic assistant system.

Furthermore, the limitations of the steering method introduced in Chapter 7 need to be addressed. Further development of model-based deflection controllers should enable them to decide automatically on appropriate control actions lateral actuation and axial rotation under constraints and limiting conditions such as a limit on the lateral force or a limited amount of axial rotations. An automatic needle deflection controller should be able to autonomously choose and leverage the required control action based on the needle steering target. Thus, the control method should be entirely autonomous with minimal input and decision making needed from the surgeon. To achieve this might also require the development of adaptive control methods that for instance correct deflection estimation errors through on-line model parameter re-tuning informed by needle deflection feedback.

Developed control methods should also be able to account for and choose appropriate control actions for a variety of steering targets including obstacle avoidance. For example, needle steering around the pubic arch during prostate brachytherapy is a common problem that could make prostate brachytherapy feasible for a wider range of patients that have previously not been considered for the procedure. Obstacle avoidance is of major importance for other applications of needle insertion. Investigating the potential of lateral actuation for other needle steering applications for which obstacle avoidance is a central concern such as biopsy can be an attractive future research direction in continuation of this thesis.

References

[1] T. Lehmann, C. Rossa, N. Usmani, R. Sloboda, and M. Tavakoli, “A virtual sensor for needle deflection estimation during soft-tissue needle insertion,” in *Proceedings of the 2015 IEEE International Conference on Robotics and Automation*, 2015, pp. 1217–1222.

[2] T. Lehmann, C. Rossa, N. Usmani, R. S. Sloboda, and M. Tavakoli, “A real-time estimator for needle deflection during insertion into soft tissue based on adaptive modeling of needle-tissue interactions,” *IEEE/ASME Transactions on Mechatronics*, vol. 21, no. 6, pp. 2601–2612, 2016.

[3] T. Lehmann, C. Rossa, R. Sloboda, N. Usmani, and M. Tavakoli, “Needle path control during insertion in soft tissue using a force-sensor-based deflection estimator,” in *Proceedings of the 2016 IEEE International Conference on Advanced Intelligent Mechatronics*, 2016, pp. 1174–1179.

[4] T. Lehmann, R. Sloboda, N. Usmani, and M. Tavakoli, “Human-machine collaboration modalities for semi-automated needle insertion into soft tissue,” *IEEE Robotics and Automation Letters*, vol. 3, no. 1, pp. 477–483, 2018.

[5] T. Lehmann, C. Rossa, N. Usmani, R. Sloboda, and M. Tavakoli, “Deflection modeling for a needle actuated by lateral force and axial rotation during insertion in soft phantom tissue,” *Mechatronics*, vol. 48, pp. 42 – 53, 2017.

[6] T. Lehmann, C. Rossa, N. Usmani, R. Sloboda, and M. Tavakoli, “Intraoperative tissue young’s modulus identification during needle insertion using a laterally actuated needle,” *IEEE Transactions on Instrumentation and Measurement*, vol. 67, no. 2, pp. 371–381, 2018.

[7] L. A. Torre, F. Bray, R. L. Siegel, J. Ferlay, J. Lortet-Tieulent, and A. Jemal, “Global cancer statistics, 2012,” *CA: A Cancer Journal for Clinicians*, vol. 65, no. 2, pp. 87–108, 2015.

[8] Canadian Cancer Statistics Advisory Committee. Canadian Cancer Statistics 2017. Toronto, ON: Canadian Cancer Society; 2017.

[9] J. N. Aronowitz, “Introduction of transperineal image-guided prostate brachytherapy,” *International Journal of Radiation Oncology Biology Physics*, vol. 89, no. 4, pp. 907–915, 2014.

[10] P. L. Roberson, V. Narayana, D. L. McShan, R. J. Winfield, and P. W. McLaughlin, “Source placement error for permanent implant of the prostate,” *Medical Physics*, vol. 24, no. 2, pp. 251–257, 1997.

[11] R. Taschereau, J. Pouliot, J. Roy, and D. Tremblay, “Seed misplacement and stabilizing needles in transperineal permanent prostate implants,” *Radiotherapy and Oncology*, vol. 55, no. 1, pp. 59–63, 2000.

[12] M. Jamaluddin, S. Ghosh, M. Waine, M. Tavakoli, J. Amanie, A. Murtha, D. Yee, and N. Usmani, “Intraoperative factors associated with stranded source placement accuracy in low-dose-rate prostate brachytherapy,” *Brachytherapy*, vol. 16, no. 3, pp. 497–502, 2017.

[13] H. Kataoka, T. Washio, M. Audette, and K. Mizuhara, “A model for relations between needle deflection, force, and thickness on needle penetration,” in *Medical Image Computing and Computer-Assisted Intervention - MICCAI 2001*, ser. Lecture Notes in Computer Science. Berlin, Heidelberg: Springer, 2001, vol. 2208, ch. 115, pp. 966–974.

[14] A. Okamura, C. Simone, and M. O’Leary, “Force modeling for needle insertion into soft tissue,” *IEEE Transactions on Biomedical Engineering*, vol. 51, no. 10, pp. 1707–1716, 2004.

[15] N. Abolhassani and R. V. Patel, “Deflection of a flexible needle during insertion into soft tissue,” in *Proceedings of the 2006 International Conference of the IEEE Engineering in Medicine and Biology Society*, 2006, pp. 3858–3861.

[16] T. Podder, J. Sherman, E. Messing, D. Rubens, D. Fuller, J. Strang, R. Brasacchio, and Y. Yu, “Needle insertion force estimation model using procedure-specific and patient-specific criteria,” in *Proceedings of the 2006 International Conference of the IEEE Engineering in Medicine and Biology Society*, 2006, pp. 555–558.

[17] N. Abolhassani, R. Patel, and F. Ayazi, “Minimization of needle deflection in robot-assisted percutaneous therapy,” *The International Journal of Medical Robotics and Computer Assisted Surgery*, vol. 3, no. 2, pp. 140–148, 2007.

[18] E. Dehghan, X. Wen, R. Zahiri-Azar, M. Marchal, and S. E. Salcudean, “Needle-tissue interaction modeling using ultrasound-based motion estimation : Phantom study,” *Computer Aided Surgery*, vol. 13, no. 5, pp. 265–280, 2008.

[19] S. Misra, K. B. Reed, A. S. Douglas, K. T. Ramesh, and A. M. Okamura, “Needle-tissue interaction forces for bevel-tip steerable needles,” in *Proceedings of the 2008 IEEE International Conference on Biomedical Robotics and Biomechatronics*, 2008, pp. 224–231.

[20] S. Misra, K. B. Reed, B. W. Schafer, K. T. Ramesh, and A. M. Okamura, “Mechanics of flexible needles robotically steered through soft tissue,” *The International Journal of Robotics Research*, vol. 29, no. 13, pp. 1640–1660, 2010.

[21] R. Roesthuis, Y. V. Veen, A. Jahya, and S. Misra, “Mechanics of needle-tissue interaction,” in *Proceedings of the 2011 IEEE International Conference on Intelligent Robots and Systems*, 2011, pp. 2557–2563.

[22] A. Asadian, M. R. Kermani, and R. V. Patel, “A novel force modeling scheme for needle insertion using multiple kalman filters,” *IEEE Transactions on Instrumentation and Measurement*, vol. 61, no. 2, pp. 429–438, 2012.

[23] M. Abayazid, R. Roesthuis, R. Reilink, and S. Misra, “Integrating deflection models and image feedback for real-time flexible needle steering,” *IEEE Transactions on Robotics*, vol. 29, no. 2, pp. 542–553, 2013.

[24] A. L. G. Robert, G. Chagnon, I. Bricault, P. Cinquin, and A. Moreau-Gaudry, “A generic three-dimensional static force distribution basis for a medical needle inserted into soft tissue,” *Journal of the Mechanical Behavior of Biomedical Materials*, vol. 28, pp. 156–170, 2013.

[25] C. Rossa, R. Sloboda, N. Usmani, and M. Tavakoli, “Estimating needle tip deflection in biological tissue from a single transverse ultrasound image: application to

brachytherapy," *International Journal of Computer Assisted Radiology and Surgery*, vol. 11, no. 7, pp. 1347–1359, 2016.

[26] M. Khadem, C. Rossa, N. Usmani, R. S. Sloboda, and M. Tavakoli, "A two-body rigid/flexible model of needle steering dynamics in soft tissue," *IEEE/ASME Transactions on Mechatronics*, vol. 21, no. 5, pp. 2352–2364, 2016.

[27] C. Rossa and M. Tavakoli, "Issues in closed-loop needle steering," *Control Engineering Practice*, vol. 62, pp. 55–69, 2017.

[28] C. Simone and A. Okamura, "Modeling of needle insertion forces for robot-assisted percutaneous therapy," in *Proceedings of the 2002 IEEE International Conference on Robotics and Automation*, vol. 2, 2002, pp. 2085–2091.

[29] S. Misra, K. B. Reed, B. W. Schafer, K. T. Ramesh, and A. M. Okamura, "Observations and models for needle-tissue interactions," in *Proceedings of the 2009 IEEE International Conference on Robotics and Automation*, 2009, pp. 2687–2692.

[30] R. J. Roesthuis, M. Abayazid, and S. Misra, "Mechanics-based model for predicting in-plane needle deflection with multiple bends," in *Proceedings of the 2012 IEEE International Conference on Biomedical Robotics and Biomechatronics*, 2012, pp. 69–74.

[31] T. Lehmann, M. Tavakoli, N. Usmani, and R. Sloboda, "Force-sensor-based estimation of needle tip deflection in brachytherapy," *Journal of Sensors*, vol. 2013, pp. 1–10, 2013.

[32] M. Khadem, B. Fallahi, C. Rossa, R. S. Sloboda, N. Usmani, and M. Tavakoli, "A mechanics-based model for simulation and control of flexible needle insertion in soft tissue," in *Proceedings of the 2015 IEEE International Conference on Robotics and Automation*, 2015, pp. 2264–2269.

[33] C. Rossa, M. Khadem, R. Sloboda, N. Usmani, and M. Tavakoli, "Adaptive quasi-static modelling of needle deflection during steering in soft tissue," *IEEE Robotics and Automation Letters*, vol. 1, no. 2, pp. 916–923, 2016.

[34] H. Lee and J. Kim, “Estimation of needle deflection in layered soft tissue for robotic needle steering,” in *Intelligent Autonomous Systems 13: Proceedings of the 13th International Conference IAS-13*. Springer International Publishing, 2016, pp. 1133–1144.

[35] C. Rossa, N. Usmani, R. Sloboda, and M. Tavakoli, “A hand-held assistant for semi-automated percutaneous needle steering,” *IEEE Transactions on Biomedical Engineering*, vol. 64, no. 3, pp. 637–648, 2017.

[36] S. DiMaio and S. Salcudean, “Needle Steering and Motion Planning in Soft Tissues,” *IEEE Transactions on Biomedical Engineering*, vol. 52, no. 6, pp. 965–974, 2005.

[37] R. J. Webster, J. S. Kim, N. J. Cowan, G. S. Chirikjian, and A. M. Okamura, “Nonholonomic modeling of needle steering,” *The International Journal of Robotics Research*, vol. 25, no. 5-6, pp. 509–525, 2006.

[38] D. Glozman and M. Shoham, “Image-guided robotic flexible needle steering,” *IEEE Transactions on Robotics*, vol. 23, no. 3, pp. 459–467, 2007.

[39] S. Patil, J. Burgner, R. J. Webster, and R. Alterovitz, “Needle steering in 3-D via rapid replanning,” *IEEE Transactions on Robotics*, vol. 30, no. 4, pp. 853–864, 2014.

[40] B. Fallahi, M. Khadem, C. Rossa, R. Sloboda, N. Usmani, and M. Tavakoli, “Extended bicycle model for needle steering in soft tissue,” in *Proceedings of the 2015 IEEE International Conference on Intelligent Robots and Systems*, 2015, pp. 4375–4380.

[41] W. Park, J. S. Kim, Y. Zhou, N. Cowan, A. Okamura, and G. Chirikjian, “Diffusion-based motion planning for a nonholonomic flexible needle model,” in *Proceedings of the 2005 IEEE International Conference on Robotics and Automation*, 2005, pp. 4600–4605.

[42] W. L. Smith, K. J. M. Surry, G. R. Mills, D. B. Downey, and A. Fenster, “Three-dimensional ultrasound-guided core needle breast biopsy,” *Ultrasound in Medicine & Biology*, vol. 27, no. 8, pp. 1025–1034, 2001.

[43] P. Abolmaesumi, S. Salcudean, Wen-Hong Zhu, M. Sirouspour, and S. DiMaio, “Image-guided control of a robot for medical ultrasound,” *IEEE Transactions on Robotics and Automation*, vol. 18, no. 1, pp. 11–23, 2002.

[44] J. Hong, T. Dohi, M. Hashizume, K. Konishi, and N. Hata, “An ultrasound-driven needle-insertion robot for percutaneous cholecystostomy,” *Physics in Medicine and Biology*, vol. 49, no. 3, pp. 441–455, 2004.

[45] A. Krupa and F. Chaumette, “Control of an ultrasound probe by adaptive visual servoing,” in *Proceedings of the 2005 IEEE International Conference on Intelligent Robots and Systems*, 2005, pp. 2681–2686.

[46] M. Sauvée, P. Poignet, and E. Dombre, “Ultrasound image-based visual servoing of a surgical instrument through nonlinear model predictive control,” *The International Journal of Robotics Research*, vol. 27, no. 1, pp. 25–40, 2008.

[47] Z. Neubach and M. Shoham, “Ultrasound-guided robot for flexible needle steering,” *IEEE Transactions on Biomedical Engineering*, vol. 57, no. 4, pp. 799–805, 2010.

[48] P. Moreira, S. Patil, R. Alterovitz, and S. Misra, “Needle steering in biological tissue using ultrasound-based online curvature estimation,” in *Proceedings of the 2014 IEEE International Conference on Robotics and Automation*, 2014, pp. 4368–4373.

[49] P. Chatelain, A. Krupa, and N. Navab, “3D ultrasound-guided robotic steering of a flexible needle via visual servoing,” in *Proceedings of the 2015 IEEE International Conference on Robotics and Automation*, 2015, pp. 2250–2255.

[50] J. Carriere, C. Rossa, N. Usmani, R. Sloboda, and M. Tavakoli, “Needle shape estimation in soft tissue based on partial ultrasound image observation,” in *Proceedings of the 2015 IEEE International Conference on Robotics and Automation*, 2015, pp. 2277–2282.

[51] M. Waine, C. Rossa, R. Sloboda, N. Usmani, and M. Tavakoli, “Three-dimensional needle shape estimation in trus-guided prostate brachytherapy using 2-d ultrasound images,” *IEEE Journal of Biomedical and Health Informatics*, vol. 20, no. 6, pp. 1621–1631, 2016.

[52] J. Carriere, C. Rossa, R. Sloboda, N. Usmani, and M. Tavakoli, “Real-time needle shape prediction in soft-tissue based on image segmentation and particle filtering,” in *Proceedings of the 2016 IEEE International Conference on Advanced Intelligent Mechatronics*, 2016, pp. 1204–1209.

[53] G. S. Fischer, A. Deguet, C. Csoma, R. H. Taylor, L. Fayad, J. A. Carrino, S. J. Zinreich, and G. Fichtinger, “MRI image overlay: Application to arthrography needle insertion,” *Computer Aided Surgery*, vol. 12, no. 1, pp. 2–14, 2007.

[54] S. B. Park, J.-G. Kim, K.-W. Lim, C.-H. Yoon, D.-J. Kim, H.-S. Kang, and Y.-H. Jo, “A magnetic resonance image-guided breast needle intervention robot system: overview and design considerations,” *International Journal of Computer Assisted Radiology and Surgery*, vol. 12, no. 8, pp. 1319–1331, 2017.

[55] G. Fichtinger, T. L. DeWeese, A. Patriciu, A. Tanacs, D. Mazilu, J. H. Anderson, K. Masamune, R. H. Taylor, and D. Stoianovici, “System for robotically assisted prostate biopsy and therapy with intraoperative CT guidance,” *Academic Radiology*, vol. 9, no. 1, pp. 60–74, 2002.

[56] G. Fichtinger, A. Deguet, K. Masamune, E. Balogh, G. S. Fischer, H. Mathieu, R. H. Taylor, S. J. Zinreich, and L. M. Fayad, “Image overlay guidance for needle insertion in CT scanner,” *IEEE Transactions on Biomedical Engineering*, vol. 52, no. 8, pp. 1415–1424, 2005.

[57] N. Abolhassani, R. Patel, and M. Moallem, “Trajectory generation for robotic needle insertion in soft tissue,” in *Proceedings of the 2004 International Conference of the IEEE Engineering in Medicine and Biology Society*, vol. 4, 2004.

[58] R. Alterovitz, A. Lim, and K. Goldberg, “Steering flexible needles under markov motion uncertainty,” in *Proceedings of the 2005 IEEE International Conference on Intelligent Robots and Systems*, 2005, pp. 120–125.

[59] R. Alterovitz, K. Goldberg, and A. Okamura, “Planning for steerable bevel-tip needle insertion through 2D soft tissue with obstacles,” in *Proceedings of the 2005 IEEE International Conference on Robotics and Automation*, 2005, pp. 1640–1645.

[60] J. Xu, V. Duindam, R. Alterovitz, and K. Goldberg, “Motion planning for steerable needles in 3D environments with obstacles using Rapidly-exploring random trees and backchaining,” in *Proceedings of the 2008 IEEE International Conference on Automation Science and Engineering*, 2008, pp. 41–46.

[61] R. Alterovitz, M. Branicky, and K. Goldberg, “Motion planning under uncertainty for image-guided medical needle steering,” *The International Journal of Robotics Research*, vol. 27, no. 11-12, pp. 1361–1374, 2008.

[62] J. Xu, V. Duindam, R. Alterovitz, J. Pouliot, J. A. M. Cunha, I. C. Hsu, and K. Goldberg, “Planning fireworks trajectories for steerable medical needles to reduce patient trauma,” in *Proceedings of the 2009 IEEE International Conference on Intelligent Robots and Systems*, 2009, pp. 4517–4522.

[63] E. Dehghan and S. E. Salcudean, “Needle insertion parameter optimization for brachytherapy,” *IEEE Transactions on Robotics*, vol. 25, no. 2, pp. 303–315, 2009.

[64] S. Patil and R. Alterovitz, “Interactive motion planning for steerable needles in 3D environments with obstacles,” in *Proceedings of the 2010 IEEE International Conference on Biomedical Robotics and Biomechatronics*, 2010, pp. 893–899.

[65] M. Bernardes, B. V. Adorno, P. Poignet, N. Zemiti, and G. Borges, “Adaptive path planning for steerable needles using duty-cycling,” in *Proceedings of the 2011 IEEE International Conference on Intelligent Robots and Systems*, 2011, pp. 2545–2550.

[66] M. Bernardes, B. Adorno, P. Poignet, and G. Borges, “Robot-assisted automatic insertion of steerable needles with closed-loop imaging feedback and intraoperative trajectory replanning,” *Mechatronics*, vol. 23, no. 6, pp. 630 – 645, 2013.

[67] J. Wang, X. Li, J. Zheng, and D. Sun, “Dynamic path planning for inserting a steerable needle into a soft tissue,” *IEEE/ASME Transactions on Mechatronics*, vol. 19, no. 2, pp. 549–558, 2014.

[68] M. A. Meltsner, N. J. Ferrier, and B. R. Thomadsen, “Observations on rotating needle insertions using a brachytherapy robot,” *Physics in Medicine and Biology*, vol. 52, no. 19, pp. 6027–6037, 2007.

[69] J. Engh, G. Podnar, D. Kondziolka, and C. Riviere, "Toward effective needle steering in brain tissue," in *Proceedings of the 2006 International Conference of the IEEE Engineering in Medicine and Biology Society*, 2006, pp. 559–562.

[70] D. S. Minhas, J. A. Engh, M. M. Fenske, and C. N. Riviere, "Modeling of needle steering via duty-cycled spinning," in *Proceedings of the 2007 International Conference of the IEEE Engineering in Medicine and Biology Society*, 2007, pp. 2756–2759.

[71] H. Bassan, R. Patel, and M. Moallem, "A novel manipulator for percutaneous needle insertion: Design and experimentation," *IEEE/ASME Transactions on Mechatronics*, vol. 14, no. 6, pp. 746–761, 2009.

[72] N. Hungr, M. Baumann, J.-A. Long, and J. Troccaz, "A 3-D ultrasound robotic prostate brachytherapy system with prostate motion tracking," *IEEE Transactions on Robotics*, vol. 28, no. 6, pp. 1382–1397, 2012.

[73] M. Muntener, A. Patriciu, D. Petrisor, D. Mazilu, H. Bagga, L. Kavoussi, K. Cleary, and D. Stoianovici, "Magnetic resonance imaging compatible robotic system for fully automated brachytherapy seed placement," *Urology*, vol. 68, no. 6, pp. 1313–1317, 2006.

[74] L. Phee, Di Xiao, J. Yuen, Chee Fatt Chan, H. Ho, Choon Hua Thng, Christopher Cheng, and Wan Sing Ng, "Ultrasound guided robotic system for transperineal biopsy of the prostate," in *Proceedings of the 2005 IEEE International Conference on Robotics and Automation*, 2005, pp. 1315–1320.

[75] R. Webster, J. Memisevic, and A. Okamura, "Design considerations for robotic needle steering," in *Proceedings of the 2005 IEEE International Conference on Robotics and Automation*, 2005, pp. 3588 – 3594.

[76] Z. Wei, G. Wan, L. Gardi, D. B. Downey, and A. Fenster, "Robotic-aided 3D TRUS guided intraoperative prostate brachytherapy," in *Proc. SPIE 5367, Medical Imaging 2004: Visualization, Image-Guided Procedures, and Display*. International Society for Optics and Photonics, 2004, pp. 361–370.

[77] G. Fichtinger, J. P. Fiene, C. W. Kennedy, G. Kronreif, I. Iordachita, D. Y. Song, E. C. Burdette, and P. Kazanzides, “Robotic assistance for ultrasound-guided prostate brachytherapy,” *Medical Image Analysis*, vol. 12, no. 5, pp. 535–545, 2008.

[78] S. Okazawa, R. Ebrahimi, J. Chuang, S. E. Salcudean, and R. Rohling, “Hand-held steerable needle device,” *IEEE/ASME Transactions on Mechatronics*, vol. 10, no. 3, pp. 285–296, 2005.

[79] S. E. Salcudean, T. D. Prananta, W. J. Morris, and I. Spadinger, “A robotic needle guide for prostate brachytherapy,” in *Proceedings of the 2008 IEEE International Conference on Robotics and Automation*, 2008, pp. 2975–2981.

[80] C. M. Schneider, A. M. Okamura, and G. Fichtinger, “A robotic system for transrectal needle insertion into the prostate with integrated ultrasound,” in *Proceedings of the 2004 IEEE International Conference on Robotics and Automation*, 2004, pp. 365–370.

[81] D. Y. Song, E. C. Burdette, J. Fiene, E. Armour, G. Kronreif, A. Deguet, Z. Zhang, I. Iordachita, G. Fichtinger, and P. Kazanzides, “Robotic needle guide for prostate brachytherapy: Clinical testing of feasibility and performance,” *Brachytherapy*, vol. 10, no. 1, pp. 57–63, 2011.

[82] S. Basu, J. Tsai, and A. Majewicz, “Evaluation of tactile guidance cue mappings for emergency percutaneous needle insertion,” in *2016 IEEE Haptics Symposium (HAPTICS)*, 2016, pp. 106–112.

[83] O. Gerovich, P. Marayong, and A. M. Okamura, “The effect of visual and haptic feedback on computer-assisted needle insertion,” *Computer Aided Surgery*, vol. 9, no. 6, pp. 243–249, 2004.

[84] D. Magee, Y. Zhu, R. Ratnalingam, P. Gardner, and D. Kessel, “An augmented reality simulator for ultrasound guided needle placement training,” *Medical & Biological Engineering & Computing*, vol. 45, no. 10, pp. 957–967, 2007.

[85] C. Rossa, J. Fong, N. Usmani, R. Sloboda, and M. Tavakoli, “Multiactuator haptic feedback on the wrist for needle steering guidance in brachytherapy,” *IEEE Robotics and Automation Letters*, vol. 1, no. 2, pp. 852–859, 2016.

[86] J. Gere and B. Goodno, *Mechanics of Materials*. Cengage Learning, 2008.

[87] A. Savitzky and M. J. E. Golay, “Smoothing and differentiation of data by simplified least squares procedures.” *Analytical Chemistry*, vol. 36, no. 8, pp. 1627–1639, 1964.

[88] J. M. Gere and S. P. Timoshenko, *Mechanics of Materials*. Boston, MA: Springer US, 1991.

[89] A. P. C. Choi and Y. P. Zheng, “Estimation of Young’s modulus and Poisson’s ratio of soft tissue from indentation using two different-sized indentors: Finite element analysis of the finite deformation effect,” *Medical and Biological Engineering and Computing*, vol. 43, no. 2, pp. 258–264, 2005.

[90] B. Siciliano, L. Sciavivvo, L. Villani, and G. Oriolo, *Robotics: Modelling, Planning & Control*. Springer, 2011.

[91] K. Reed, A. Majewicz, V. Kallem, R. Alterovitz, K. Goldberg, N. Cowan, and A. Okamura, “Robot-assisted needle steering,” *IEEE Robotics Automation Magazine*, vol. 18, no. 4, pp. 35–46, 2011.

[92] S. E. Song, J. Tokuda, K. Tuncali, C. M. Tempany, E. Zhang, and N. Hata, “Development and preliminary evaluation of a motorized needle guide template for MRI-guided targeted prostate biopsy,” *IEEE Transactions on Biomedical Engineering*, vol. 60, no. 11, pp. 3019–3027, 2013.

[93] N. J. Cowan, K. Goldberg, G. S. Chirikjian, G. Fichtinger, R. Alterovitz, K. B. Reed, V. Kallem, W. Park, S. Misra, and A. M. Okamura, “Robotic needle steering: Design, modeling, planning, and image guidance,” in *Surgical Robotics: Systems Applications and Visions*. Boston, MA: Springer US, 2011, pp. 557–582.

[94] J. Reddy, *An Introduction to the Finite Element Method*, 2nd ed., ser. McGraw-Hill series in mechanical engineering. McGraw-Hill, 1993.

[95] G. Genta, *Vibration Dynamics and Control*, ser. Mechanical Engineering Series. New York, NY, USA: Springer, 2008.

[96] K. Hoyt, B. Castaneda, M. Zhang, P. Nigwekar, P. A. di Sant'agnese, J. V. Joseph, J. Strang, D. J. Rubens, and K. J. Parker, "Tissue elasticity properties as biomarkers for prostate cancer." *Cancer biomarkers : section A of disease markers*, vol. 4, no. 4-5, pp. 213–25, 2008.

[97] R. Hooke and T. A. Jeeves, ""direct search" solution of numerical and statistical problems," *Journal of the ACM*, vol. 8, no. 2, pp. 212–229, 1961.

[98] M. P. Ottensmeyer and J. K. Salisbury, *In Vivo Data Acquisition Instrument for Solid Organ Mechanical Property Measurement*. Berlin, Heidelberg: Springer Berlin Heidelberg, 2001, pp. 975–982.

[99] Min-Hua Lu, W. Yu, Qing-Hua Huang, Yan-Ping Huang, and Yong-Ping Zheng, "A hand-held indentation system for the assessment of mechanical properties of soft tissues in vivo," *IEEE Transactions on Instrumentation and Measurement*, vol. 58, no. 9, pp. 3079–3085, 2009.

[100] D. Fu, S. F. Levinson, S. M. Gracewski, and K. J. Parker, "Non-invasive quantitative reconstruction of tissue elasticity using an iterative forward approach," *Physics in Medicine and Biology*, vol. 45, no. 6, pp. 1495–1509, 2000.

[101] K. Nightingale, S. McAleavey, and G. Trahey, "Shear-wave generation using acoustic radiation force: in vivo and ex vivo results," *Ultrasound in Medicine & Biology*, vol. 29, no. 12, pp. 1715–1723, 2003.

[102] P. Moreira and S. Misra, "Biomechanics-based curvature estimation for ultrasound-guided flexible needle steering in biological tissues," *Annals of Biomedical Engineering*, vol. 43, no. 8, pp. 1716–1726, 2014.